TU Delft

Delft University of Technology

Raman based identification of on-chip trapped single micro-organisms

A feasibility study

Heldens, Jeroen

DOI
10.4233/uuid:f5ddb664-54ef-4f4f-b810-01c2f727b8b

Publication date
2019

Document Version
Final published version

Citation (APA)
Heldens, J. (2019). *Raman based identification of on-chip trapped single micro-organisms: A feasibility study*. [Dissertation (TU Delft), Delft University of Technology]. https://doi.org/10.4233/uuid:f5ddb664-54ef-4f4f-b810-01c2f727b8b

Important note
To cite this publication, please use the final published version (if applicable).
Please check the document version above.

Copyright
Other than for strictly personal use, it is not permitted to download, forward or distribute the text or part of it, without the consent of the author(s) and/or copyright holder(s), unless the work is under an open content license such as Creative Commons.

Takedown policy
Please contact us and provide details if you believe this document breaches copyrights.
We will remove access to the work immediately and investigate your claim.

This work is downloaded from Delft University of Technology.
For technical reasons the number of authors shown on this cover page is limited to a maximum of 10.

RAMAN BASED IDENTIFICATION OF ON-CHIP TRAPPED SINGLE MICRO-ORGANISMS: A FEASIBILITY STUDY

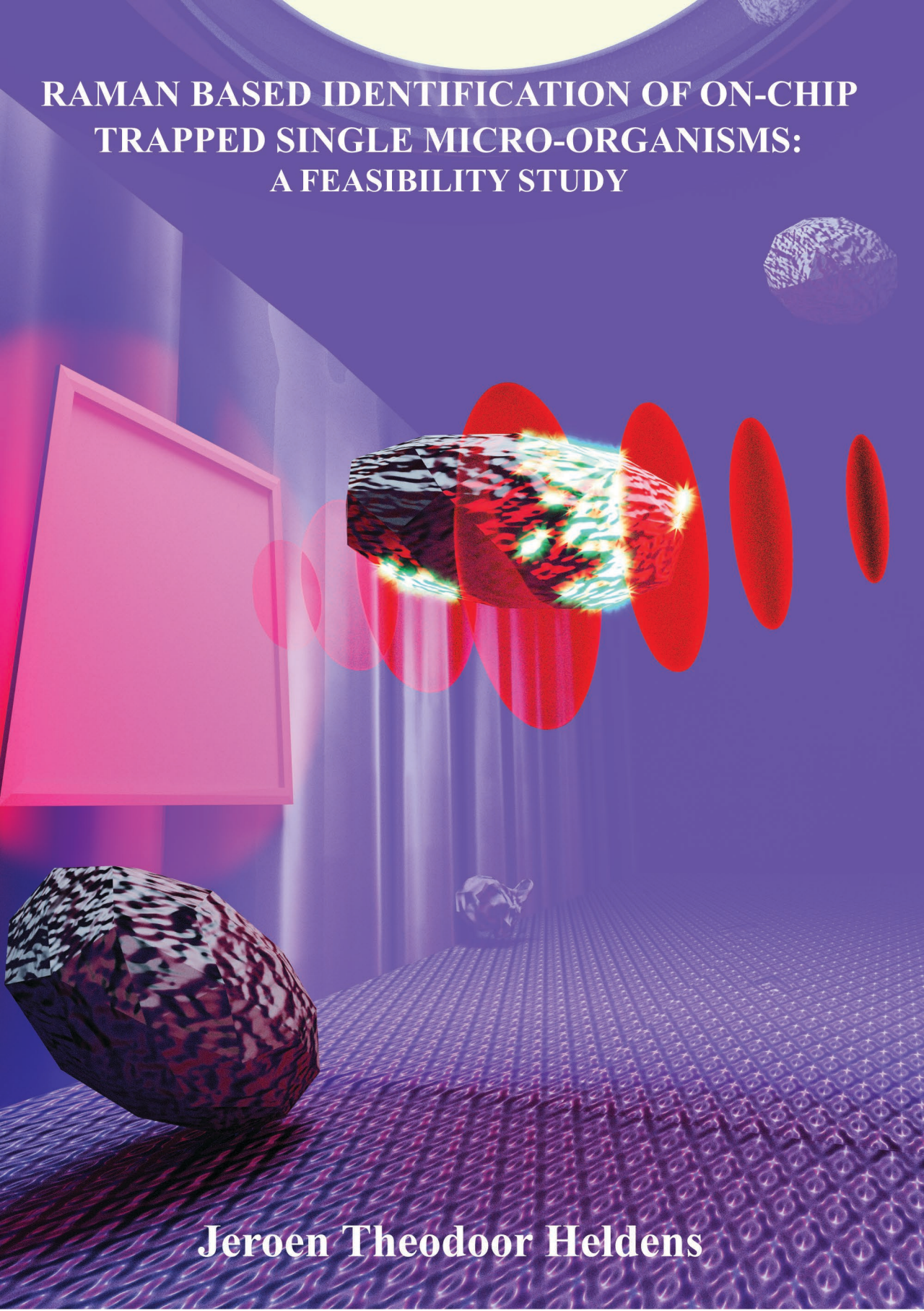

Jeroen Theodoor Heldens

RAMAN BASED IDENTIFICATION OF ON-CHIP TRAPPED SINGLE MICRO-ORGANISMS:

A FEASIBILITY STUDY

RAMAN BASED IDENTIFICATION OF ON-CHIP TRAPPED SINGLE MICRO-ORGANISMS:

A FEASIBILITY STUDY

Proefschrift

ter verkrijging van de graad van doctor
aan de Technische Universiteit Delft,
op gezag van de Rector Magnificus Prof. dr. ir. T.H.J.J. van der Hagen,
voorzitter van het College voor Promoties,
in het openbaar te verdedigen op **17 mei 2019 om 10:00 uur**

door

Jeroen Theodoor Heldens

Doctorandus in de Natuurwetenschappen (research),
Radboud Universiteit Nijmegen, Nijmegen, Nederland,
geboren te Roermond, Nederland.

Dit proefschrift is goedgekeurd door de

promotor: Prof. dr. ir. L.J. van Vliet
copromotor: Dr. J. Caro

Samenstelling promotiecommissie:

Rector Magnificus,	voorzitter
Prof. dr. ir. L.J. van Vliet,	Technische Universiteit Delft
Dr. J. Caro,	Technische Universiteit Delft

Onafhankelijke leden:

Dr. H.L. Offerhaus,	Universiteit Twente
Dr. H. Miedema,	Westus
Prof. dr. U. Staufer,	Technische Universiteit Delft
Dr. N. Bhattacharya,	Technische Universiteit Delft
Prof. dr. S.J. Picken,	Technische Universiteit Delft

The work described in this thesis is supported by wetsus, centre of excellence for sustainable water technology

Keywords: optical trapping, Raman spectroscopy, on-chip, micro-organisms, identification

Printed by: Ridderprint | www.ridderprint.nl

Front & Back: Artist impression of a *Bacillus subtilis* spore trapped in the dual-waveguide trap & GaP PhC

Cover design: J. T. Heldens

Copyright © 2019 by Jeroen T. Heldens

ISBN: 978-94-6384-038-5

An electronic version of this dissertation is available at
`http://repository.tudelft.nl/`.

"Dear Sir or Madam, will you read my book?
It took me years to write, will you take a look?"

Lennon & McCartney

CONTENTS

Summary **9**

Samenvatting **11**

1 Introduction **1**
1.1 The current identification of microbiological contaminants 2
1.2 Identification of micro-organisms by optical spectroscopy 4
1.3 Laser Tweezers Raman Spectroscopy 6
1.3.1 Raman Spectroscopy. 6
1.3.2 Laser tweezers (optical trapping). 10
1.4 Lab-on-a-chip 13
1.5 Triplex dual-waveguide traps 15
1.6 Recapitulation 16
1.7 Research questions 16
1.8 Content of this thesis 17

2 Classification of yeast species using single cell laser tweezers Raman spectroscopy **19**
2.1 Introduction 21
2.2 Materials and methods 23
2.2.1 Origin, maintenance and cultivation of the yeast strains 23
2.2.2 Laser tweezers Raman spectroscopy setup 23
2.2.3 Laser tweezers Raman spectroscopy 24
2.2.4 Spectra analysis 25
2.3 Results 27
2.4 Discussion 30
2.5 Conclusions. 32
2.6 Acknowlegdments 32

3 On-chip optical trapping and Raman spectroscopy using a TripleX dual-waveguide trap **33**
3.1 Introduction 34
3.2 Design of the dual-waveguide trap and experimental setup. 36
3.3 Optical field of the dual-waveguide trap 39
3.4 Trapping experiments. 41
3.5 Force calculations and optical power considerations 42
3.6 Raman spectroscopy 45
3.7 Conclusions. 47
3.8 Acknowledgments 47

4 Preparing the setup for bio-particles and comparing the ltrs and dual-waveguide trap **49**
4.1 Introduction . . . 50
4.2 Method . . . 51
4.2.1 The setup . . . 51
4.3 Results . . . 53
4.3.1 Raman generation and acquisition geometry: comparing the ltrs and dual-waveguide trap. . . . 53
4.3.2 Comparison of the Raman generating properties of the 5, 10, 15 and 20 μm dual-waveguide traps . . . 58
4.3.3 Analysis of the background signal . . . 62
4.4 Discussion and Conclusions . . . 65

5 The feasibility of *Bacillus subtilis* spore identification with the dual-waveguide trap **67**
5.1 Introduction . . . 68
5.2 Materials and Methods . . . 69
5.2.1 *Bacillus subtilis* spores . . . 69
5.2.2 Devices and Setup . . . 69
5.2.3 Acquiring Raman spectra and method of spectrum analysis . . . 71
5.3 Results . . . 74
5.3.1 Raman spectra of bacterial spores obtained with the 10 μm trap. . . . 74
5.3.2 Raman spectra of bacterial spores obtained with the 5 μm trap . . . 77
5.4 Discussion and Conclusions . . . 82
5.4.1 Evaluation of the setup. . . . 82
5.4.2 Raman spectra of *Bacillus subtilis* spores . . . 82
5.4.3 Conclusions . . . 83

6 Conclusions and Outlook **85**
6.1 Conclusions. . . . 86
6.2 Outlook . . . 88
6.2.1 Researching the physics and application suitability . . . 88
6.2.2 Envisioning a dual-waveguide trap based instrument . . . 89

Acknowledgements **91**

A Appendix **93**

B Acronyms **95**

List of Figures **97**

Curriculum Vitæ **105**

List of Publications **107**

References **109**
References . . . 109

SUMMARY

An important aspect in increasing our health and safety is the development of new sensors for screening drinking water samples for the presence of microbiological contaminants. The main problem associated with the detection and identification of these microbial contaminants is the long process time. The majority of the time is required for their purification and multiplication due to the low concentrations in which they are found. These steps can be avoided by using spectroscopic identification rather than biochemical techniques.

Raman spectroscopy provides a fingerprint based on the vibrational states of molecular bonds from which the bio-particles containing these can be identified. The Raman effect is weak, but rich in information and flexible with respect to its excitation wavelength. When working in an aqueous environment it can take advantage of the absorption minima of water to outperform for instance IR spectroscopy. Optical trapping allows the immobilization of particles without additional preparation steps and provides much added value to, and is highly compatible with Raman spectroscopy. Lab-on-a-chip techniques allow for integration and large-scale parallelization of processes, which is unavoidable when performing large-scale identification of microbial contaminants on the level of single cells. To take advantage of established CMOS processing techniques for mass production in electronics, a CMOS compatible technology for integrated photonics providing waveguides transparent at a Raman suitable wavelengths, is needed. TripleX is such a waveguide technology.

The research presented in this thesis shows the realization of an integrated dual-waveguide optical trap and the feasibility of its use for the identification of micro-organisms based on their Raman spectrum induced by the same on-chip optical beams used for trapping.

It does so in four main steps.

Firstly, laser tweezers Raman spectroscopy is used to classify the closely related yeast species *Kluyveromyces lactis* and *Saccharomyces cerevisiae* from measurements at the single cell level. Laser tweezers Raman spectroscopy combines optical trapping of a cell and generation of its characteristic Raman spectrum using one laser-beam focus. This enables fingerprinting of a cell's molecular composition in a harmless fluidic environment within minutes. Laser tweezers Raman spectroscopy is considerably faster than well-known biological techniques based on streak plating or PCR, and requires far less biological material.
For each yeast species a training set and a test set were measured. Visual inspection of the spectra showed intra-species variations obstructing division into two classes by eye. Application of a classification rule based on Fisher's criterion nevertheless led to the successful blind classification of the test-set cells. Finally, a Kolmogorov-Smirnov test

indicated that the difference between the distributions of the species was statistically significant, implying biological origin of the classification. This successful extension of laser tweezers Raman spectroscopy to classification of the aforementioned yeasts underlines its applicability in microbiology and will hopefully contribute to the process of its adoption in this discipline. Laser tweezers Raman spectroscopy is not limited to rapid classification of single cells, but may also include e.g. study of the cell metabolism.

Secondly, a new approach to the dual-beam geometry for on-chip optical trapping and Raman spectroscopy, using box shaped waveguides microfabricated in TripleX technology is demonstrated. These waveguides consist of SiO_2 and Si_3N_4, so as to provide a low index contrast with respect to the SiO_2 claddings and low signal loss, while retaining the advantages of Si_3N_4. The waveguides enable both the trapping and Raman functionality with the same dual beams. Polystyrene beads of 1 μm diameter can be trapped with this device. In the axial direction discrete trapping positions occur, owing to the intensity pattern of the interfering beams. Interpretation of the trapping events on the basis of simulated optical fields and calculated optical forces indicate that a strong trap is formed by the beams emitted by the waveguides. Furthermore, the acquisition of Raman spectra of a single trapped bead is demonstrated. The spectra obtained in this manner show distinct polystyrene Raman peaks for integration times as short as 0.25 seconds.

Thirdly, usual procedure of background subtraction is found to be less effective for Raman spectra obtained with the dual-waveguide trap, due to its specific geometry. The differences in the Raman generating properties between four dual-waveguide traps with varying distances between their waveguide facets are explored using a saturated ascorbic acid solution. Furthermore, the origin of a periodic background observed in the ascorbic acid spectra is investigated.

Finally, an alternative method of signal acquisition and processing is presented to deal with the lack of fluidic control in the device and the periodic background and low signal-to-noise ratio observed in the spectra. The 10 μm and 5 μm traps are used in trapping and Raman generation experiments with biological relevant particles in the form of Bacillus subtilis spores. These experiments result in noisy spectra for many and few spores in both traps. Using the presented processing the spectra are identified as *Bacillus subtilis* spore spectra. A comparison of the obtained signal-to-noise values to literature benchmarks shows the feasibility of micro-organisms identification with the dual-waveguide trap.

SAMENVATTING

Een belangrijk aspect in het verbeteren van onze gezondheid en veiligheid is het ontwikkelen van nieuwe sensoren voor het testen van drinkwater op de aanwezigheid van vervuilende micro-organismen. Het grootste probleem bij de detectie en identificatie van deze micro-bacteriële vervuiling is de lage concentratie waarin ze aangetroffen wordt waardoor zuivering en vermenigvuldiging veel tijd kost. Door het gebruik van spectroscopische in plaats van biochemische technieken kunnen deze stappen vermeden worden.

Raman spectroscopie geeft een op de vibrationele toestanden van moleculaire bindingen gebaseerde vingerafdruk. Aan de hand hiervan kunnen de bio-deeltjes die deze bevatten geïdentificeerd worden. Het Raman effect is zwak maar rijk aan informatie en flexibel met betrekking tot zijn excitatiegolflengte. Wanneer er gewerkt wordt in een waterig milieu kan Raman spectroscopie beter presteren dan bijvoorbeeld IR spectroscopie door de absorptieminima van water te benutten. Een optische val kan deeltjes immobiliseren zonder extra voorbereidings en voegt veel waarde toe aan, en is zeer compatibel met Raman spectroscopie. Lab-op-een-*chip* technieken faciliteren integratie en massale parallellisatie iets dat vrijwel onontkoombaar is bij de identificatie van individuele cellen op grote schaal. Om gebruik te maken van de bestaande CMOS procestechnieken voor de massaproductie van elektronica, is een CMOS compatibele golfgeleider technologie voor geïntegreerde fotonica nodig met golfgeleiders die transparant zijn bij voor Raman spectroscopie geschikte golflengtes. TripleX is zo een golfgeleider technologie. Het onderzoek in deze thesis toont de realisatie van een dubbele-golfgeleider optische val en de geschiktheid daarvan voor de identificatie van micro-organismen op basis van een Raman spectrum geïnduceerd met de zelfde *on-chip* optische bundels die voor de val gebruikt zijn.

Dit wordt gedaan in vier stappen.

Ten eerste wordt laser pincet Raman spectroscopie gebruikt om de nauw verwante gist soorten *Kluyveromyces lactis* en *Saccharomyces cerevisiae* te classificeren, op basis van metingen op het niveau van individuele cellen. Laser pincet Raman spectroscopie combineert het optisch vangen van een cel met het genereren van het karakteristieke Raman spectrum van deze cel, in een enkele laser focus. Hierdoor is het mogelijk een vingerafdruk te nemen van de moleculaire compositie van de cel in een onschadelijke vloeistof omgeving, binnen enkele minuten. Laser pincet Raman spectroscopie is aanzienlijk sneller dan bekende biologische technieken gebaseerd op *streak plating* of PCR én heeft veel minder biologisch materiaal nodig.

Voor elke gist soort is er een training- en test-set gemeten. Een visuele inspectie van de spectra toonde soort interne variatie die een verdeling in twee klassen op het oog verhinderd. De toepassing van een op Fisher's criterium gebaseerde classificatie regel

leverde, niettemin, een succesvolle classificatie van de testset cellen op. Hierna werd met een Kolmogorov-Smirnov test aangetoond dat het verschil tussen de distributies van de soorten statistisch significant is, wat een biologische oorsprong van de classificatie impliceert. Deze succesvolle uitbreiding van laser pincet Raman spectroscopie naar de genoemde gist soorten onderstreept de toepasbaarheid hiervan in de microbiologie en draagt hopelijk bij aan de acceptatie ervan in deze discipline. Laser pincet Raman spectroscopie kan niet alleen gebruikt worden voor de snelle classificatie van cellen maar kan ook gebruikt worden om bijvoorbeeld het celmetabolisme te bestuderen.

Ten tweede, wordt een nieuwe benadering van de dubbelle-bundel geometrie voor *on-chip* optische vallen en Raman spectroscopie, gebruik makend van balkvormige golfgeleiders micro-gefabriceerd in TripleX technologie, gedemonstreerd. Deze golfgeleider bestaan uit SiO_2 en Si_3N_4, dit zorgt voor een laag index contrast met de SiO_2 bedekking en laag signaalverlies, terwijl de voordelen van Si_3N_4 behouden blijven. De golfgeleiders maken zowel de val en de Raman functionaliteit mogelijk met de zelfde dubbele bundels.

Met dit *device* kunnen polystyreen bolletjes met een diameter van 1 µm gevangen worden. In de axiale richting treden discrete vallen op ten gevolge van het intensiteitpatroon van de interfererende bundels. Interpretatie van de vangsten op basis van gesimuleerde optische velden en brekende optische krachten duiden aan dat de door de golfgeleiders uitgestraalde bundels een sterke val vormen. Verder is de acquisitie van Raman spectra van enkele gevangen bolletjes gedemonstreerd. De zo verkregen spectra tonen onderscheidbare polystyreen Raman pieken voor integratie tijden zo kort als 0.25 seconden.

Ten derde, blijkt de gebruikelijke achtergrond substractie methode minder effectief te zijn voor Raman spectra verkregen met de dubbele-golfgeleider val, ten gevolge van de specifieke geometrie hier van. De verschillen in Raman genererende eigenschappen tussen vier verschillende dubbele-golfgeleider vallen, variërend in de afstand tussen de golfgeleider facetten worden onderzocht met behulp van een verzadigde ascorbinezuur oplossing. Verder wordt de oorsprong van de periodieke achtergrond, te zien in de ascorbinezuur spectra, onderzocht.

Ten slotte, word er een alternatieve signaalacquisitie- en verwerkings-methode gepresenteerd om om te gaan met het gebrek aan fluidische controle in het *device*, de periodieke achtergrond en de lage signaal-ruis-verhouding van de spectra. De 10 µm en 5 µm vallen zijn gebruikt in experimenten die als doel het genereren van Raman spectra van gevangen biologisch relevante deeltjes in de vorm van *Bacillus subtilis* sporen hadden. Deze experimenten resulteren in ruisige spectra van menige en weinig sporen in beide vallen. Met behulp van de gepresenteerde verwerkingsmethode worden de spectra geïdentificeerd als spectra afkomstig van *Bacillus subtilis* sporen. Een vergelijking van de verkregen signaal-ruis-verhoudingen met ijkpunten uit de literatuur toont de haalbaarheid van micro-organisme identificatie met de dubbele-golfgeleider val aan.

1

INTRODUCTION

Our senses allow us to perceive the world around us. A sensor is a device that detects physical phenomena, which may augment our senses by either allowing us to sense remotely or by allowing us to perceive things that would otherwise remain unnoticed. As such, new sensors facilitate us in observing and detecting things we previously could not. This capability is especially important where it directly affects our health, as it does with detecting contaminants in essentials such as drinking water. In its efforts to provide the cleanest drinking water, the industry has moved beyond the removal of readily detectable contaminants such as soil particles and organics [1] and is now targeting microbiological contaminants such as bacteria and spores. The research presented in this thesis is aimed at integrating Raman spectroscopy and optical trapping in a lab-on-a-chip sensor capable of detecting such contaminants in water at the single cell level.

In this introductory chapter, we will first look at the current methods to identify microorganisms. We then compare these biochemical techniques to optical techniques employing spectroscopy. Then we will look in more detail at Raman spectroscopy and optical trapping and the benefits and drawbacks that accompany this combination. Next, we focus on the technologies needed to integrate sample handling using micro-fluidics, optical trapping and diagnostics in a single device. Finally, we provide some summarizing remarks and a brief overview of the following chapters.

1

1.1. THE CURRENT IDENTIFICATION OF MICROBIOLOGICAL CONTAMINANTS

The detection and subsequent identification of microbiological contaminants is an issue common to a diversity of fields ranging from the food industry to the health care sector. The main problem in a screening situation is the low concentrations of microbiological contaminants in the samples subject to investigation. Consequently, almost all techniques currently in use, being biological or chemical in nature, rely on the multiplication of identifiable material. This multiplication is time consuming. As a result, identification can take, depending on the technique, between 8 and 48 hours, which is a determining factor for the amount of damage that arises from the contamination.

The two most important steps in managing microbial contaminants are the isolation of the contaminant and the identification thereof [2]. These steps can be tackled in a variety of ways based on several biochemical techniques i.e. replicate plating, Polymerase Chain Reaction (PCR) and sequencing, which we briefly discuss.

REPLICATE PLATING

Replicate plating deals with the growing of bacterial cultures on agarose plates under different circumstances to allow identification. The first step is the culturing of a diluted sample on a plate, which allows the formation of colonies that grow from a single cell. For all practical purposes, this is a purification step that allows isolated species to be selected for further testing. These isolates are then cultured on media with different compositions, which permits the study of growth, metabolism and morphology of the isolates. These studies allow experts to assess which microbial species is being tested. The duration of a single culture step can vary from one day to weeks depending on the species [2]. Because of the multitude of test, experts frequently need to select the most appropriate test based on the origin of the sample in order to save time.

POLYMERASE CHAIN REACTION (PCR)

The Polymerase Chain Reaction is a biochemical technique. Repeatedly splitting double stranded DNA/RNA strands and using the single strands to grow new double strands using a chemical procedure lies at the basis of PCR. In this manner, an exponential increase in the amount of genetic material is realized. The 20 to 40 cycles required to obtain sufficient genetic material usually takes 2 to 3 hours depending on the size of the fragments used [3]. Examining the fragment sizes of the multiplied material, through gel electrophoresis, subsequently provides the species identification. Resulting in the familiar ladder type images that can be compared to images of know samples. Although there are many different versions of PCR, differing in among others the type of primers or the origin of the genetic material used, most rely on an initial isolation step using plating. This means that although the PCR itself might only take a few hours the preparations might still take more than a day.

SEQUENCING

Not yet standard practice [4] the sequencing of genetic material is seen by many as the next big thing in microbial identification. The next generation sequencing (NGS) techniques use innovative approaches such as the detection of single fluorescently labelled

bases during sequence syntheses (SMRT sequencing [5]) or measuring the current associated with single bases being pulled through a nanopore (Nanopore sequencing [6]). Although these techniques are becoming more affordable, they are currently estimated to cost 200 to 400 dollar per genome and take between 2 hours and 2 days to complete. Both techniques almost literally read stretches of genetic material. These reads are reconstructed into a complete genome, which is compared to a database of known genomes to identify the species. Many NGS techniques either rely on a PCR preparation step or incorporate a PCR like multiplication technique to provide sufficient genetic material to be read [7]. This means that they incur the same drawbacks as regular PCR in that the sequencing itself might be (very) fast but the preparation might still consume more than a day.

BIO CHEMICAL IDENTIFICATION WITHOUT CULTURING

The aforementioned descriptions raise the question if culturing can be avoided. Biochemical identification without culturing yields two challenges. First, being able to cope with small amounts of genetic starting material. Second, being able to identify multiple species of micro-organisms in a sample. Since both PCR in combination with gel electrophoresis and NGS techniques identify microorganism based on a comparison of multiple pieces of genetic material with a reference, this task becomes increasingly difficult when trying to identify multiple species in one process. An analogy would be to simultaneously lay several similarly themed jigsaw puzzles after having jumbled the pieces together. In certain cases, this is possible e.g., when the sample contains relatively few micro-organisms such as with cerebrospinal fluid [2] or if there is prior knowledge regarding the population of micro-organisms. In these cases, sequencing can be used to identify multiple organisms from the sample by comparing the reads to a database. Another option is to use a targeted PCR where primers coding for species-specific genes are used to only amplify these genes. A successful amplification then indicates the presence of said species.

1

1.2. IDENTIFICATION OF MICRO-ORGANISMS BY OPTICAL SPECTROSCOPY

Identification of micro-organisms by optical spectroscopy is based on the interaction of the organism's molecular and structural components with an incident light beam. The wavelength-dependent change in the light returning from the sample, called the spectroscopic fingerprint, is then used to identify the micro-organisms. In contrast to biochemical techniques, spectroscopic techniques do not require the multiplication of material to be effective. Instead smaller samples can simply be investigated using stronger light sources, more sensitive detectors or advanced signal amplification techniques. This may reduce the time needed for identification from hours to minutes. In addition, optical spectroscopy is label-free and non-destructive, meaning that a sample can be used for further study after identification of the contaminant. In the following section, Infrared and fluorescence spectroscopy are briefly discussed before a more thorough treatment of Raman spectroscopy is presented.

INFRARED (IR) SPECTROSCOPY

Infrared (IR) spectroscopy, denoted as Near Infrared (NIR) or Far Infrared (FIR) spectroscopy depending on the wavelength range used, has been established as a standard technique for the identification of chemicals. As a form of vibrational spectroscopy, IR spectroscopy probes the vibrational modes of molecules, providing information on both chemical composition and structure of most chemical components. The acquired spectrum forms a chemical fingerprint uniquely identifying the sample.

IR spectroscopy can be employed in either emission or absorption and provides a signal strength that has a linear relation to the source strength. The basic principle of IR spectroscopy is that a sample is exposed to a broad range of IR wavelengths. After the interaction with the sample, the wavelength-dependent emission or absorption intensity is evaluated. This is achieved by either scanning a source through a wavelength range or by passing the signal generated by a broadband source through a grating. As a result, the sample always absorbs portions of the light, leading to sample heating which can potentially damage the sample. IR absorption is also problematic for samples in aqueous environments, since the incoming Infrared light will also be absorbed by the water surrounding the sample making it harder to detect the sample suspended in the water. To circumvent this problem IR spectroscopy of microbiological contaminants is often performed on samples smeared or dried on a suitable carrier. This requires additional sample preparation and can lead to changes in the chemical fingerprint of the sample since the vibrational spectrum of a molecule is sensitive to its surroundings.

FLUORESCENCE SPECTROSCOPY

In fluorescence spectroscopy a molecule is excited electronically through absorption of a photon, after which it goes through one or more non-radiative vibrational relaxation steps. Finally the molecule relaxes through an electronic transition under the emission of a photon of lower energy compared to the exciting photon. Molecules that exhibit this behavior are called fluorophores. Because the initial, intermediate and final vibrational state of the fluorophore can vary, both the fluorescence excitation and emission spectrum appear rather smooth, making it non trivial to identify the different vibrational

states [8]. Most often, fluorescence spectroscopy is used as a proxy to identify microbial contaminants by using fluorescent probes, i.e. fluorescent molecules attached to small strands of DNA/RNA or anti-bodies [9]. However since the basis of these methods is intrinsically bio-chemical we will not elaborate on them. Especially since label-free fluorescent identification of micro-organisms is possible, however troublesome. In this approach one relies on the fluorophores naturally present in micro-organisms most prominently amino acids, such as tryptophan, tyrosine and phenylalanine, and nucleic acids [10]. However, these are only present in relatively small amounts, compared to for instance IR active components. As a consequence the resulting signal is very weak and can easily be overshadowed by other effects [11]. In addition, large and pure samples are required to ensure acceptable acquisition times, which makes it again dependent on culturing as a preparation step, thereby effectively losing most, if not all, benefits of a spectroscopic approach. As such, fluorescence spectroscopy becomes a very unlikely candidate for the spectroscopic identification of micro-organisms.

RAMAN SPECTROSCOPY

Another class of vibrational spectroscopy is Raman spectroscopy. Raman spectroscopy is set apart from IR and fluorescence spectroscopy by using light scattering rather than light absorption or fluorescent emission to probe the vibrational modes of the molecular bonds of a sample. Because the probing light does not have to be absorbed, Raman spectroscopy is not limited to the spectral range matching the probed vibrational states, allowing it to take full advantage of absorption minima in the surrounding media. A drawback however is that Raman scattering is a very weak effect with only few photons being Raman scattered. It is this drawback that has ensured IR spectroscopy's popularity over Raman spectroscopy. However, in the case where strongly absorbing media, such as water, are all but unavoidable, Raman spectroscopy has the better cards. There are many variations of Raman Spectroscopy with different trade-offs between drawbacks and benefits. The one with the optimal trade-off for our purposes is laser tweezers Raman spectroscopy.

1

1.3. LASER TWEEZERS RAMAN SPECTROSCOPY

Laser tweezers Raman spectroscopy or LTRS is the combination of Raman spectroscopy with optical trapping and a spectroscopic technique for the identification of micro-organisms. The basic requirement for both Raman spectroscopy and laser tweezing is having a high local optical field intensity. Because of this, a Raman spectroscopy setup requires only little modification to be capable of optically trapping suspended particles. Adding laser tweezing to a Raman spectrometer provides significant added value to the system, especially for single cell Raman spectroscopy (SCRS). Instead of immobilizing cells by drying them on a substrate[12, 13], the cells can be held, manipulated and inspected in a medium suitable to the cell. This prevents the cells Raman spectrum from changing [14] due to the immobilization process while simultaneously reducing the sample size to its smallest possible unit. This approach is possible because of the ability of Raman spectroscopy, in contrast to other spectroscopic techniques, to obtain a vibrational fingerprint spectrum with a single excitation wavelength. Exploiting this, Raman spectroscopy can be performed within a spectral window of low absorption and sample damage. Another benefit of using LTRS for SCRS is the possibility to examine mixtures of cells without prior purifications steps such as platting, something that would not be possible with bulk Raman spectroscopy.

A well-designed LTRS can be a desktop appliance, only slightly larger than a standard microscopy setup. Depending on the sophistication of its microfluidics, the capturing of cells and the acquisition of Raman spectra can be done manually or fully automated. In combination with software-based identification of the Raman spectra, such an instrument would reduce microbiological identification from a task requiring significant biological or chemical expertise to one requiring only a day worth of training.

The following two subsections will treat the theory of Raman spectroscopy and laser tweezing in sufficient detail to understand the remainder of this PhD thesis.

1.3.1. RAMAN SPECTROSCOPY

The discovery of the Raman Effect is attributed to C. V. Raman and K. S. Krishnan who published their discovery in 1928 [15]. The Raman effect is a form of inelastic light scattering (i.e. scattering with energy transfer) that carries information about the vibrational modes of the scattering molecule and forms the basis of Raman spectroscopy. To fully explain the workings of this energy exchange a quantum mechanical treatment of the Raman effect is required. However, for an operational understanding of vibrational Raman spectroscopy as is required to use Raman spectra, it suffices to understand the frequency dependency of the Raman effect and to have a basic understanding of the processes that give rise to the intensity differences found in Raman spectra. Therefore, we will shortly discuss the classical treatment and the quantum mechanically determined scattering cross-section[16]. For a more detailed treatment of the Raman effect the reader is referred to “The Raman Effect” by Derek Long [16].

In both the classical and quantum mechanical treatment of the Raman effect, the scattered radiation is treated as originating from the oscillating dipole induced in the scattering molecules by the incident field. The time-averaged power emitted by such an oscillating dipole per unit solid angle is given by:

$$I_S = \frac{\omega_S^4 p_0^2 sin\theta}{32\pi^2 \epsilon_0 c_0^3}. \tag{1.1}$$

Here θ is the angle between the dipole axis and the direction of observation, c_0 is the speed of light in vacuum and ϵ_0 is the vacuum permittivity. The goal is now to determine how the dipole oscillation amplitude (p_0) and frequency (ω_0) depend on the properties of the scattering molecule. Restricting ourselves to first order induced dipoles we can write:

$$p_0 = \vec{\vec{a}}^{Ray} \vec{E}_0 cos(\omega_i t) + \vec{\vec{a}}_k^{Ram} \vec{E}_0 cos(\omega_i \pm \omega_k \pm \delta_k) t, \tag{1.2}$$

where $\vec{E}_0$ is the electric field amplitude, and ω_i the frequency of the incident radiation. $\vec{\vec{a}}^{Ray}$ is the Rayleigh scattering tensor and is equal to the molecule's polarization tensor in its equilibrium positon. In other words $\vec{\vec{a}}^{Ray}$ is not affected by molecular vibrations and as such the (Rayleigh) scattered radiation retains its frequency, as is clear from the first term of Equation 1.2.

$\vec{\vec{a}}^{Ram}$ is the Raman scattering tensor and is proportional to the molecule's derived polarizability tensor. This means that only vibrational modes that change the polarizability tensor will produces a Raman signal, since only their $\vec{\vec{a}}_k^{Ram}$ will be non-zero. The subscript k in the Raman scattering tensor denotes its dependence on the k-th vibrational mode of the molecule, which has a frequency ω_k and phase factor σ_k. The interaction between the Raman active vibration, with ω_k, and the driving frequency (ω_i), of the incident radiation is given by the cosine in the second term of Equation 1.2. Putting this term in to words, ω_i is the frequency that would be induced in the molecular dipole if it were not restrained by the molecular bond and ω_k is the frequency at which the molecular bond would normally vibrate if unperturbed. As can be seen form, Equation 1.2 the perturbed vibration has either the sum or difference frequency of these two base frequencies. These two options correspond to two different situations and different types of Raman spectroscopy.

In the first situation ($\omega_i + \omega_k$), an already present molecular vibration is perturbed by an incident light wave, causing the molecule to relax to a less energetic vibrational state. In the process, the scattered light will increase in energy and thus be shifted to a shorter wavelength. This is called anti-Stokes Raman scattering.

However, if the scattering event promotes the molecule to a more energetic vibrational state ($\omega_i - \omega_k$), either from the ground state or from an already excited vibrational mode, the scattered light will decrease in energy and thus be shifted to a longer wavelength. This is called Stokes Raman scattering and it is the type of Raman scattering used in this thesis.

Equation 1.2 correctly predicts the frequency dependence of both Rayleigh and Raman scattering. However, it has no way of predicting the observed difference in intensity between stokes and anti-stokes Raman scattering nor does it explain the difference in intensity between different Raman peaks. For this we have to look at a result of the semi classical treatment. The scattering cross-section (σ') is defined as the ratio between the irradiance (F) [1] and the scattered intensity (I_S) (see Equation 1.3).

[1] F is the amount of power passing though a surface perpendicular to the propagation direction in Wm^{-2} [16]

1

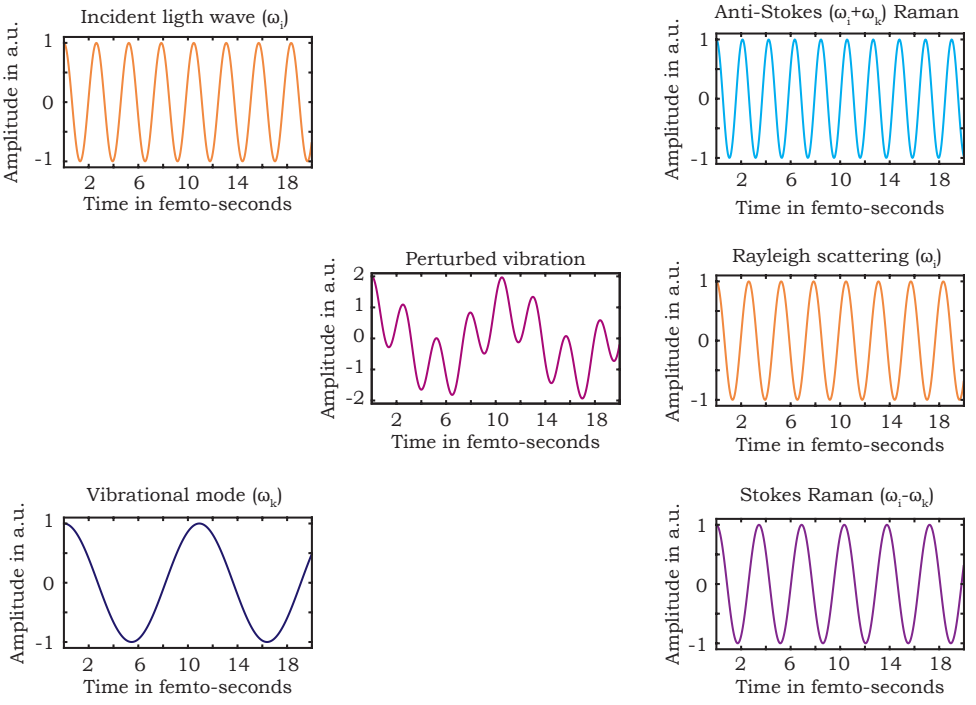

Figure 1.1: Graphical representation of the frequencies involved in Raman scattering. An incident light wave, in this case with a wavelength of 785 nm (top left graph) interacts with a vibrational mode of a molecule, in this case the CH stretch mode (Wilson Number 2) of polystyrene (bottom left graph). This interaction induces a dipole oscillation in the molecule, which resembles the vibrational mode perturbed by the incident light wave (central graph). The oscillating dipole can radiate at two of three different frequencies. In the case that the vibrational mode was already populated the emitted light will have the sum frequency (top right graph) if the vibrational mode is relaxed which is called Anti-Stokes Raman scattering or the same frequency as the incident light (middle right graph) if the vibrational mode remains populated which is called Rayleigh scattering. In the case that the vibrational is mode is not populated at the moment of the interaction, the incident light will be either Rayleigh scattered or will have the difference frequency (bottom right graph) if the vibrational mode is excited which is called Stokes Raman scattering.

$$\sigma' = \frac{I_S}{F} \tag{1.3}$$

The scattering cross-section then given by:

$$\sigma' = \frac{N_{v^i}\omega_s^4 < \vec{\alpha}^2_{v^f v^i} >}{16\epsilon_0^2 c_0^4 \pi^2}. \tag{1.4}$$

Here ω_s is the scattered frequency, c_0 is the speed of light in vacuum and ϵ_0 is the vacuum permittivity. N_{v^i} represents the number of sample molecules in the initial vibrational state. By realizing that the higher vibrational states are populated from the ground state, it now becomes clear that samples will have a higher scattering cross-section for stokes than for anti-stokes shifting transitions, based solely on the population of the required vibrational states. As a result, the stokes Raman signal will usually outperform the anti-stokes signal.

The key variable in Equation 1.4 is the isotropic average of the squared Placzek[17] vibrational transition polarizability tensor ($< \vec{\alpha}^2_{v^f v^i} >$), which is the quantum mechanical analogue of the classical polarizability tensor. In contrast to its classical counterpart, $< \vec{\alpha}^2_{v^f v^i} >$ depends on the specific vibrational transition under consideration: from the initial (vi) to the final (vf) vibrational state. From this, it becomes apparent that each vibrational transition has its own specific scattering cross-section, explaining the intensity differences observed for the different peaks in Raman spectra.

To get a feeling for the strength of the Raman signal it is useful to compare the Raman scattering cross-section with the Rayleigh scattering cross-section, as the Rayleigh scattering will be the dominant contribution to the scattered light. If we compare these cross-sections for N_2[18–20], which is often used as a standard, we find that the Rayleigh scattering is on the order of a thousand times larger than the Raman scattering cross-section. This means that the Raman signal is comparatively weak. Consequently, Raman spectroscopy generally employs strong filters to separate the Raman signal from the Rayleigh signal.

Since the constituent atoms of a molecule and the types of bonds between them determine the vibrational modes of the molecule, Raman spectroscopy can be used to identify both the species of atoms and the types of bonds between them. This is done by determining the shift in frequency between ω_i and ω_s, which is a direct measure of the energy difference between the vibrational modes. This so-called Raman shift is then plotted, traditionally in cm^{-1}. Each peak in the resulting Raman spectrum is then compared to tabulated values [21] to identify the chemical group it originated from. For single molecules or simple mixtures, this allows the molecule to be reconstructed from its Raman spectrum see Figure 1.2. For more complex samples, such as micro-organisms, the individual Raman peaks blend into bands, which can at best be assigned to types of molecules. For these samples, the Raman spectrum functions more as a fingerprint, identifying the sample rather than the molecules present.

The weak signal of the Raman effect can in most practical application be considered crippling. As such, Raman spectroscopy is normally used in situations where other spectroscopic techniques are hampered by strong absorption such as in biological samples where the strong IR absorption of water can easily mask any other signal or cause

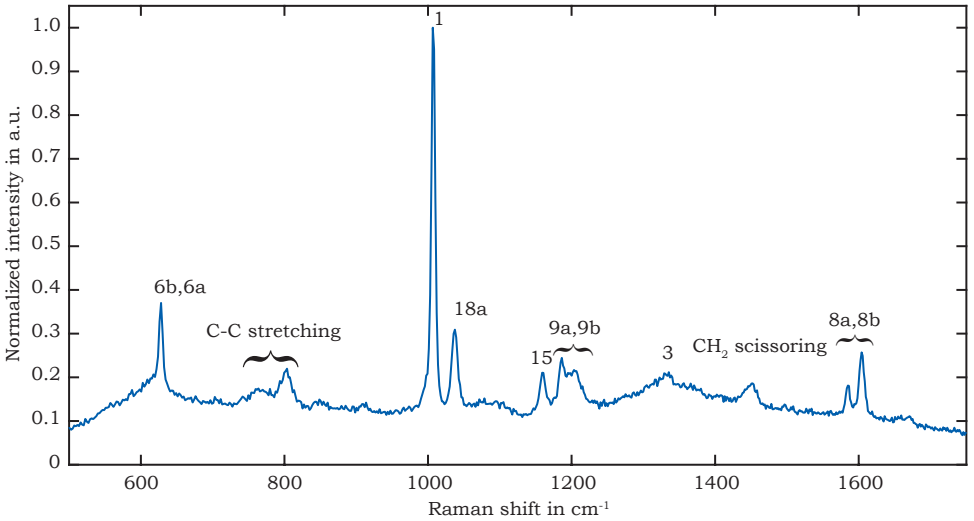

Figure 1.2: Raman spectrum of polystyrene. All save two peaks can be assigned to the various vibrational modes of the benzene moiety of the polystyrene polymer. These peaks have been labelled following the Wilson notation for benzene. [22, 23]. For the different vibrational modes, the reader is referred to appendix A. The two remaining peaks can be assigned to the vibrational stretching mode of the skeletal C-C bonds, for the broad peak around 800 cm^{-1} and the vibrational scissoring mode of the methylene bridge for the peak at 1450 cm^{-1}

damage to the sample. Here Raman spectroscopy can take advantage of the near IR absorption minimum of water, the weak Raman signal of water and the low damage wavelength windows [24]. In these situations, Raman spectroscopy has the additional advantages that it requires little to no sample preparation. In addition it is non-destructive and label-free.

1.3.2. LASER TWEEZERS (OPTICAL TRAPPING)

Optical trapping is a term used for the confinement of particles such as atoms, molecules, or cells to a small volume using optical forces. This technique was pioneered by Arthur Ashkin in 1969 [25]. If free space optical beams are used to exert the required optical forces, the employed devices are usually referred to as optical tweezers. Today's optical traps however also readily use the evanescent fields of waveguides or resonance cavities to trap, usually relative small, particles [26, 27] . Laser tweezers offer researchers the opportunity to precisely manipulate particles from the microscale [28] right down to the nanoscale [29]. This enables for instance the investigation of the forces involved in protein folding and molecular motors, the measuring of DNA transport through nano ports and the stretching and positioning of cells in microfluidic environments [30].

The description of the working principle of optical trapping depends on the size of the trapped particle, relying on considerations of geometrical optics when the particle is much larger than the used wavelength and considering point-dipole approximations when the particle is much smaller than the wavelength. The latter is called the Rayleigh scattering regime. Both these descriptions provide nice conceptual frame works to un-

derstand how optical trapping works (see Figure 1.3).

However, when the trapped particle is comparable in size to the wavelength, as is the case in this thesis with a possible exception of chapter two, none of the aforementioned descriptions is capable of providing accurate results for the forces acting on the particle. In this case a computational approach is required building on the conservation of momentum in electromagnetic fields. Using the Maxwell equations it can be shown that the total flow of momentum P_α through a closed surface S in a direction α is given by:

$$\frac{d}{dt}P_\alpha = \oint_S \sum_\beta T_{\alpha\beta} n_\beta da. \tag{1.5}$$

Here n_β is the normal to the surface S and $T_{\alpha\beta}$ is an element of the Maxwell stress tensor [32]. Using this equation, the optical force on any system enclosed by the surface S can be calculated. Conceptually this can be better understood by realizing that a momentum flow (N) through a surface (m^2) is in units equal to an energy density ($Nm^{-2} = Jm^{-3}$). This means that any volume penetrated by an optical energy density gradient will experience a net force acting upon it, as the momentum flow through its surface will not be balanced.

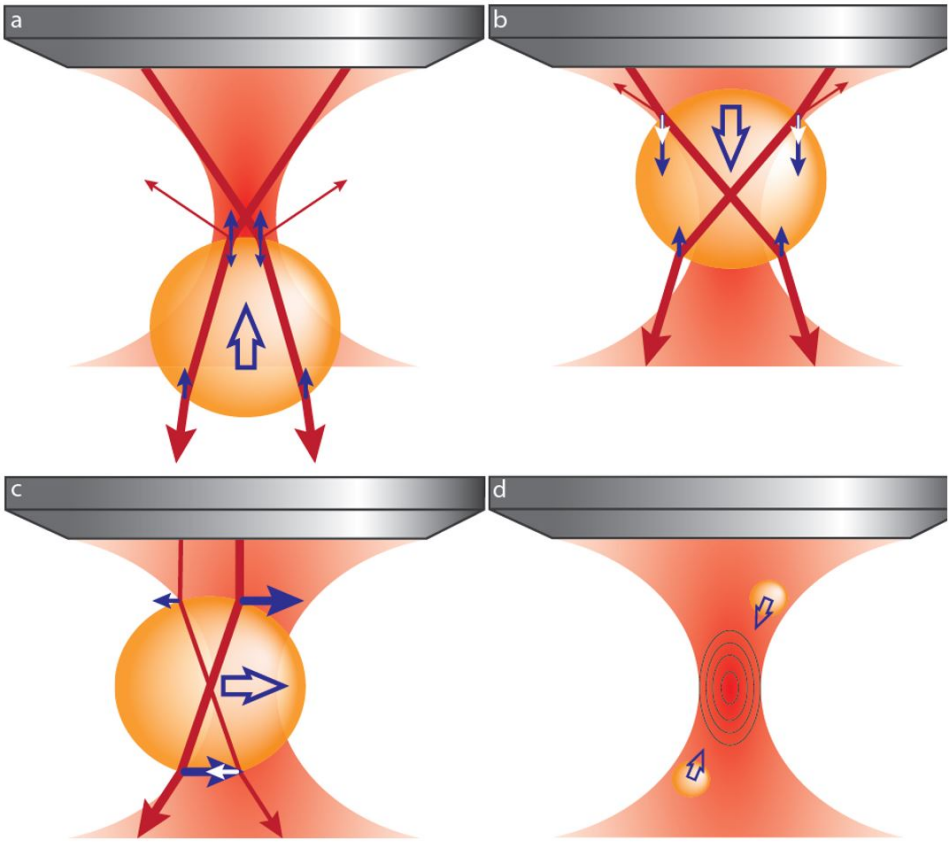

Figure 1.3: Optical trapping, geometric and Rayleigh regime. In these figures red arrows denote light rays, blue and white arrows indicate imparted momentum, open arrows indicate net momentum and closed loops give iso-field lines. The geometrical optical explanation of optical trapping of particles much larger than the wavelength is based on the conservation of momentum between the trapped particle and the refracted and reflected light. In this case, the trapping of a particle can be decomposed in lateral and axial trapping. Axial trapping (a-b) is achieved by the balancing of the momentum transferred to the particle by the refracted light and the reflected light. Lateral trapping (c) results from the asymmetrical refraction and the corresponding un-balanced change in momentum, of light by a particle in an optical gradient. In both cases, a tighter focus produces a stronger trap although axial trapping is the most sensitive to this effect. The particle in this illustration is assumed to be of higher refractive index than its surroundings. In the Rayleigh scattering regime where the particle is much smaller than the wavelength (d) it can be treated as an induced dipole minimizing its energy by placing itself at the focus of the optical gradient. Figure based on Dholakia et al. [31]

1.4. LAB-ON-A-CHIP

The ability to hold, sense and identify single cells is a major advantage of LTRS systems. However, it also is large potential weakness, since the identification of a single cell might very well provide inconclusive results concerning the contamination of a sample. If the extent of a possible contamination of a sample is to be investigated, a representative number of cells will have to be trapped and investigated per unit sample. In this case, the sequential process measuring trapped cells can quickly lead to large overall measurement times. The obvious solution for this problem is parallelization.

Miniaturization and parallelization of laboratory processes is the aim of lab-on-a-chip (LOC) research [33, 34]. Such an approach would reproduce a couple of laser tweezers Raman spectrometers in a handheld point-of–care device or even several dozens in the space occupied by one traditional unit [33, 35]. Parallelization reduces the overall measurement time, per sample, with approximately the parallelization factor. Additionally, if these chips are designed to be mass producible a cost reduction comparable to that found in the CMOS industry can be obtained. Because the full integration of a system including light sources, spectrometers and fluidic pumps on a chip is very challenging, it is customary to already talk about a LOC system when only partial integration of a system is achieved. Considering this, both optical trapping and Raman spectroscopy have, separately, been achieved in LOC systems. In essence, all these systems integrate a fluidic channel, used for sample delivery, with optical structures to provide the required light and sometimes to collect the produced signal.

A good example of LOC Raman spectroscopy is provided by Ashok et al. [36, 37]. Using a polydimethylsiloxane (PDMS) chip they aligned two fibres into an orthogonal geometry to perform what they call waveguide confined Raman spectroscopy. One fibre is used to illuminate a small region with the fibre-delivered excitation light, while the other fibre is used to collect the generated Raman signal. The box created by the two orthogonal fibre facets serves as a turn in the fluidic channel, which delivers either dissolved samples or samples confined to micro droplets to the excitation/acquisition area. The main advantages of waveguide-confined Raman spectroscopy compared to standard Raman microscopes are its reduced background generation and collection, improved collection efficiency and its compatibility with other LOC techniques [36, 37]. The clever fluidic design in this work forces all material in the fluidic channel through the combined excitation/acquisition volume. This is all the sample confinement needed when using dissolved samples and is already reminiscent of a trap, but falls short when applied to particles that are small compared to the channel dimensions, such as cells.

LOC optical traps take the form of either evanescent field traps or waveguide traps with the latter being prevalent. Dual-waveguide optical traps are in essence a waveguide variety of the opposing beams trap demonstrated by Ashkin [25]. Instead of using free-space optics, waveguides or fibres are used to produce two, usually diverging, counter-propagating beams. The overlap between these beams creates a local energy density extreme, which acts as the trapping site. In the case that the beams interfere with each other, a single set of beams can even produce an energy density landscape with several localized extremes each of which can act as a trapping site. This approach using fibres was first demonstrated by A. Constable et al. [38]. A good example of the application of an LOC optical trap is the cell stretcher by Faigle et al. [28]. Using a glass

chip Faigle et al. aligned two fibres perpendicular to a fluidic channel and coaxially with respect to each other. The counter-propagating beams trap set up in this way was used to deform or stretch cells. Using a camera to monitor the deformation they could, in an automated fashion, detect compliance differences between healthy and unhealthy cells. After detection, the cells were sorted into different laminar flows. With this system, throughputs of up to 100 cells per hour from a population composed of cells treated with the cytoskeletal drug cytochalasin D, the unhealthy cell mimics, and fluorescently stained cells, the healthy cell mimics are achieved. Although the system is very mature, the authors note that it would benefit from additional non-mechanical selection criteria to improve the sorting error of 25.9%.

From the aforementioned two examples the combination of trapping and Raman spectroscopy seems an obvious choice for LOC systems, as it is for free-space devices. Whether fibres or waveguides are used to achieve an LOC LTRS has little to no implication for the operational principles of the system. However, it does have a number of practical implications. Fibre-based systems can be fabricated with relative ease, using equipment available to most laboratories, because the required optical structures are obtained from the fibres. This makes them readily available and well suited to laboratory practice. Consequently, fibre-based LOC LTRS systems have been achieved [39, 40] ahead of the waveguide-based versions. The main fabrication issue for fibre-based systems is usually the positioning of the fibres. Although this challenge can be readily met, it remains a task ill suited for mass fabrication. Waveguide-based traps on the other hand require access to a foundry or cleanroom for fabrication and are therefore costly and labour-intensive to obtain, significantly limiting their user base. However, once a design has been finalised the production can, in principle, directly be turned into mass production. As such, fibre-based traps will be predominant in research, but waveguide-based traps should be expected to prevail in applications.

For the mass production of waveguide-based traps, it is very attractive to be able to use the established CMOS infrastructure. This, however, limits the choice of wave guiding platforms to those that can be produced with the materials, techniques and environmental conditions generally used for the production of CMOS electronics [41]. To be able to combine optical trapping with Raman generation the wave guiding platform needs be transparent for wavelengths suitable for the generation of the Raman signal. This requirement is challenging and has led the first systems to use waveguide trapping in combination with free-space Raman spectroscopy [42]. One of the few materials that meet all these requirements is Si_3Ni_4, which provides a high refractive index and low propagation losses in a wide wavelength range. One form of Si_3Ni_4 is the proprietary TripleX platform of LioniX [43].

1.5. TRIPLEX DUAL-WAVEGUIDE TRAPS

TripleX waveguide technology uses thin layers of Si_3Ni_4 embedded in SiO_2 to form waveguiding structures. TripleX waveguides offer a very large transparency range from 405 nm up to 2.35 µm with losses down to 0.1 dB/m (measured at 1550 nm) [44]. In addition, it offers a high contrast in refractive index allowing bending radii down to 70 µm [43] and it is CMOS compatible. These properties make TripleX waveguides suitable for a broad range of applications ranging from telecom to bio-sensing. Because of these properties, TripleX was chosen for the fabrication of the LOC LTRS system presented in this thesis, to which we further shall refer as the dual-waveguide trap.

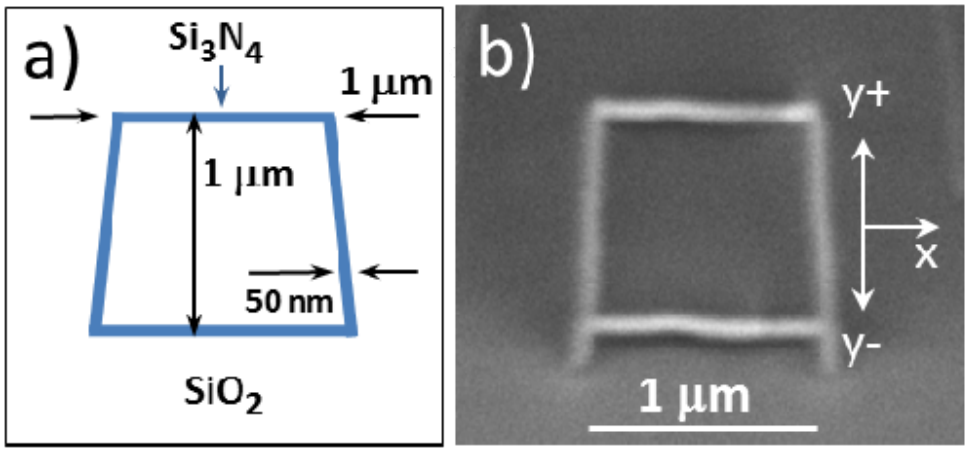

Figure 1.4: TripleX box shell waveguide

TripleX waveguides come in different layouts, all with their own specific properties. For the dual-waveguide trap, the box shell layout was used. This layout consist of a 1x1 μm SiO_2 core surrounded by a 50 nm Si_3N_4 shell embedded in SiO_2 (see Figure 1.4). The shape of the waveguide is defined using dry etching, which results in sidewalls sloped at an 82° angle, rather than being perpendicular. The TE_{00} mode of these waveguides has a 0.06 dB/cm propagation loss at 1250 nm and the smallest obtainable bending radius is 500 μm [43, 45].

A LOC consisting of a Y-splitter and two semi-circular waveguides terminating in a fluidic channel, the dual-waveguide trap integrates the free-space optics needed, in traditional setups, to set up the energy density landscape and generate the Raman signal. These traps belongs to the first generation of LOC devices that combine trapping and Raman generation in to a monolithic chip

1.6. RECAPITULATION

Summarizing, an important aspect in increasing our health and safety is the development of new sensors for screening water samples on the presence of microbiological contaminants. The main problem associated with the detection and identification of these microbial contaminants is the time required for purification and multiplication of the target components due to the low concentrations in which these contaminants are found. These steps can be avoided by using spectroscopic identification rather than biochemical techniques. Raman spectroscopy provides a vibrational fingerprint from which particles can be identified. The Raman effect is weak, but rich in information and flexible with respect to its excitation wavelength. When working in an aqueous environment it can take advantage of the absorption minima of water to outperform for instance IR spectroscopy. Optical trapping allows the immobilization of particles without additional preparation steps and provides much added value to and is highly compatible with Raman spectroscopy. Lab-on-a-chip techniques allow for integration and large-scale parallelization of processes, which is all but unavoidable when performing large-scale single cell identification of microbial contaminants. To take advantage of the established CMOS infrastructure for mass production, a CMOS compatible waveguide technology transparent at Raman suitable wavelength is needed. TripleX is such a waveguide technology.

1.7. RESEARCH QUESTIONS

The main research question that we address with the research in this PhD thesis is:

> Can an integrated dual-waveguide trap, as intended by Van Leest *et al.* [46], be realized and used to identify micro-organisms based on their Raman spectrum acquired from an optically trapped single cell?

We decompose this question into the following sub-questions:

1. Are we able to identify micro-organisms based on Raman spectra obtained with laser tweezers Raman spectroscopy and treated by signal processing and pattern recognition?

2. Is an on-chip dual-waveguide trap, fabricated in TripleX, capable of optically trapping individual particles in a microfluidic environment while generating a significant Raman signal from those particles?

3. Is an on-chip TripleX dual-waveguide trap capable of trapping micro-organisms and producing Raman fingerprint spectrum from these?

The aforementioned research questions will be addressed in the remainder of this thesis.

1.8. CONTENT OF THIS THESIS

Following this introduction, Chapter 2 of this thesis will investigate if a conventional laser Tweezers Raman Spectrometer can obtain Raman spectra from the yeast species *Kluyveromyces lactis* and *Saccharomyces cerevisiae* at the single cell level. Furthermore, attempting to identify them will test the quality of these spectra. In the process, a suitable test setup and the required processing techniques are developed for the following chapters.

Chapter 3 presents the dual-waveguide trap and will determine, through simulation and experiment, if trapping potentials of sufficient strength can be generated to trap polystyrene beads inside the microfluidic channel. Whether the used laser intensities are sufficient to generate a significant Raman signal from the trapped beads will also be subject of investigation.

In Chapter 4 the particularities of the acquisition geometry of the LTRS and the dual-waveguide trap will be investigated. Additionally, the differences in the Raman generating properties between four dual-waveguide traps with varying distances between their waveguide facets will be tested experimentally, using a saturated ascorbic acid solution. Furthermore, the origin of a periodic background observed in the ascorbic acid spectra is investigated.

In Chapter 5 two of the four dual-waveguide traps will be used in trapping and Raman generation experiments with biological relevant particles in the form of *Bacillus subtilis* spores. The quality of the obtained spectra will be used to compare the used dual-waveguide traps to benchmarks obtained from literature.

Chapter 6 presents the overall conclusions and will discuss their implications for the main research question. The Outlook will, subsequently, shortly discuss further research suggestions and envision a possible basic architecture for a lab-on-a-chip instrument based on optical trapping and Raman spectroscopy.

2

CLASSIFICATION OF YEAST SPECIES USING SINGLE CELL LASER TWEEZERS RAMAN SPECTROSCOPY: *Kluyveromyces lactis & Saccharomyces cerevisiae*

We applied laser tweezers Raman spectroscopy to classify the closely related yeast species Kluyveromyces lactis and Saccharomyces cerevisiae from measurements at the single cell level. In laser tweezers Raman spectroscopy, optical trapping of a cell and generation of its characteristic Raman spectrum are combined in one laser-beam focus. This enables fingerprinting of a cell's molecular composition in a harmless fluidic environment within minutes. Laser tweezers Raman spectroscopy is considerably faster than well-known biological techniques based on streak plating or PCR, and requires far less biological material. For each yeast species many dozens of spectra, constituting a training set and a test set, were measured. Visual inspection of the spectra showed large intra-species variations obstructing manual division into two classes. Principal component analysis of the training set, containing 128 *K. lactis and* 119 *S. cerevisiae cells, nevertheless indicated separability into classes. Application of a classification rule based on Fisher's criterion subsequently led to successful blind classification of the test-set cells. This yielded a classification accuracy of* 85% *for the* 48 *K. lactis cells and* 79% *for the* 90 *S. cerevisiae cells. Finally, a Kolmogorov-Smirnov test indicated that the difference between the distributions of the species was statistically significant, implying biological origin of the classification. This successful extension of laser tweezers Raman spectroscopy to classification of the aforementioned yeasts*

This Chapter is based on an manuscript inpreparation by:J.T. Heldens, D.K. Leenman, M.A.H. Luttik, P.A.S. Daran-Lapujade, L.J. van Vliet and J. Caro Titled:"Classification of yeast species using single cell Raman tweezers spectroscopy" (2019)

underlines its applicability in microbiology and contributes to the process of its adoption in this discipline. Laser tweezers Raman spectroscopy is not limited to rapid classification of single cells, but may also include e.g. study of cell metabolism.

2.1. INTRODUCTION

Identification of micro-organisms, such as yeasts and bacteria, plays a key role in many applications. These range from purity control of cell cultures to preventing premature spoilage of food [47, 48] to identifying the responsible pathogen of infectious diseases [49, 50]. Usually, the speed of identification is crucial, as the impact of events inevitably increases with time. The impact can be as mundane as financial losses or as tragic as the death of a patient. Consequently, in many fields there is a strong need for techniques offering fast identification.

Bottleneck for identification of micro-organisms employing biological techniques such as streak plating and PCR the time required for preparing the sample and generating sufficient material for identification. In this context Raman spectroscopy, the spectral analysis of light inelastically scattered by a sample placed in the focus of a laser beam, is very promising. This physical technique is fast (a spectrum can be taken within minutes), label-free, and has a species differentiation capability comparable to 16S RNA sequencing, the microbiological "gold standard" [50]. Probing the characteristic vibrational spectrum of the constituent molecules of micro-organisms with a single excitation wavelength, Raman spectroscopy can operate in the near-infrared wavelength window of low photodamage [24], and thus is non-destructive. In addition, only a small number of cells, even down to the single cell level, and simple sample preparation are required. Thus, Raman spectroscopy can turn the identification process from a laborious and time-consuming task in an expensive laboratory setting into a quick and simple microscopy-like exercise.

Rösch et al. [12, 13] performed scanning Raman spectroscopy using a focused laser-beam diameter of approximately 0.7 μm to classify single yeast cells smeared on fused silica slides. Since yeast cells contain many substructures and thus are highly inhomogeneous (as opposed to bacteria), and since the cell size (in this case about 3 μm) exceeded the focal spot, about ten spectra had to be taken at different positions across a cell to obtain an average spectrum representative of the whole cell. This approach convincingly classified three yeast species down to strain level. In an ideal scenario, however, a *single* yeast cell should be identifiable from a *single* spectrum. Furthermore, due to random organelle positions with respect to the focus positions of a scan, scanning Raman spectroscopy inherently leads to random accents of features in the average spectrum of different cells of a strain. This gives an additional widening of the distribution in the parameter space used for identification. Finally, the relatively harsh conditions on a substrate as compared to the natural aqueous environment of yeast induce cell stress affecting the Raman spectrum [14], which can hamper the identification.

A different approach was recently taken by Rodriguez et al. [51], who Raman-classified yeasts associated with wine spoilage. In this study pure culture suspensions with an apparent turbidity were used, causing many cells in the probing volume defined by a 35 μm laser-beam focus to contribute to a single spectrum. This approach resulted in reliable classification of the three tested yeast species down to the strain level (six strains per species). Although this is a clear example of the value of Raman spectroscopy for an industrial setting, this specific implementation using a large focus yielded ensemble averaged spectra over many cells, thus prohibiting identification of cells in an impure suspension, as for example, a sample taken directly from bottled wine.

In the present work, we apply laser tweezers Raman spectroscopy (LTRS) to the single cell classification of *Kluyveromyces lactis* and *Saccharomyces cerevisiae*, two yeast species highly relevant for modern biotechnology [52, 53] that we use here as model microbes. In LTRS, the laser-beam focus generating the Raman signal is also used for optical trapping of the cell in a stressless fluidic environment, so as to first select the cell by trapping and then hold it for Raman spectroscopy. The cell's rotational Brownian motion [54], intrinsically giving orientational averaging of the Raman signal in the focus, yields a truly representative single-cell spectrum. Thus, the shortcomings of the aforementioned implementations [12, 13, 51] are overcome, while full advantage is taken of the discriminatory power of Raman. As for classification, LTRS has so far mainly been applied to bacteria [55, 56], which have a close to homogeneous composition. Here, we successfully extend LTRS to the classification of the aforementioned two yeast species.

2.2. MATERIALS AND METHODS

2.2.1. ORIGIN, MAINTENANCE AND CULTIVATION OF THE YEAST STRAINS

Saccharomyces cerevisiae CEN.PK 113-7D (P. Kötter, Frankfurt, Germany) and *Kluyveromyces lactis* CBS2359 (Centraal Bureau voor Schimmelcultures, Utrecht, The Netherlands) are prototrophic yeast strains. Stock cultures of both strains were grown in shake flasks in 100 mL synthetic medium with 2% (v/v) glucose. Glycerol 30% (v/v) was added to overnight cultures and 1-mL aliquots were stored at −80°C. Synthetic medium used for cultivation was prepared according to [57]. Glucose was sterilized separately for 20 min at 110°C and added to a final concentration of 2%. The cells used for Raman spectroscopy were cultivated in shake-flasks. 100 mL synthetic medium in 500 mL flasks was inoculated with 1 mL of stock culture and incubated at 30°C on an orbital shaker operating at 150 rpm. The cell concentration of the overnight cultures was determined with a Coulter Counter Z2 (Beckman Coulter Nederland BV, Woerden, Netherlands), after which a volume containing 2×107 cells was taken and centrifuged. The resulting pellet was washed in 10 ml isotone Z2 and centrifuged again. The pellet thus obtained was suspended in 20 ml isotone Z2, to yield the sample from which the fluidic cell of the LTRS setup was filled.

2.2.2. LASER TWEEZERS RAMAN SPECTROSCOPY SETUP

The LTRS is schematically represented in Figure 2.1, which includes an image of a trapped single yeast cell. This home-built setup has a Raman laser (Sacher Lasertechnik, GmbH, Marburg, Germany) operating at 785 nm. The light path to the fluidic cell includes a single mode fibre, a beam launcher, a clean-up filter, a beam expander, two dichroic mirrors and a water immersion objective. The objective creates a beam focus of approximately 0.4 µm diameter for trapping and Raman excitation. The so-called illumination volume, where Raman scattered photons are generated, is several times larger than the focal diameter [58, 59]. Backscattered Raman photons are collected by the objective and directed to a Acton LS 785 spectrometer (Roper Scientific, GmbH, Martinsried, Germany) (resolution 5 cm^{-1}) via a dichroic mirror, a confocal pin-hole (diameter 200 µm), a razor edge filter (Semrock Inc. Rochester, NY, USA) and a lens focusing the signal on the spectrometer's entrance slit. Finally, there is a light path for visual inspection of the yeast cells in the fluidic environment, for which we included a light source and a camera. After sample loading and further initialization, the setup was remotely controlled from outside the darkened lab using a LabVIEW program. This enabled performing all steps but the last of the protocol described in the next section without hands-on operating the setup.

The fluidic cell, based on a literature design [60], is formed by sandwiching a piece of 0.15 mm thick parafilm between two 0.15 mm thick standard glass BB024060A1 coverslips (Gerhard Menzel, Braunschweig, Germany) matching the objective's correction range. From the parafilm a strip (3 mm×54 mm) was removed to accommodate the yeast suspension. The sandwich is sealed by heat bonding at 80°C. Then it is clamped between two plates with central holes for optical access. The upper plate accommodates two O-rings to seal the connection to the fluidic ports in the upper coverslip. A cell suspension is loaded from a syringe connected to the assembly, which is mounted on a piezo stage

with x-y-z-positioning. The objective has additional z-translation. A microfluidic flow-control system (Fluigent SA, Villejuif, France) was coupled to the fluidic cell to enable flushing of the system with isotone Z2.

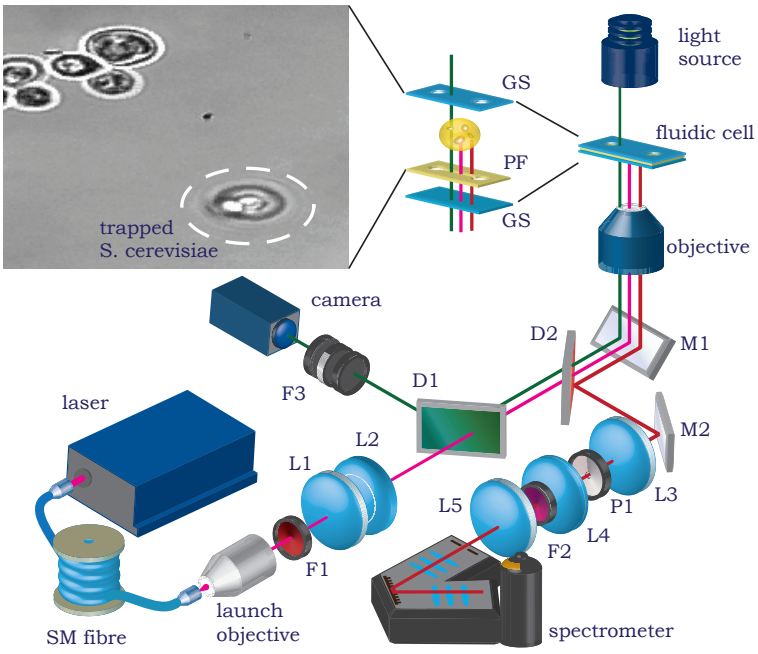

Figure 2.1: Schematic drawing of the laser tweezers Raman spectrometer. Components: SM fibre – single mode fibre, F1 – clean-up filter, F2 – razor edge filter, L1, L2 – lenses beam expander, D1, D2 – dichroic mirrors, L3, L4 – lenses confocal filter, P1 – pinhole, L5 – aperture matching lens, F3 – filter set for camera. For the fluidic cell a zoomed-in view is shown where GS indicates the glass slides and PF the parafilm. The inset shows an image of an optically trapped yeast cell (encircled), adjacent to a group of cells with some of their organelles resolved.

2.2.3. LASER TWEEZERS RAMAN SPECTROSCOPY

The measurements were performed according to a detailed protocol, of which the main steps are the following.

FINDING, TRAPPING AND POSITIONING A YEAST CELL IN THE MEASUREMENT REGION OF THE FLUIDIC CELL

In this step, no attention was paid to the size or shape of the cells or to the presence of a bud, implying that the yeast cells were trapped non-selectively. Having trapped a yeast cell, we vertically translated the fluidic cell, so as to position the glass-fluid interface of the lower cover glass approximately 50 µm below the trapped cell and thus below the laser-beam focus. In this way the Raman background signal in the spectra originating from the cover glass was minimized. Under these circumstances, however, the glass signal still exceeded the Raman signal from the yeast cell.

MEASURING THE RAMAN SPECTRUM OF THE TRAPPED CELL

Raman spectra of trapped cells were measured for the Raman shift range 743 – 1692 cm^{-1}, giving 551 intensity values. The laser power and the acquisition time were chosen to maximize the signal intensity measured by the spectrometer. Resulting laser powers at the objective and resulting acquisition times were in the ranges 9 – 23 mW and 4 – 8 min, respectively, yielding good quality spectra.

RELEASING THE CELL IN THE RELEASE REGION

This step, controlled release of the cell, is to avoid the possibility that one and the same cell would be measured multiple times. To accomplish this the stage was translated until the cell arrived at the edge of the measurement region, where it was released by placing a shutter in the laser beam.

MEASURING THE BACKGROUND SPECTRUM

The background spectrum was measured after each measurement of a cell spectrum, the only difference being that during a background measurement the trap was empty.

MEASURING A POLYSTYRENE REFERENCE SPECTRUM

The polystyrene reference spectrum, for which we placed a 1.1 mm thick polystyrene slab at the position of the fluidic cell, was measured once a day, to enable correction of a possible drift of the spectrometer.

The measurements were performed to obtain a training set and a test set, acquired as two separately measured sequences of Raman spectra. Contrary to the yeast cells for the training set, the cells for the test set were measured blindly. More specifically, from day-to-day the species in a sample for the test set was randomly chosen and before Raman-based classification only known to the authors at the Department of Biotechnology.

2.2.4. SPECTRA ANALYSIS

The measured spectra were pre-processed with the following steps:

- Removal of spikes due to cosmic rays
- Correction, if necessary, of the raw yeast and background spectrum for spectrometer drift using the peak positions in the daily polystyrene Raman reference spectrum
- Normalization of both the raw yeast and background spectrum with respect to their respective mean intensity
- Subtraction of the background spectrum from the raw yeast spectrum, to obtain what we call the direct spectrum (to be discriminated from the derivative spectrum obtained in the next step)
- Calculation of the first derivative of the yeast spectrum

The derivative spectra were used for further analysis instead of the direct spectra to diminish the influence of slowly varying signals, which do not originate from the yeast but remain after the background-subtraction procedure.

The training set was analysed with principal component analysis (PCA), performed with the statistical pattern recognition toolbox for Matlab (version 2.10; Faculty of Electrical Engineering, Czech Technical University Prague, [http://cmp.felk.cvut.cz/cmp/software/stprtool/]).

Following the procedure of Vogt [61], the appropriate reduced number of principal components (PCs) was determined from the so-called lack of fit between the pre-processed spectra and the spectra reconstructed from a reduced number of PCs. The ratio of the residual variances of the reconstructed and pre-processed spectra was used as a test statistic for an F-test to find, per spectrum, the smallest number of PCs that produces a non-significant lack of fit [61]. As the reduced number of PCs we chose the number needed to describe all spectra in the training set with a non-significant lack of fit. This reduction of the number of PCs also suppresses non-descriptive signals and noise in the spectra.

To classify the spectra of the test set we constructed a classification rule from the training set based on Fisher's criterion [62]. The quality of the classifier was then assessed by determining the classification accuracy on the test set. Finally, a Kolmogorov–Smirnov test [63] was performed on the test set to confirm the assumed spectral independence of the yeast species.

2.3. RESULTS

We generated a training set containing the Raman spectra of 128 *K. lactis* and 119 *S. cerevisiae* cells and a test set containing the Raman spectra of 48 *K. lactis* and 90 *S. cerevisiae* cells, measured over a period of 88 and 30 days, respectively.

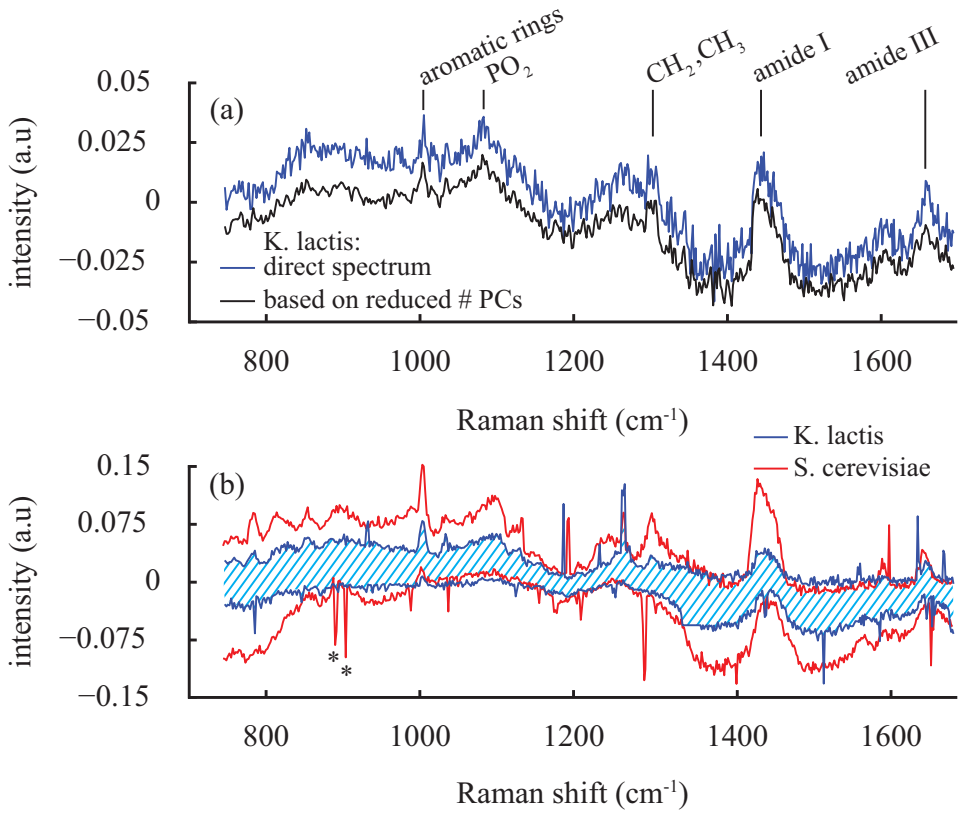

Figure 2.2: (a) An example of a direct *K. lactis* spectrum (blue) and the corresponding spectrum reconstructed from the reduced number of PCs used the analysis (black). The Raman bands indicated by vertical lines (solid or dashed) agree with Raman bands found in yeast by [13, 51, 64] and have been associated with the indicated molecules. Solid lines have in addition been found by [65]. (b) Envelope spectra of *K. lactis* (blue) and *S. cerevisiae* (red). The envelopes are constructed from the training spectra by taking for each Raman shift the highest and the lowest intensity. Some sharp peaks, for example the two negative peaks indicated with an asterisk (∗) are residual cosmics. The hatched area indicates the overlap between the envelope spectra, showing that the *S. cerevisiae* envelope largely encloses the *K. lactis* envelope.

An example of a direct Raman spectrum of *K. lactis* from the training set is presented in Figure 2.2 a (upper curve). The Raman bands centred at 782, 813, 1005, 1300, 1450 and 1660 cm^{-1} have been reported for *S. cerevisiae* by others as well [13, 51, 64] and have been associated with RNA, proteins, lipids and primary amides, for most in accordance with the vibrational transitions of these compounds tabulated in [65]. Observation of these bands is not hindered by the sub-optimal signal-to-noise ratio arising from

the relatively small Raman signal as compared to the background. The occurrence of a negative intensity above approximately 1200 cm^{-1} is due to small deviations of the subtracted background from the actual background. To minimize the influence of the slow transition towards negative intensities at larger Raman shifts on the classification we use the derivative spectra.

From visual peak-to-peak comparison of spectra as in Figure 2.2a, for each yeast species, it was found impossible to classify the measured yeast cell. This finding is illustrated in Figure 2.2b, where envelope spectra are plotted. These spectra were constructed for each species from the 128 and 119 spectra in the training set by taking for each Raman shift the highest and the lowest intensity. Some sharp peaks, for example the two negative peaks at approximately 900 cm^{-1}, are residual cosmic rather than Raman peaks, which could not be removed with our automated procedure without deteriorating the Raman spectra. The envelope spectra of each species indicate strong intensity variation of the individual spectra. This may reflect the heterogeneity of the yeast cells regarding the cell-cycle phase, of which signatures have been observed in Raman spectra before [66, 67]. From the figure it is apparent that the *S. cerevisiae* envelope largely encloses the *K. lactis* envelope, as shown by the hatched area. This indicates that the spectral difference between cells of one species is often larger than the difference between species and illustrates the impossibility to classify cells based on peak-to-peak comparisons. Therefore, we investigated possible systematic differences between spectra of the yeast species with PCA.

The reduced number of PCs, determined according to the Vogt procedure, amounts to 126 out of 247. The effect of the reduced number of PCs on an individual spectrum is demonstrated by the black spectrum of Figure 2.2a, which results from the red spectrum after reduction and reconstruction. When comparing both spectra, it is seen that the procedure reduces the noise while maintaining the characteristic Raman signatures.

In the three-dimensional (3D) subspace spanned by the first three of the 126 PCs, two distributions corresponding to the two yeast species can be discerned, pointing towards separability of the species. Based on this assessment Fisher's criterion was employed to define the following linear classification rule:

$$\vec{w}^T \vec{x}_{test,i} + w_0 \begin{cases} > 0: & \text{assign } \vec{x}_i \text{ to the class of } S.cerevisiae \\ < 0: & \text{assign } \vec{x}_i \text{ to the class of } K.lactis \end{cases} \tag{2.1}$$

Here $\vec{w}^T \vec{x}_{test,i} + w_0$ is a linear classifier acting on the vector $\vec{x}_{test,i}$ representing a spectrum i ($i = 1 \cdots 138$) from the test set, in the 126D PCA sub-space. The vector $\vec{w}$ represents the direction of maximum separation between the classes and the threshold value w_0 acts as separator. Both $\vec{w}$ and w_0 were calculated using the 247 vectors $\vec{x}_{training,i}$ derived from the training set. The classification accuracy was determined by classifying the cells from the test set. The resulting classification is shown in Figure 2.3, where cells classified as *K. lactis* are located to the left and cells classified as *S. cerevisiae* to the right of the dashed green line. From this classification of the 138 cells it was determined that the constructed classifier has a classification accuracy of 85% (0.05%) and 79% (0.04%) for *K. lactis* and *S. cerevisiae*, respectively, where the percentages in between brackets are the standard deviations.

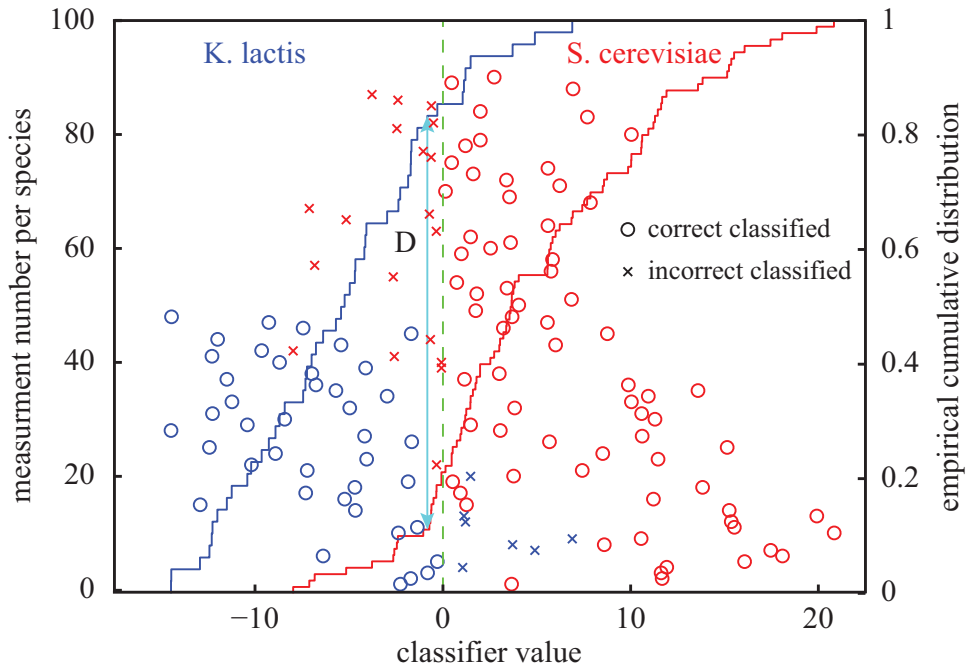

Figure 2.3: Linear classification of 48 *K. lactis* (blue) and 90 *S. cerevisiae* (red) test spectra. Circles denote correctly classified spectra, crosses incorrectly classified spectra. The classifier value is noted along the horizontal axis. The position of the data points with respect to the vertical dashed line at zero classifier value indicates their classification, with negative values corresponding to *K. lactis* and positive values corresponding to *S. cerevisiae*. The two empirical cumulative distributions, (solid lines), refer to the right vertical axis. The maximum vertical deviation D between the distributions amounts to 0.72 and is indicated by the double arrow.

To establish that the two distributions of yeast spectra found in Figure 2.3 are not due to chance in the picking of samples from a single distribution, we projected the 126D PCA space on the direction of maximum separation $\vec{w}$, and subsequently used the two-sided Kolmogorov-Smirnov (KS) test. The KS-test compares the empirical cumulative distributions (solid lines in Figure 2.3) by the maximum vertical deviation D as a function of the Fisher criterion as the test statistic. The value of the test statistic D is 0.72, as indicated by the double arrow in Figure 2.3. The KS-test performed for $D = 0.72$ and for the 48 *K. lactis* and 90 *S. cerevisiae* cells showed that the distributions differ to a significance level better than $\alpha = 0.01$ (critical value for D is 0.29), i.e. the difference is statistically significant. Stated differently, this result proves that the separation of the distributions has a microbiological origin and is not due to chance in the picking of samples from one single population. Thus, the aforementioned percentages for the classification accuracy also originate from microbiological differences between the two yeast species as obtained with LTRS as a classification method.

2.4. DISCUSSION

The central results presented here are: i) blind PCA-based classification of single *K. lactis* and *S. cerevisiae* cells with laser tweezers Raman spectroscopy yields classification accuracies of 85% and 79%, respectively, the related standard deviations being small and ii) demonstration of the statistical independence of the distributions in the PCA space describing the spectra of the two types of yeast cells.

S. cerevisiae and *K. lactis* are closely related ascomycetous budded yeasts that share a similar life cycle: they harbour two mating types, an haploid and a diploid state. *K. lactis* morphologically looks like a smaller version of *S. cerevisiae* [52]. While very similar, these yeasts have some specific traits. Evolving from a common ancestor, these two yeasts diverged ca. 100 million years ago following a whole genome duplication (WGD) [68]. While *S. cerevisiae* is a post-WGD yeast carrying 16 chromosomes, *K. lactis* did not undergo a WGD and has a smaller genome spread over 6 larger chromosomes (www.genolevure.org). Beyond this genome divergence, these two yeasts display some metabolic specificities. While *S. cerevisiae* is capable of aerobic fermentation (so-called Crabtree-positive yeast) and can grow under strict anaerobiosis, *K. lactis* is Crabtree-negative and requires oxygen for growth [52]. Conversely, *K. lactis* is capable of utilizing lactose as carbon source and is proficient at protein secretion [69], whereas *S. cerevisiae* is not. These genomic and metabolic differences are likely to give rise to the classifiability reported here on the basis of Raman spectra.

The results have been obtained with a home-built setup of which the fluidic cell leaves room for improvement of the classification procedure, concerning the supply of cells to the trap and the reduction of the background in the spectra resulting from the glass coverslips. The yeast cells tend to adhere to the glass surfaces of the fluidic cell, making them unavailable for trapping. This effect was counteracted by dislodging the cells from the surfaces by using microfluidic flow pulses. This, however, resulted in a relatively long preparation time for the next Raman measurement. A better solution is to avoid adherence to the surface by using a microfluidic sheath around a central flow carrying the cells [70] or glass with an anti-adherence coating [71]. Furthermore, by replacing glass with Raman silent quartz, frequent measurements of the background spectrum according to the protocol will no longer be needed, while an improved signal-to-noise ratio is obtained. Combined, these improvements will considerably reduce the time required to obtain a cell spectrum.

To classify the spectra we used a linear classifier, which turned out to be very well suited to this proof-of-principle work. However, a further refined classification rule can be applied to these data sets. In particular, the assumption that the species can be perfectly separated by a straight line is almost certainly an oversimplification in view of the shape of the distributions in the PCA space. As such, significant improvements in the classification accuracy are to be expected from non-linear classifications schemes.

Since the presented results constitute a strong proof-of-principle argument to use LTRS for yeast classification, it is appropriate to consider the next step towards practical application of the technique. In general, a database of yeast Raman spectra from which the necessary classification rules can be derived, is required. The classification rules should be stable over long periods of time and transferable between Raman systems. In the present case, the training set and test set were measured over a period of

88 respectively 30 days, after which the classification rule turned out to be no longer valid. Therefore, the estimated temporal stability of the classification rule is between 30 and 118 days, which we consider a respectable time for an experimental setup. We attribute the breakdown of the validity of the classification rule to slow drift of the optical alignment of the setup. We expect that some sort of PCA sub-space calibration based on the Raman spectra of reference materials can stabilize the classification rules and make these transferable between LTRS systems. In this context we note that a commercial LTRS system based on a microscope, which has a compact and solid body, is more stable than our experimental setup, implying that drift in the alignment is inherently much smaller.

Since LTRS is an extension of a laser-tweezers system, of which various realizations are on the market, a logical step for vendors of laser tweezers is to add Raman functionality to their system. The NanoTracker 2 (`http://www.jpk.com/index.2.en.html`), based on an inverted microscope, is an example of such a commercial turnkey system that gives a wide community access to a variety of Raman applications at the single-cell level.

2.5. CONCLUSIONS

Using laser tweezers Raman spectroscopy at the single-cell level, we demonstrated the classification of the closely related yeasts *Kluyveromyces lactis* and *Saccharomyces cerevisiae* with classification accuracies of 85% (σ = 0.05%) and 79% (σ = 0.04%), respectively. Since direct visual evaluation of the Raman spectra failed to classify the two species, a classification rule based on Fisher's criterion was defined, enabling an unambiguous and robust classification. The statistical significance of the difference between the distributions, derived from a Kolmogorov-Smirnov test, proves that their separation has a microbiological origin related to the genomic and metabolic differences between these yeasts. Our hypothesis concerning the cell-phase origin of the intra-species spectral variation can be tested by searching for signatures of the different cell phases under well-controlled conditions. This study demonstrates that laser tweezers Raman spectroscopy is a powerful tool for the rapid classification of yeasts, which can even be extended to mixed samples, and will most likely become of increasing importance in modern microbiology.

2.6. ACKNOWLEGDMENTS

This work was performed in the cooperation framework of the Wetsus centre of excellence for sustainable water technology (`www.wetsus.nl`). Wetsus is co-funded by the Dutch Ministries of Economic Affairs and of Infrastructure and Environment, the European Union Regional Development Fund, the Province of Fryslân and the Northern Netherlands Provinces. The participants of the research theme sensoring of Wetsus are gratefully acknowledged for fruitful discussions and financial support.

The authors gratefully acknowledge P. de la Torre Cortes and T. Vos of the Department of Biotechnology of Delft University of Technology for preparing the many cultures, an activity generously facilitated by the Department's MSD staff.

The authors thank S. R. van Vliet for his skilful operation of the LTRS system and extensions of the LabView program.

3

ON-CHIP OPTICAL TRAPPING AND RAMAN SPECTROSCOPY USING A TRIPLEX DUAL-WAVEGUIDE TRAP

We present a new approach to the dual-beam geometry for on-chip optical trapping and Raman spectroscopy, using wave-guides microfabricated in TripleX technology. Such waveguides are box shaped and consist of SiO_2 and Si_3N_4, so as to provide a low index contrast with respect to the SiO_2 claddings and low loss, while retaining the advantages of Si_3N_4. The waveguides enable both the trapping and Raman functionality with the same dual beams. Polystyrene beads of 1 μm diameter can be easily trapped with the device. In the axial direction discrete trapping positions occur, owing to the intensity pattern of the interfering beams. Trapping events are interpreted on the basis of simulated optical fields and calculated optical forces. The average transverse trap stiffness is 0.8 pN/nm/W, indicating that a strong trap is formed by the beams emitted by the waveguides. Finally, we measure Raman spectra of trapped beads for short integration times (down to 0.25 s), which is very promising for Raman spectroscopy of microbiological cells.

This Chapter is published as: Boerkamp, M. et al., 2014. On-chip optical trapping and Raman spectroscopy using a TripleX dual-waveguide trap. Optics express, 22(25), p.30528

3.1. INTRODUCTION

Today's strong interest in characterization of biological samples with optical methods has initiated several research directions, including classification and identification of biological cells with Raman spectroscopy [72, 73]. With this technique, which comprises the spectral analysis of photons inelastically scattered by a sample placed in a region of highly concentrated monochromatic light, vibrations of the constituent molecules are probed to yield the sample's chemical fingerprint [74]. In laser tweezers Raman spectroscopy, a laser-beam focus for inducing a Raman signal from a microscopic particle in a fluid also serves to immobilize the particle by optical trapping [56, 75], so as to enable building up a sufficient signal-to-noise ratio in the Raman spectrum. In this way one can first select e.g. a biological cell by trapping and then perform Raman spectroscopy on it. These functionalities can be transferred to a lab-on-a-chip situation using a photonic crystal with a cavity [26, 27, 76] or a dual-beam trap [39].

In this context, a very attractive approach is the dual-waveguide trap [46]. In this device microfabricated optical waveguides, from which counter-propagating beams emanate, replace the optical fibres [39] of the dual-beam trap in creating the strong light concentration for onchip trapping and Raman spectroscopy. In [46] we characterize this new design in a simulation study of the optical forces and trapping potentials. Trapping is described as resulting from a force directed transverse and a force directed parallel to the beams, together determining the particle's position in the trap. A salient difference with conventional optical tweezers [77] is that for a dual-waveguide trap with coherently excited modes in either waveguide, the force in the direction parallel to the beams is oscillatory as a result of beam interference [46]. This gives rise to multiple stable trapping positions, a situation similar to that of optical lattices used to study trapped atoms [78].

Dual-beam optical traps have recently been further developed [40, 42, 79, 80]. High quality fibre based traps have been demonstrated, applying fibres solely for trapping [79], and for trapping, Raman excitation and signal collection [40]. However, in view of the delicate mounting of the fibres, this approach does not permit widespread use. The trap reported in [42, 80] is based on microfabricated Ta_2O_5 waveguides. Although this is a very important step forward in view of the fabrication procedure, the research material Ta_2O_5 is not likely to give rise to a general waveguiding platform for sensing. In addition, the Ta_2O_5 waveguides are reported to be lossy [80], thus requiring an additional Raman excitation laser.

Here, we report on a dual-waveguide trapping and Raman device fabricated in TripleX[1] waveguide technology [81, 82], of the monolithic design we proposed in [46]. The box shaped waveguides produced in this technology (Section 3.2) consist of layers of low-loss SiO_2 and Si_3N_4, so as to obtain a low index contrast with respect to the SiO_2 cladding, while retaining the advantages of Si_3N_4. A further property of the waveguides is the low birefringence. The integrated photonics platform based on these waveguides is compatible with CMOS technology, thus automatically fulfilling the requirement for mass fabrication of the device we study here. The waveguides are highly transparent in the very wide wavelength range 405 – 2350 nm, similar to Si_3N_4 waveguides, but contrary to silicon-on-insulator, InP and Ta_2O_5. Therefore, the waveguides can be used at $\lambda = 785$

[1] TriPleX™is a trademark for LioniX's waveguide technology

nm, a standard Raman excitation wavelength, making an additional Raman laser as in [80] redundant. The waveguides used here are to be preferred over Si_3N_4 waveguides because of the low effective index (Section 3.3), which gives beam profiles favourable for trapping and Raman spectroscopy. With our device we successfully trap polystyrene beads and induce a clear Raman effect in the trapped beads.

3.2. DESIGN OF THE DUAL-WAVEGUIDE TRAP AND EXPERIMENTAL SETUP

A cross-sectional schematic of the waveguides is shown in Figure 3.1a. The waveguide has a slightly trapezoidal box shape. The width at the base and the top of the box are 1.1 and 1.0 μm, respectively, while its height is 1.0 µm. The wall of the box is 50 nm thick Si_3N_4. Both the material of the inner region and the surrounding cladding of the box are SiO_2. A cross sectional scanning electron microscope image of a waveguide is given in Figure 3.1b, along with the mode profile of the lowest order TE mode in Figure 3.1c. The profile for this polarization clearly shows the tendency to concentrate the field in the horizontal walls of the box, as expected for higher index regions.

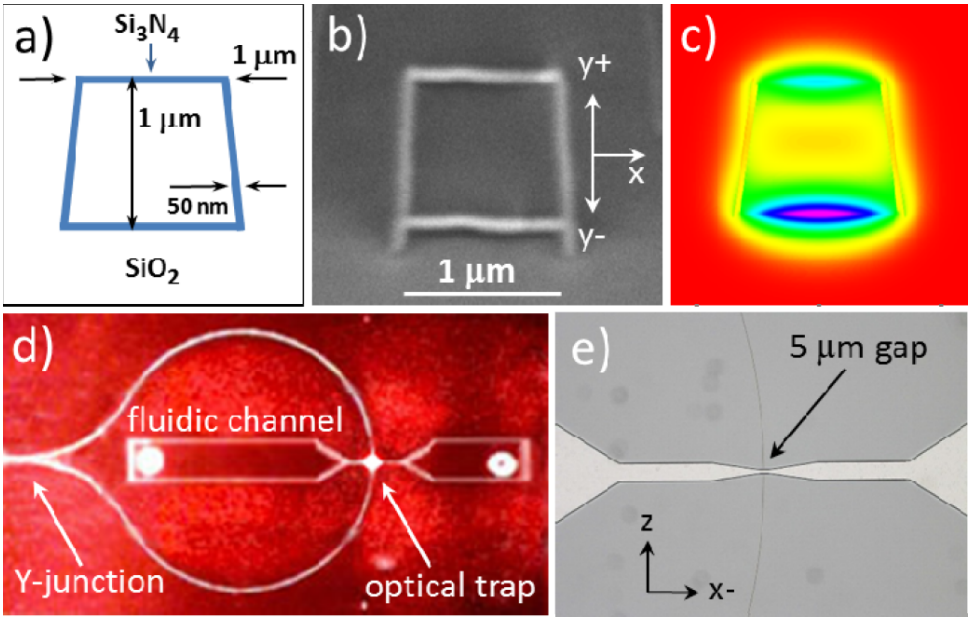

Figure 3.1: (a) Cross-sectional schematic with dimensions and materials of the waveguide. The blue trapezoidal box shape is Si_3N_4. Both the inner region of the box and the surrounding cladding are SiO_2. (b) Cross-sectional SEM picture of a waveguide with the box structure. (c) Mode profile of the lowest TE mode in the waveguide, represented as P_z, the z-component of the Poynting vector. Colours from red to purple indicate increasing values of P_z. (d) Microscope image of the Raman trapping device taken while red light was coupled into the input waveguide to check waveguide continuity, giving the red glow. A 50/50 Y-junction splits the input waveguide in two half-circular arms (circle diameter = 7 mm), which guide the light to the fluidic channel. The waveguiding structures are imaged as white due to saturation of the camera. For clarity, white saturation regions due to scattering loss at the input waveguide and at the trap have been removed. (e) Microscope image of the central region of the device. Each of the two waveguides terminates in a wall of the 5 µm wide fluidic channel, which tapers up in two steps. Definition of the coordinate axes as indicated in b) and e).

The device is fabricated as an assembly of a waveguide, a 50/50 Y-junction and a loop, as can be seen in Figure 3.1d. To create the trapping geometry, a gap is opened in the loop by dry etching successively through the upper cladding (12 μm SiO_2), the waveguide and the lower cladding (8 μm SiO_2). In this way an integrated fluidic chan-

nel and two faceted waveguides, from which counter-propagating beams are launched into the channel, are formed in a single step. The devices are sealed by direct bonding a glass wafer onto the device wafer, with pre-etched holes for access to the fluidic channel of each device. The final step is dicing, which produces a sufficient quality facet of the input waveguide of a device for incoupling of light.

The narrowest section of the channel, located between the waveguides, is 5 µm wide and 20 µm long. Outside this section, the channel tapers up to 1 mm wide in two steps (Figure 3.1e). The coordinate system we use in the following sections is defined by taking x parallel to the fluidic channel axis, y in the vertical direction and z along the waveguide axes (see Figure 3.1b, 3.1e), the trap centre being the origin of the coordinate system.

A schematic of the experimental setup is shown in Figure 3.2. The light source of the

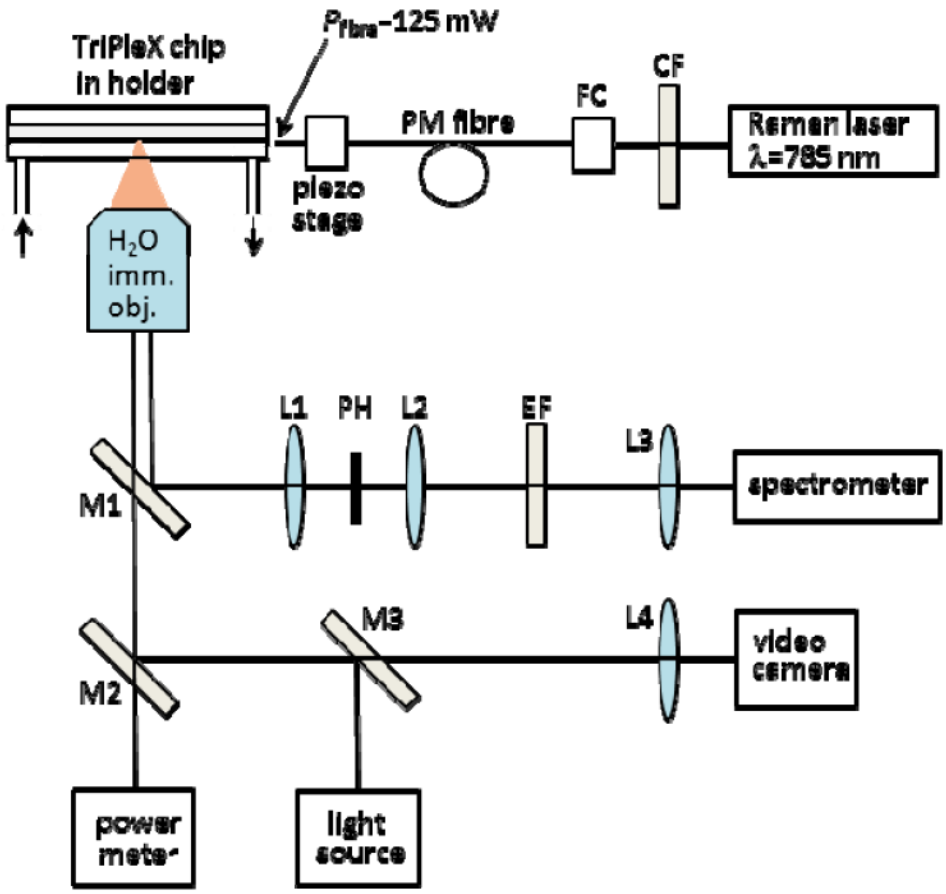

Figure 3.2: Schematic of the setup for optical trapping and Raman spectroscopy with the dualwaveguide trap, which is clamped in a holder with ports for fluidic access. Components: CF - laser clean-up filter, FC - fibre coupler, M1, M2 - dichroic mirrors, M3 - beam splitter, L1, PH, L2 - lenses and pinhole of confocal filter, EF - razor edge filter, L3, L4 - aperture matching lens and imaging lens for spectrometer and camera, respectively. In most of the experiments, the power offered by the fibre to the input waveguide was 125 mW, as indicated.

system is a Sacher Raman laser operating at 785 nm. The light path to the chip includes a laser clean-up filter, a laser-to-fibre coupler and a polarization maintaining single mode fibre. The fibre is butt-coupled to the input waveguide of the device using a high resolution xyz piezo stage, so as to enable optimum excitation of the waveguide's lowest TE mode.

Raman scattered photons generated in a trapped particle are collected by a water immersion objective ($NA = 0.80$) and directed to a Princeton Instruments LS 785 spectrometer (resolution 5 cm^{-1}) via a dichroic mirror, a confocal filter (pin-hole size 200 Si_3N_4 μm), a razor-edge filter and a lens focusing the signal on the spectrometer's slit. Finally, there are light paths for visual inspection and monitoring of the trapped particle(s) and to follow alignment of the fibre to the waveguide, and for measurement of light scattered elastically from the empty trap. For this a LED light source, a beam splitter, a camera and a powermeter are included (see Figure 3.2).

The chip is mounted in a holder comprising a pair of Perspex plates, of which the lower plate has a thickness matching with the objective's working distance of 3.3 mm and which has O-ring seals to the access holes in the chip. The holder, in turn, is mounted on an xy-translation stage. The objective has z-translation. Water with dispersed polystyrene beads is loaded into the fluidic channel from a motorized syringe pump, connected to the holder via peek tubing. Water flow velocities for the experiments, in the range 7-90 μm/s, are obtained by stabilizing the flow without pump activity.

3.3. OPTICAL FIELD OF THE DUAL-WAVEGUIDE TRAP

To characterize the optical field of the device we performed finite-difference time-domain (FDTD) simulations using Lumerical[2] software. In each waveguide the lowest TE mode for $\lambda = 785$ nm is excited. In the simulations coherent modes thus propagate towards the end facets of the waveguides, together delivering 1.0 W of power to the trap. Simulated patterns of the time-averaged intensity of the electric field, both for the xz-plane and the yz-plane, are shown in Figure 3.3.

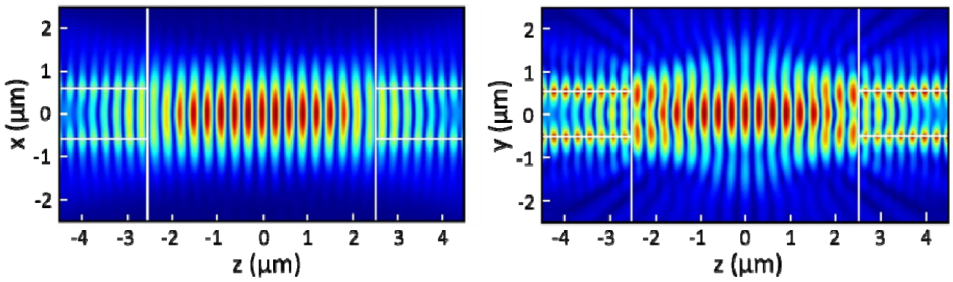

Figure 3.3: Simulated patterns of the intensity of the electric field in (a) the xz-plane and (b) the yz-plane. The pattern results from excitation of the lowest TE mode and shows standing wave modulation due to beam interference. The polarization is in the x-direction.

In this figure, the intensity pattern between the waveguides and inside the waveguides is characterized by standing wave modulation due to beam interference. In the gap between the waveguides the period deduced from the modulation amounts to 299 nm, in close agreement with the expected value $\lambda_{H_2O}/2 = 785$ nm$/(2 \times 1.33) = 295$ nm ($n_{H_2O} = 1.33$). The period of the oscillations in the waveguides is some smaller than in the gap, due to their higher index ($n_{eff} = 1.49$ @ $\lambda = 785$ nm). The clear presence of the interference pattern inside the waveguides indicates that an appreciable fraction of each emitted beam is transmitted into the opposite waveguide, as a result of the low index contrast between the waveguides and water.

For the high field region of the patterns near the optical axis and in the gap, only weak beam spreading is observed, whereas near the facets this region clearly differs for the two cross-sectional planes. This weak spreading is in contrast to the rather strong spreading found for homogeneous Si_3N_4 waveguides [46]. This difference arises from the lower index contrast of the waveguides with respect to water as compared to that of Si_3N_4 waveguides with respect to water (in [46] $n_{Si_3N_4} = 1.9$), resulting in weaker confinement of the guided mode and less diffraction at the waveguide facets.

In the yz-plane, going from guided mode to radiation mode, the profile evolves in a way characteristic of this type of composite oxide/nitride waveguide. In the wave-guide the modal profile has lobes concentrated in the Si_3N_4 walls of the box, which is energetically favourable in view of the polarization being parallel to these walls (i.e. perpendicular to the yz-plane). Outside the waveguide the lobes merge to form a more regular pattern, of which the central high field region is slightly narrower than the correspond-

[2] Lumerical FDTD Solutions, Inc., http://www.lumerical.com/tcad-products/fdtd/ (accessed Nov. 14, 2014)

ing region in the xz-plane. In the xz-plane the profile's evolution from guided to radiation mode is smoother, which relates to the polarization now being perpendicular to the walls (i.e. in the xz-plane).

Details of the highly concentrated optical field in the gap between the waveguides determine several aspects of the optical force characteristics of the device, as discussed in the next section.

3.4. TRAPPING EXPERIMENTS

We clearly observe optical trapping of single polystyrene beads upon their delivery by the flow to the trapping region between the waveguides. A single bead can be kept in the trap for a long time (> 10 min.), provided it does not undergo a head-on collision with another arriving bead, which then may take its place. While being trapped, the bead shows Brownian motion in the optical confinement potential of the trap. When the supply of light to the trap is stopped, the bead is released into the flow. The trap is strong enough to trap more than a single bead, as may be seen in various trapping events recorded in the supplementary Media 1 and Media 2 [3]. Snapshots of these media are presented in the three panels of Figure 3.4, showing one bead in the trap, and two different configurations of five and four beads in the trap. For these trapping events the optical power presented to the input waveguide by the fibre was 125 mW. In Media 1 and Media 2[3] we further observe that a bead can become trapped at various discrete paraxial positions between the waveguides, depending on where it arrives, and that it subsequently may hop to c.q. between what appear to be preferential positions. When several beads are trapped, they may assemble into a lump or into a short chain located on the z-axis (see Figure 3.2b, 3.2c). Assembly of multiple beads in the trap and the related changing configurations can be followed in Media 2[3] .

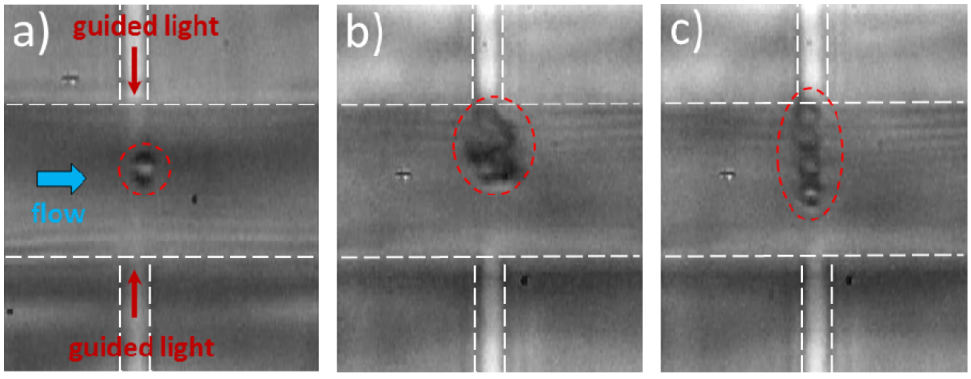

Figure 3.4: Snapshots (a) and (b, c) of the online supplementary Media 1 and Media 2[3] , respectively. A single trapped bead can be seen in a). In b) and c) a lump a five trapped beads and a linear chain of four trapped beads are shown, respectively. The respective water flow velocities for the panels are 90, 34 and 43 µm/s. Dashed lines indicate the boundaries of the fluidic channel and the dual waveguides.

[3]Media 1 and 2 can be viewed at respectively https://doi.org/10.1364/OE.22.030528.m001 and https://doi.org/10.1364/OE.22.030528.m002

3.5. FORCE CALCULATIONS AND OPTICAL POWER CONSIDERATIONS

To calculate the optical forces $F_x(x)$, $F_y(y)$ and $F_z(z)$ in the three directions, we use the electromagnetic fields derived from FDTD simulations, with the bead in position, as input data for the Maxwell stress-tensor method. The mesh sizes used in the bead, the waveguides and the remaining FDTD volume are 5, 10 and 30 nm, respectively. The refractive index used for Si_3N_4, SiO_2 and polystyrene are 2.00, 1.45 and 1.58, respectively. In the simulations the bead position is varied on the x-, y- and z-axis. In view of symmetry, we only use half-axes for the x- and z-direction, but use the full y-axis to study the effect of the asymmetry of the box shape (using the half-axes y+ and y-; see Figure 3.1b). The results are presented in Figure 3.5.

The transverse forces F_x and $F_{y+(-)}$ in Figure 3.5 show the typical restoring behaviour of the gradient force: upon displacement from the trap centre the force pulls the bead back. Further, with increasing displacement the force goes through an extremum, the position of which marks the point beyond which the effective gradient of the field intensity probed by the bead decreases. As for the magnitude of $F_{y+(-)}$ and the position of their extrema, small but discernible differences occur with respect to these quantities of F_x. In particular, the extrema of $F_{y+(-)}$ slightly exceed the extremum of F_x, and occur for smaller displacement than for F_x, whereas for displacements below 0.5 μm the magnitudes of $F_{y+(-)}$ exceed that of F_x. Such properties can be understood from details of the field distribution in Figure 3.3. For example, for small displacements the gradient of the field intensity turns out to be stronger for direction y+ than for direction y-, while this difference becomes negligible for larger displacements. This agrees with the calculated force behaviour. For larger displacements in the x-direction the intensity gradient exceeds the gradient for either y-directions, leading to the larger calculated forces for that range.

From the initial slope of the force curves we determine transverse trap stiffnesses of 0.73 and 0.87 pN/nm/W for the x- and y-direction, respectively (taking the average for y+ and y-). These values amply exceed, by a factor ≈ 25, those for the dual-waveguide trap in[46] based on homogeneous Si_3N_4 waveguides. This is due to the weaker beam spreading in the trap, giving stronger transverse gradients. The values also exceed those of conventional optical tweezers, for which a few tenths of pN/nm/W are reported for the transverse case [77]. It follows that this trap is a strong trap.

The axial force F_z in Figure 3.5 oscillates strongly around zero, with the same period as the intensity modulation in Figure 3.3. The oscillatory force thus reflects the beam interference. Multiple points of stable trapping exist on the periodic curve, characterized by $F_z = 0$ and a negative slope, i.e. for $x = m \times \lambda/(2n_{H_2O}) = m \times 295$ nm ($m = 0, 1, 2, \ldots$), the positions of the interference maxima. Such multiple stable points agree with the experimental observation of several discrete axial trapping positions and hopping between these, discussed in the previous section and illustrated in Media 1[3]. The trap stiffness for F_z related to a stable point equals the slope at a zero crossing of an oscillation, and amounts to 3.8 pN/nm/W. This value characterizes very strong local traps in the z-direction. The envelope of the oscillations has a slight positive slope. This corresponds to a weak force towards the waveguide facets, contrary to the usual direction of

the scattering force for divergent dual beams. We explain this as resulting from the characteristics of the radiation mode emitted by this type of waveguide, in particular to the merging of the lobes as discussed in relation to Figure 3.3b.

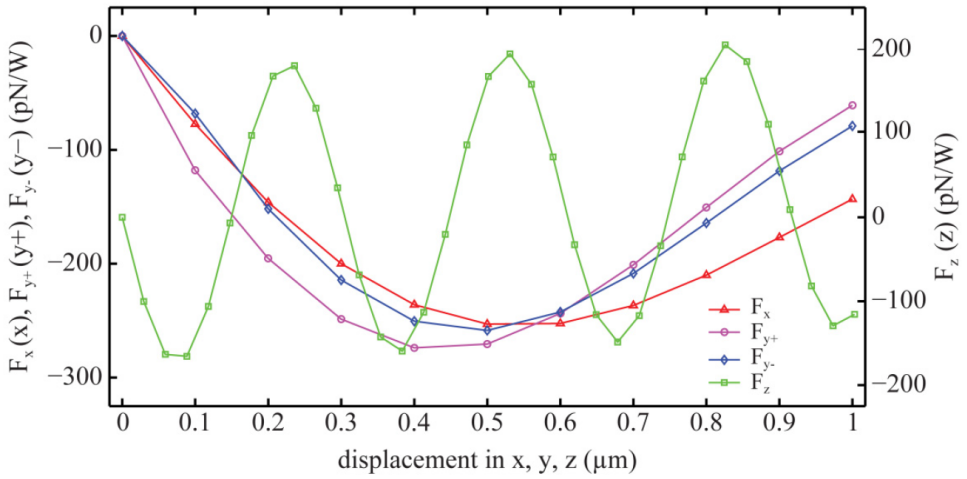

Figure 3.5: Calculated forces F_x, F_{y+} (-) and F_z for displacement of a 1 µm polystyrene bead on the three corresponding axes. The axes y+ (y-) are defined in Figure 3.1b.

The optical power supplied to the trap (P_{trap}), a key figure of merit, cannot be measured directly. Therefore, we derive (P_{trap}) from release experiments. In such experiments (P_{trap}) is lowered by lowering P_{fibre}, the power offered by the fibre, to the value where F_x is just not balanced by the drag force F_d exerted on the bead by the flow. This leads to the bead's release into the flow. At release F_x to a good approximation equals $F_d = 6\pi\eta r v$. Here $\eta = 10^{-3}$ Pa.s is the dynamic viscosity of water, r the bead radius and v the water velocity at release. The water velocity equals the bead velocity immediately after release, which we deduce from the bead position in successive frames of the movie of the release event. The resulting F_x values at release for the various water-flow velocities, which in these experiments take values up to 0.6 pN, correspond to the extremum of $F_x(x)$ in Figure 3.5 (250 pN/W) and thus yield the related P_{trap} values, which are found to range up to 2.4 mW.

Release experiments also yield the relation between P_{trap} and P_{fibre}. We obtain this relation via P_{scatt}, the power of the light elastically scattered from the empty trap into the immersion objective, measured behind dichroic mirror M2 (see Figure 3.2). For the empty trap (i.e. no beads contributing to light scattering) we first obtain as a calibration $P_{scatt}(\mu W) = 17.6 \times P_{fibre}(W)$. Using this, the P_{scatt} values measured just after release give the P_{fibre} values set to just enable release. Note that P_{fibre} is not accessible to direct measurement when the fibre-waveguide alignment is preserved, which we prefer in these experiments. Using the drag force, this in turn gives the relation between P_{fibre} and F_x at release. This, when combined with the aforementioned extremum $F_x/P_{trap} = 250pN/W$, yields $P_{trap}(mW) = 4.1 \times 10^{-2} P_{fibre}(mW)$. The prefactor 4.1 ×

10^{-2} represents the overall transmission, including the fibre-waveguide butt coupling, the Y-junction, the waveguide bends and the straight waveguide sections. Of these the butt coupling to the diced waveguide facets by far induces the highest loss. In most of the trapping experiments P_{fibre} was 125 mW, giving P_{trap} = 5.1 mW (corresponding to F_x = 1.3 pN at release). From conventional laser tweezers Raman spectroscopy it is known that this power level is sufficient for Raman spectroscopy of a trapped bead.

3.6. RAMAN SPECTROSCOPY

We have performed preliminary Raman spectroscopy measurements of a single polystyrene bead optically trapped in the dual-waveguide device, using the setup of Figure 3.2. Example spectra are presented in Figure 3.6, for five integration times in the range 0.25 – 15 s. The spectra have been corrected (see below) for a separately measured background spectrum without bead in the trap. We observe that with increasing integration time distinct peaks develop in the spectra. Raman shifts of a standard spectrum of polystyrene [83], denoted by the eight dashed lines with attached shifts, agree with the positions of the measured peaks. For the peaks close to 1327 and 1450 cm^{-1} there is a small deviation, which is on the order of the spectrometer's resolution. From measurements of 11 μm beads of the same quality as the 1 μm beads with our laser tweezers Raman spectroscopy setup, in which the bead is trapped in the laser-beam focus in water without involvement of the dual-waveguide device, we find similar deviations for these two peaks from the standard spectrum. This proves that the deviation is not due to the dualwaveguide trap and suggests that sample dependent properties are involved. For the 15 s integration time we have included two traces in the figure to demonstrate the repeatability of the measurements in terms of overall spectrum shape, peak positions and intensity. Visual comparison indicates good repeatability with respect to these qualities, quantified by an average difference of 5 per cent as calculated from the raw data, which represent the direct measurements. We conclude from the data set that we measure the Raman spectrum of polystyrene. Above 1700 cm^{-1} and for longer integration times, some structures are present which are not polystyrene related. These could only be partly corrected by the background, due to its specific nature discussed below. We connect the structure in the range 1730 – 1740 cm^{-1} to Perspex, the material of the holder of the chip, of which the spectrum shows a peak at 1736 cm^{-1} [84]. The residual structures at 1900 and 1960 cm^{-1}, clearly present in both the raw spectra and the background, so far remain unidentified, although we note that they occur in the range of Raman signatures of hydrocarbon chains.

The background used for correction was measured during 1 s, further conditions being similar as for the raw polystyrene spectra. Like the spectra, the background has a decaying global behavior with increasing wavenumber, without pronounced structures coinciding with Raman peaks of polystyrene. Multiplicative scaling of the background yields global decays slower than the background of the raw spectra (each having a separate scaling factor), implying that the separately measured background is an approximation of the actual background. This is not surprising, since a raw spectrum's background is affected by the presence of the bead. This serves as scatterer for all light impinging on it and thus also scatters other light than polystyrene Raman light into the objective (fluorescence light and other Raman light). Without bead this other light does not contribute to background to this degree. This is why the spectrum of the empty trap only approximates the actual background, unlike the situation of e.g. micro-Raman on a liquid in a cuvette. In our future research we will study the contributions to the background in more detail. We have used the background to partly remove non-polystyrene signal from the raw spectra. The criterion for the background magnitude is that its integral equals the integral of a spectrum, i.e. the photon count for the background is "by hand" equated to the photon count for a spectrum. Thus, the background's somewhat slower global de-

cay is approximately equally divided over the spectrum. After background subtraction, the result was slightly smoothed using a moving average filter with a four points span, which is comparable to the resolution of the spectrometer, giving the spectra of Figure 3.6. These show negative intensities for higher Raman shifts due to different decays of background and raw spectra. For the interpretation of the spectra this is irrelevant.

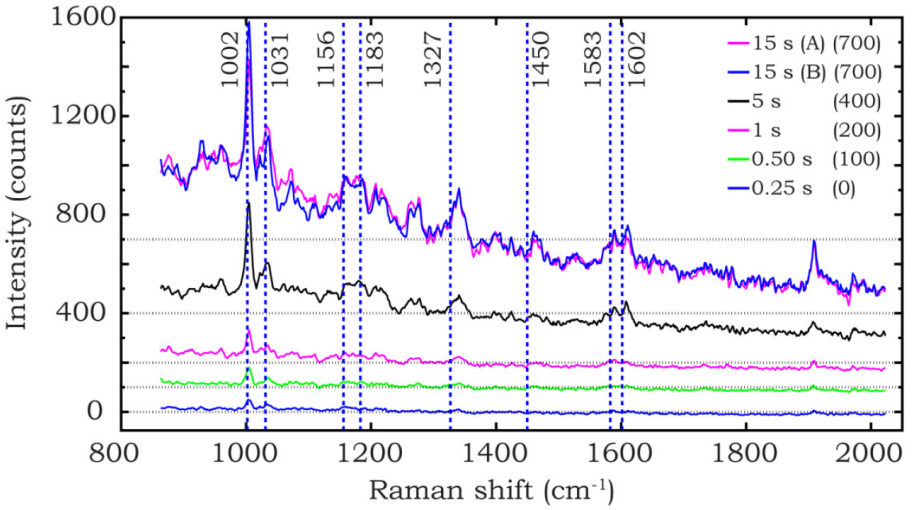

Figure 3.6: Raman spectra of an optically trapped polystyrene 1 µm bead, for integration times as indicated. Ptrap = 5.1 mW. The Raman shifts attached to the dashed lines have been taken from a standard Raman spectrum of polystyrene [83]. From the spectra a background has been subtracted and they have been slightly smoothed, as described in the text. The two 15 s spectra indicated with (A) and (B) demonstrate the repeatability of the measurements. The dotted lines are the axes of the respective spectra, showing that the intensity is negative for higher shifts as a result of the background-subtraction procedure (see text). The numbers in brackets adjacent to the integration times are the vertical offsets applied to the spectra for clarity.

These results proof that this new design of the dual-waveguide trap is not only a powerful device for optical trapping but also for Raman spectroscopy of trapped particles. The Raman peaks at 1002 and 1031 cm^{-1} are still clearly measured for an integration time as short as 0.25 s, while the structures at or close to 1156, 1183, 1327, 1450 and 1602 cm^{-1} are just discernible in the spectrum for a 0.5 s integration time. This is promising for trapping and Raman spectroscopy of bio-objects such as single cells (e.g. bacterial spores and bacteria), which have a relatively weak Raman signal and therefore will unavoidably lead to longer integration times than used here. Such longer times are expected to be very well possible, since our Raman excitation wavelength of 785 nm is in a window of relative transparency of biological material in the near infrared portion of the spectrum (750−1200 nm) where photo-damage and heating of micro-organisms and other cells are limited [77].

3.7. CONCLUSIONS

With a dual-waveguide trap based on waveguides fabricated in TripleX technology, a novel design of the dual-beam trap, we have optically trapped polystyrene beads from an aqueous suspension flowing through an integrated fluidic channel. A transverse trapping force as high as 1.3 pN can be exerted on a bead with a power of 5.1 mW supplied to the trap. Optical force calculations yield 0.8 pN/nm/W for the average transverse trap stiffness and 3.8 pN/nm/W for the axial stiffness of an individual local trapping potential induced by beam interference. These are high values, indicating a strong trap. Apart from particle trapping, the beams emanating from the dual waveguides are capable of inducing the Raman effect in a trapped microparticle, as we demonstrate from measured Raman spectra with a shortest integration time of 0.25 s. We suggest that III-V lasers can be heterogeneously integrated, and arrayed waveguide grating spectrometers based on TripleX technology can be homogeneously integrated with multiple dual-waveguide traps of the type we study. In this way a complete lab-on-a-chip results for in parallel trapping and Raman spectroscopy of multiple microbiological cells.

3.8. ACKNOWLEDGMENTS

The authors gratefully acknowledge the support of the Smart Mix Programme of the Netherlands Ministry of Economic Affairs and the Netherlands Ministry of Education, Culture and Science. This work was performed in the cooperation framework of Wetsus, centre of excellence for sustainable water technology (www.wetsus.nl). Wetsus is co-funded by the Dutch Ministries of Economic Affairs and of Infrastructure and Environment, the European Union Regional Development Fund, the Province of Fryslân and the Northern Netherlands Provinces. The participants of the research theme sensoring of Wetsus are gratefully acknowledged for fruitful discussions and financial support.

4

PREPARING THE SETUP FOR BIO-PARTICLES AND COMPARING THE LTRS AND DUAL-WAVEGUIDE TRAP

4.1. INTRODUCTION

In applications ranging from purity control [47] to the detection/screening of infectious pathogens [49], the identification of yeasts, bacteria and other micro-organisms is essential. As the impact of biological contamination increases with time, there is a need for fast identification techniques. Single cell Laser Tweezers Raman Spectroscopy (LTRS) is a fast alternative to traditional techniques such as streak plating and PCR.

In single cell LTRS a micro-organism is trapped in the focal spot of a laser beam while its Raman spectrum is generated. This Raman spectrum acts as a fingerprint to identify the organism. For traditional techniques the required purification and multiplication steps are the most time consuming. Single cell LTRS is faster mainly because it does not require these steps. However, to characterise a sample many cells have to be identified in a short time. Although the repeat rate is limited by the required acquisition time, this can be achieved by identifying many cells in parallel.

A lab-on-a-chip approach can realize several dozen LTRS systems in the space occupied by one traditional unit, allowing a high degree of parallelization [33]. The dual-waveguide trap, monolithically fabricated in TripleX waveguide technology[43], is a trapping and Raman generating device and first step towards a full-fledged lab-on-a-chip LTRS.

Trapping and Raman generation have been demonstrated with the dual-waveguide trap for polystyrene beads [85]. However, acquiring Raman spectra from biological particles is significantly harder than from polystyrene beads, because of their lower Raman yield. This is mainly due to the – on average – lower density and smaller Raman scattering cross section. In anticipation of this increased difficulty, the stability of the setup as used in Chapter 3 has been improved to reduce signal loss. The improvements are presented in Subsection 4.2.1.

The LTRS and dual-waveguide trap differ in their signal generation and acquisition geometry. These difference lead to subtle changes in the obtained Raman spectra. To better understand these changes, the difference in signal generation and acquisition geometry are presented in Subsection 4.3.1.

Using dissolved ascorbic acid, the signal generation difference between four dual-waveguide traps is investigated in Subsection 4.3.3. These dual-waveguide traps differ in the distance between the waveguide facets in the fluidic channel. As such, they are referred to by this width. The four traps have distances of 5, 10, 15, and 20 µm between their facets.

A periodic background is observed in the spectra obtained from the dual-waveguide traps. The possible origin of this background is investigated in Subsection 4.3.3. The experiments and analyses performed in this section lead to a choice of traps to be used in Chapter 5.

Finally, Section 4.4 reflects on the improvements made to the setup, the experiments with ascorbic acid and the comparison between the LTRS and the different dual-waveguide traps and presents the conclusions.

4.2. METHOD

This section presents the setup as used in this chapter, and the major changes made with respect to the one of Chapter 2 and 3. The aim of these changes is to obtain a higher alignment stability and a better image quality.

4.2.1. THE SETUP

The previous setup (as presented in Chapter 2 and 3) has two main issues leading to instability. The first is that the main beam path, which runs from the fibre launcher to the objective, traverses two dichroic mirrors (D1 and D2 in Figure 2.1 of Chapter 2) resulting in two, angle of incidence dependent, parallel displacements. All further optical components need to follow these displacements, practically fixing the angle of the mirrors. As a result, precise angular control is required in the side arms, in addition to positional control, which increases the setup's sensitivity to alignment drift. The second issue is the early expansion of the Raman laser beam and the refocusing of the beam containing the acquired camera image and Raman signal well beyond the 180 mm infinity space of the objective. Both choices unnecessarily fill the aperture of most optical components, increasing the risk of clipping due to alignment drift. This leads to asymmetrical trapping forces in the LTRS mode and loss of image signal and Raman signal in both LTRS and dual-waveguide trap mode. In the previous setup the image contrast is low because strong reflections of the illumination light on the optical components saturate the camera within the exposure time. This limits the maximum image intensity that can be obtained. Furthermore, some residual structure of the light source is still visible in the produced images due to the long focal length lenses used for the Köhler illumination.

The new setup (see Figure 4.1) uses reflective optics (M D2, D1, and BS) to guide the main beam path, indicated in blue, from the chip holder (CH) to the camera (C). Each section of the beam path can now be fixed individually using pairs of diaphragms, not depicted, set along the beam path. This allows a deviation in angle of the main optical axis to be corrected by these reflective components.

The side arms in this setup are the LTRS arm indicated in red, the Raman arm indicated in purple and the illumination arm indicated in green. The beams of these arms are coupled to the main beam path by traversing D1, D2 and BS respectively. Each arm undergoes a single parallel displacement, which can now be corrected for. This can be done with, for example, the beam expander (L4, L5) in the Raman laser arm. Such corrections are comparatively easy, since the correct alignment can be determined using the diaphragms already present in the main beam path.

The acquired image signal beam and Raman signal beam are contracted and recollimated using respectively lenses L1 and L2 placed within the infinity space of the objective. This simultaneously reduces the required width of the Raman laser beam and the resulting width of the Raman and imaging beam. Additionally, it extends the distance over which the Raman and imaging beams can be considered collimated.

A new halogen lamp with higher intensity allows a diffuser (D) to be used to give a more homogeneous illumination than obtained with only the Köhler illumination. Furthermore, a conjugated diaphragm (DF) is used to restrict the illumination beam to the region of interest in the object plane, thus significantly reducing the amount of light entering the main beam path and hence the amount of back reflected light. The increased

brightness and contrast allow spores to be imaged within the dual-waveguide trap, while previously polystyrene beads already used to be challenging.

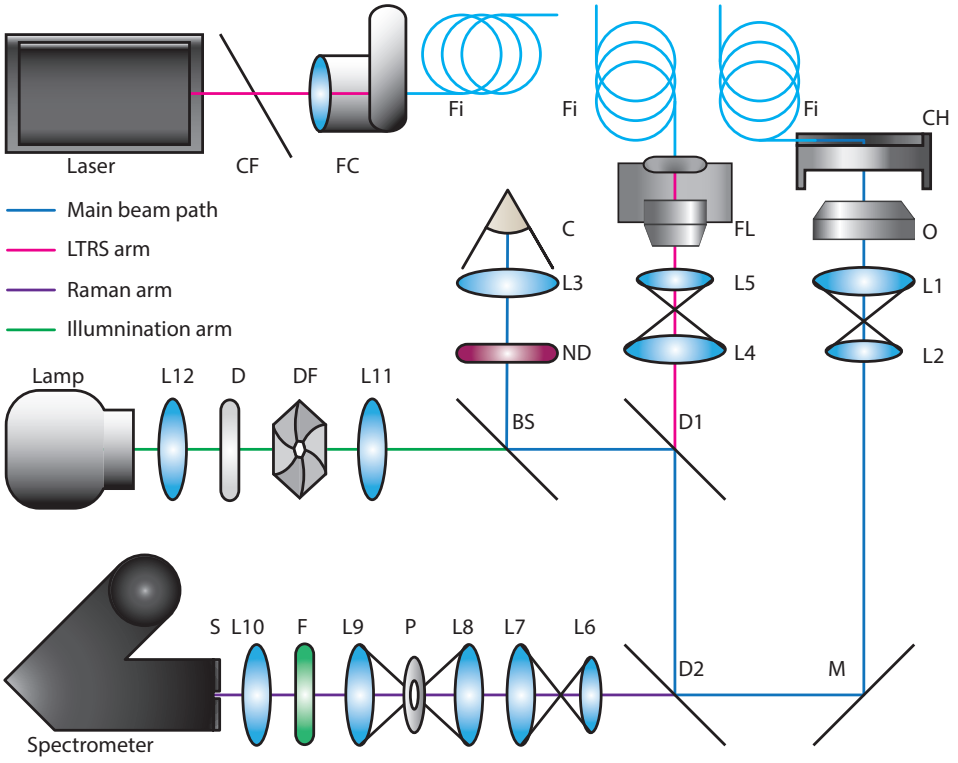

Figure 4.1: Experimental setup used in this chapter. (blue) The main beam path. (red) The LTRS arm. (purple) The Raman arm. (green) The illumination arm. Components: L1-12 - lenses, CF - clean-up filter, FC – Newport 9131-M fibre coupler, Fi - Thorlabs PM-630-HP polarisation maintaining fibre, FL - fibre launcher, C - camera, ND - neutral density filters, Lamp - halogen lamp, D - diffuser plate, DF - diaphragm, BS - 50:50 beam splitter, D1, D2: dichroic mirror, M - silver mirror, O - Olympus UPLSAPO 60XW or LUMPLFLN 40XW objective, CH - chip holder, F - filter, P - pinhole ø=100 µm, S - spectrometer entrance slit, spectrometer Acton LS 785. Lens sets L1/L2, L4/L5 and L6/L7 form beam expanders. L9, P and L8 form a confocal filter.

The use of a new chip holder consisting of a chip shaped cavity in an aluminium drum removes two refractive index transitions and a transition through Perspex, associated with the lid of the old holder, from the main beam path. The new chip holder allows a working distance reduction of 2.5 mm for the dual-waveguide trap mode. However, this is insufficient to use an objective with a higher NA than the one used in chapter 3. The chip holder is mounted on both a manual and a piezo stage to allow positioning relative to the objective and can hold either an LTRS fluidic cell or a dual-waveguide trap chip. The setup is switched from LTRS mode to dual-waveguide trap mode by transferring the fibre from the fibre launcher (FL) to the chip.

4.3. RESULTS

The results section presents a theoretical and experimental comparison of the LTRS and dual-waveguide trap. Furthermore, experimental results and the analysis thereof for the characterization of dual-waveguide systems varying in size from 5 to 20 μm are presented.

4.3.1. RAMAN GENERATION AND ACQUISITION GEOMETRY: COMPARING THE LTRS AND DUAL-WAVEGUIDE TRAP

While the principles of optical trapping and Raman scattering are universal, the geometry in which they are applied still has a large impact on the resulting trapping forces and amount of Raman signal acquired. The specific geometry used for the LTRS and dual-waveguide trap in this chapter is treated below.

The setup used in this chapter has been designed to operate in LTRS and dual-waveguide trap mode and requires minimal adjustment when switching between these modes. The main difference between the modes is that for the dual-waveguide trap the trapping force is generated using on-chip waveguides (see Figure 3.1) rather than free-space optics, as is the case for the LTRS mode. Consequently, the major optical axes are orientated parallel for the LTRS and perpendicular for the dual-waveguide trap. This leads to differences in Raman generation and acquisition geometries between the modes. These differences are best described by looking at the overlap between the Raman generating volume, a sub-volume of the illumination volume, and the acquisition volume.

THE ILLUMINATION VOLUME

In both modes, the laser light used to set up the trapping force is also used to generate the Raman signal. The region with a sufficiently high laser-light intensity to generate a significant Raman signal is referred to as the illumination volume (V_{il}) [58]. For the LTRS the V_{il} has the shape of a diabolo. It is given by a focused Gaussian beam truncated at one Rayleigh length (L_R) above and below focus. The Gaussian beam is focused onto a spot size of diameter $d = 1.22\lambda/NA$ with λ the wavelength of laser light and NA the numerical aperture of the objective. L_R is approximated for high NA objectives as $L_R = 2\lambda/NA^2$ [86]. The radial boundary of the Gaussian beam is customarily defined as the distance at which the intensity equals e^{-2} times the axial intensity [86].

For the dual-waveguide trap, the slightly diverging counter-propagating beams emerging from the waveguide facets define the illumination volume. In this case, the facets form the boundaries in the propagation direction. The radial V_{il} boundary is defined in analogy to the Gaussian beam as the point where the intensity of the local maxima equals e^{-2} times the axial intensity, which is indicated by the dashed lines in Figure 4.2. The highest energy density region of the dual-waveguide trap's V_{il}, indicated by green and warmer colours in Figure 4.2 are found in a cylindrical volume between the facets. The remaining regions of the dual-waveguide trap's V_{il}, form a bulge on the middle of this volume, which increases with channel width. We will approximate the dual-waveguide trap's V_{il}, with some arbitrariness, as a cylinder with a radius of 1.5 μm spanned between the waveguide facets indicated in Figure 4.3b by the red hatching.

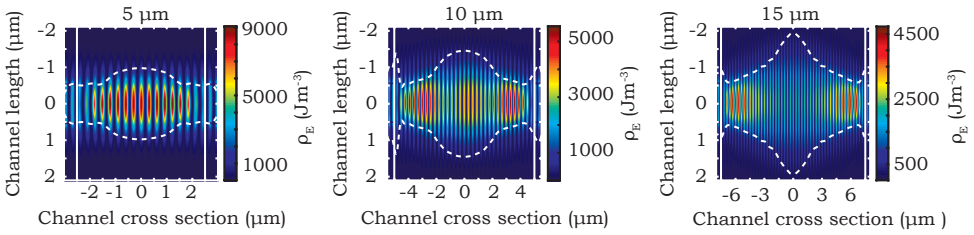

Figure 4.2: Simulated dual-waveguide trap illumination volumes. From left to right the 5, 10 and 15 µm dual-waveguide trap. (colormap) Energy density (ρ_E). (dashed lines) The radial V_{il} boundary. (solid vertical white lines) The position of the channel wall. Data courtesy of Gyllion Loozen

4

THE RAMAN GENERATING VOLUME

The Raman generating volume (V_{Rg}) is the volume in which Raman signal is generated, indicated in Figure 4.3 in orange. The V_{Rg} is that portion of the V_{il} that is occupied by a Raman active substance. Generally, the trapped particle represents the only Raman active substance for both modes. Consequently, the V_{Rg} is equal to the volume of the particle within the V_{il}. For the LTRS mode of operation this means that the V_{Rg} is always centred on the objective's optical axis. However, the dual-waveguide trap potentially generates multiple stable trapping sites, see Chapter 3 Section 3.4. Consequently, the V_{Rg} has several possible positions, which is illustrated in Figure 4.3b.

THE ACQUISITION VOLUME

The acquisition volume (V_{aq}) is the volume from which Raman signal can be collected. The numerical aperture (NA) of the objective and the size of the confocal pinhole determine this volume for both modes, as indicated by the green hatching in Figure 4.3. The NA determines the field of view of the system usually indicated with the f-number ($f\#$), which is related to the NA by $f\# \approx n/2NA$. Here n is the lowest refractive index in the path of the V_{aq}, in this case that of the immersion liquid. A larger field of view, i.e. lower $f\#$, results in a larger Vaq and more collected signal. Furthermore, the solid angle, defined by the NA, indicates which portion of the Raman signal scattered by a point is collected. In other words, a larger solid angle gives a higher collection efficiency for every point within the field of view.

The pinhole (see P in Figure 4.1) in the confocal filter rejects unwanted signal by restricting the field of view and the depth of focus. A smaller pinhole leads to a smaller acquisition volume by directly blocking part of the field of view. In the same way it reduces the contributions from other focus planes by partially blocking their out of focus image [86], resulting in a more selective signal acquisition.

The optimal signal acquisition is achieved by using the highest possible NA and a confocal pinhole size matching the size of the trapped particle while taking into account the optical magnification between the particle and the pinhole.

The strength of the acquired Raman signal is now proportional to the overlap between V_{Rg} and V_{aq}. The overlap between these volumes is constant for the LTRS, since both are determined by the objective. For the dual-waveguide trap, however, the overlap can become time dependent if the particle hops from one trapping site to the next (see

Figure 4.3b) and the particle is approximately equal in volume to V_{aq}. This means that the acquired Raman signal strength can only be reliably determined from a stable particle, a particle that remains trapped at a single site.

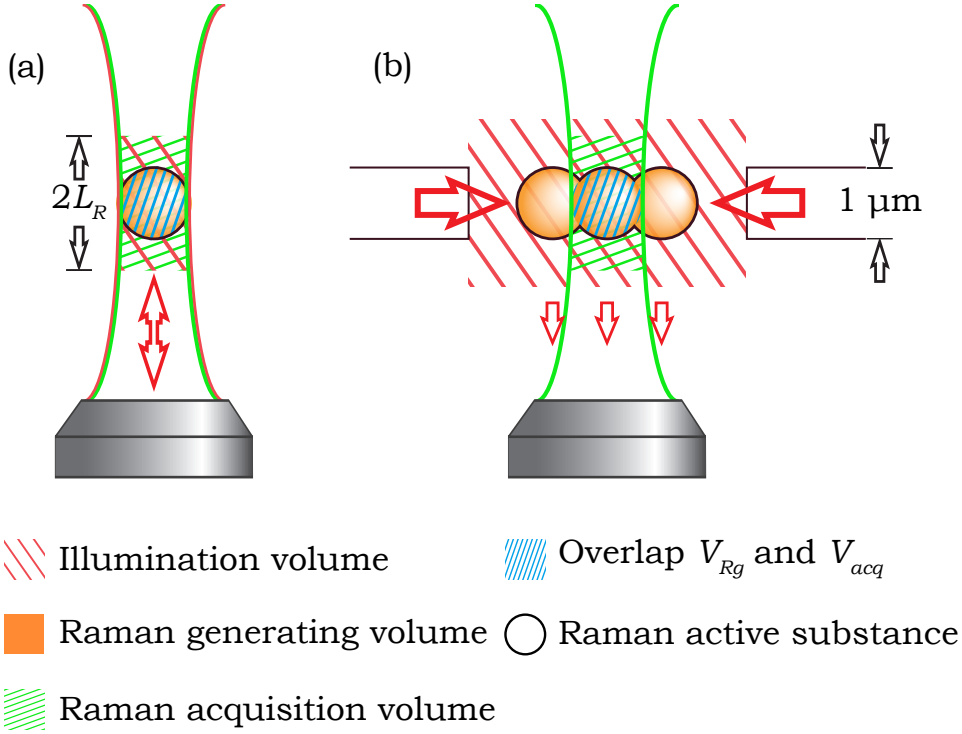

Figure 4.3: Relevant volumes for Raman spectroscopy. (a) LTRS. (b) Dual-waveguide trap. Illumination volume: the region with sufficient intensity to generate Raman signal. Raman generating volume: the portion of the V_{il} occupied with Raman active substance. Acquisition volume: the volume from which Raman signal can be acquired.

To compare the acquired Raman signal strength between the modes, dissolved ascorbic acid is used in Subsection 4.3.2 to circumvent the issues associated with a potentially unstable overlap. This, however, changes the shape of the V_{Rg} for both modes, since the entire V_{il} is now Raman active. The optimal V_{aq}, determined by the pinhole size, will be different for the two V_{Rg}. To provide an unbiased comparison this geometric difference needs to be accounted for.

To calculate the relative Raman acquisition efficiency of the two modes we first need an estimate of the Raman acquisition of the individual modes. Since any Raman signal generated outside of V_{aq} will not be acquired, we approximate the Raman acquisition efficiency (R_{acq}) to be proportional to the fraction of the V_{aq} that overlaps with V_{Rg}. This approximation assumes a homogeneous generation of the Raman signal throughout the V_{Rg}.

For the LTRS, V_{Rg} will be approximated by a cylinder with a radius (r_{Ray}) equal to that

of the focussed Gaussian beam one Rayleigh length from the focus and a length equal to two times the Rayleigh length (L_R), *i.e.*

$$R_{acq,LTRS} \propto \frac{V_{aq}}{2L_R \pi r_{Ray}^2}. \tag{4.1}$$

For the dual-waveguide trap, V_{Rg} equals the cylindrical volume spanning the channel width (W_{DW}) with the chosen radius of 1.5 µm (r_{DW}). This leads to R_{acq} for the dual-waveguide trap to be proportional to:

$$R_{acq,DW} \propto \frac{V_{aq}}{\pi r_{DW}^2 W_{DW}}. \tag{4.2}$$

Taking the relative R_{acq} as the ratio of the individual R_{acq} in waveguide mode versus LTRS mode and realizing that V_{aq} is the same for both modes, as it is determined by the chosen pinhole and objective, we find that $R_{acq,rel}$ is proportional to:

$$R_{acq,rel} \propto \frac{V_{Rg,DW}}{V_{Rg,LTRS}} = \frac{R_{DW}^2 W_{DW}}{r_{Ray}^2 2L_R}. \tag{4.3}$$

Equation 4.3 seems like a natural result when considering the discussion of the different volumes above. Although it provides us with a useful value for the relative Raman acquisition efficiency, it remains a crude approximation. To improve this approximation a more precise description of V_{Rg} and V_{aq} would be required. Especially for a discussion of the latter the reader is referred to the work of D. Leenman [59].

We find for the 5, 10 and 15 µm dual-waveguide trap, $R_{acq,rel}$ values of 23, 47 and 71 respectively. These values will be used in Subsection 4.3.2 to compare the LTRS with the dual-waveguide trap mode.

The parallel resp. perpendicular orientations of the cylinders modelling V_{il} and V_{aq} has an influence on the background signal acquired in the two modes. For the parallel orientations of the two cylinders, the objective collects any light backscattered by the particle or the traversed interfaces, including the Rayleigh scattered laser light. Consequently the LTRS mode requires strong filters (D2 and F in Figure 4.1) to remove this laser light from the Raman signal. For this orientation, a large part of the background signal is caused by the reflection and scattering of the fluidic-cell-interfaces (see Figure 4.4a). The trapped particle has relatively little influence on the background signal (see Figure 4.4b). As such, a background taken at the same position without a particle is still representative and can be subtracted from the Raman spectrum, after simple scaling, to yield a relative clean spectrum, as demonstrated in Chapter 2.

For the perpendicular orientations of the two cylinders, the counter-propagating beams are directed at the waveguides and only the weaker side scattered light is collected (see Figure 4.4c), reducing the need for filters. As such, the perpendicular orientation geometry is preferred over the parallel orientation geometry. The drawback of the perpendicular orientation geometry is that a trapped particle will strongly alter the way in which light is scattered towards the objective, changing the strength and spectral composition of the background signal. The compositional change is apparent from the fact that a scaled background does not match the spectral shape of the Raman spectrum's

background. The origin of the compositional change might be found in the hopping of the particle between trapping sites. If the diverging light emanating from the waveguides contains signal in the Raman window, causing a background signal variation over the width of the trap, a hopping particle can randomly mix the signal from different trapping sites. Consequently, the background signal obtained at a single point of an empty trap is not representative for the Raman spectrum's background of a trapped particle.

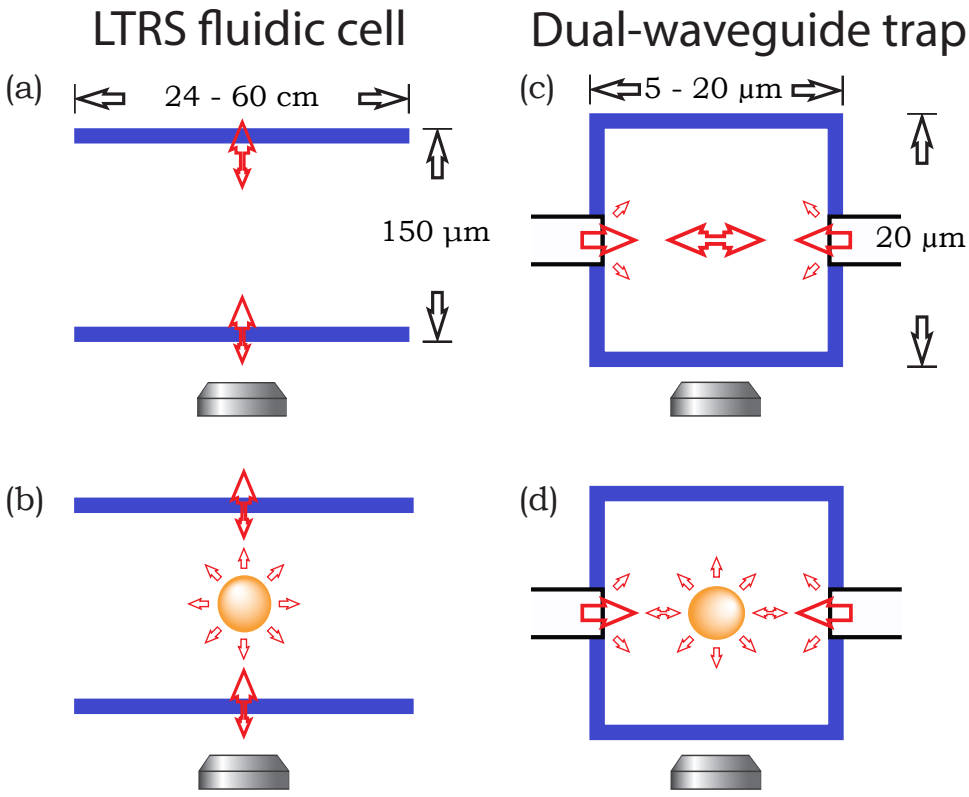

Figure 4.4: Comparison of the background collection for empty and full traps. (a) For the LTRS a portion of the laser light is reflected and scattered back towards the objective by the interfaces of the fluidic cell. (b) When a particle is trapped, only the amount of laser light directed towards the objective changes. (c) For the dual-waveguide trap, most laser light is directed from one waveguide to the other. Only a small part of the diverging light or light scattered from the side walls will reach the objective. (d) When a particle is trapped in the dual-waveguide trap the amount of laser light that reaches the objective strongly increases. Furthermore, the spectral composition of this light will be different from the light collected without a trapped particle (not shown).

The varying collection efficiency and background composition complicate the comparison of the different dual-waveguide traps. However, using dissolved ascorbic acid, the selected potential trapping position can simply be positioned inside V_{aq}. In this way, the acquired Raman and background intensity can be compared between traps and trapping positions. In Subsection 4.3.2 , the centre trap positions of the four different

dual-waveguide traps will be compared with this method.

4.3.2. COMPARISON OF THE RAMAN GENERATING PROPERTIES OF THE 5, 10, 15 AND 20 μm DUAL-WAVEGUIDE TRAPS

To select the trap size most suited for Raman spectroscopy of bio-particles, the Raman generating properties of the traps need to be compared. However, the multiple stable trapping sites generated by the dual-waveguide trap allow the overlap between V_{Rg} and V_{aq} to vary, as explained in the previous section. Such variation, during the experiment, would hamper the comparison of the trap's Raman generation. To avoid this, an ascorbic acid solution is used to stably fill the V_{aq} with Raman active material; independent of the trap's trapping behaviour and the position of V_{aq}. The potential trap position under investigation can now be selected by moving V_{aq} to the desired position in the trap.

Ascorbic acid, commonly known as vitamin C, was chosen because of its high solubility in water (0.333 kg/L), which is desirable because it maximizes the strength of the Raman signal. Its most prominent peaks are situated at 1129 and 1668 cm^{-1} [65]. These are well above 850 cm^{-1}, a threshold below which the background (see Figure 4.5) can potentially obscure the peaks. Additionally, the ascorbic acid spectrum contains a large variety of peak intensities. These properties make an ascorbic acid solution an ideal test solution.

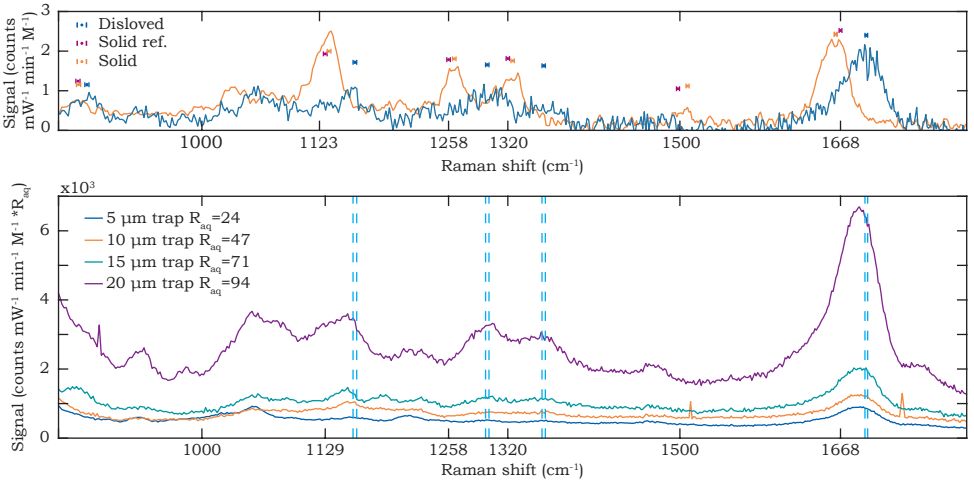

Figure 4.5: Ascorbic acid spectra. (Top) LTRS spectra. (orange) Solid ascorbic acid. (blue) Saturated ascorbic acid solution. (black markers) Literature peak positions. (orange markers) Solid ascorbic acid peak positions. (blue markers) Saturated ascorbic acid solution peak positions. Bars on the markers indicate the local spectrometer resolution. The peak positions (in cm^{-1}) are [Lit; solid; solution], [870.3; 871.0; 879.7], [1129; 1133; 1160], [1258; 1264, 1298], [1320; 1325; 1357], [1498; 1508; -], [1668; 1663; 1695]. (Bottom) Dual-waveguide trap spectra of a saturated ascorbic acid solution. (pairs of dashed lines) LTRS ascorbic acid peaks. The spacing between the lines indicate the local spectrometer resolution.

Reference spectra comparable to the spectrum obtained with the dual-waveguide traps were taken from solid and dissolved ascorbic acid with the LTRS. Both spectra in Figure 4.5a were acquired with P_{trap}= 18 mW, and an acquisition time of 1 min. A smoothed background, obtained by 3 point averaging, was subtracted from both recorded spectra. Six clear peaks can be identified in the solid ascorbic acid LTRS spectrum. When comparing their position to their literature values [65] a difference on the order of the spectrometer's resolution, indicated by the bars, is observed. We attribute this to an acceptable calibration difference. The compliance of this spectrum with the literature values is seen as validation of the new setup.

The LTRS spectrum of a saturated ascorbic acid solution, also presented in Figure 4.5a, contains five clear peaks. These peaks are shifted with respect to the solid ascorbic acid peaks, which is most noticeable for the peaks at 1129 and 1668 cm^{-1}. We attribute this shift to the difference in surrounding between the ascorbic acid molecule in a crystal lattice and the molecule being dissolved in demi water, a known effect in Raman spectroscopy.

Figure 4.5b presents the dissolved ascorbic acid spectra obtained with the four traps, all displaying four recognizable features, ranging from clear peaks for the 20 µm and 15 µm traps to weak features for the 10 µm and 5 µm traps. The spectra acquired with the 5, 10 and 15 µm traps were acquired with P_{trap}= 5.12 mW in 1 min. The spectrum acquired with the 20 µm trap was acquired with P_{trap}= 4.92 mW in 1 min. Striking in these spectra is a non-zero baseline and a downward slope. The latter is attributed to the slowly declining background signal, which we will treat extensively below. Comparing the peak positions in these spectra with the ones in the LTRS spectrum of dissolved ascorbic acid, (see Figure 4.5a) we find that they reproduce the shifted peaks, indicated by the dashed line-sets that we reported before. This confirms the correct functioning of both the dual-waveguide traps and the LTRS system.

When comparing the intensities between the two operational modes of the setup, we do not only need to normalize the graphs but also correct for differences in $R_{aqc,rel}$ as explained in Section 4.3.1. The solid ascorbic acid spectra has further been corrected for a difference in pinhole size, by multiplying by the ratio of the pinhole apertures. Having corrected the intensities for excitation power and $R_{aqc,rel}$ we find, comparing the peak heights at 1695 cm^{-1} in Figure 4.5 for the LTRS and the 5, 10 and 15 µm dual-waveguide traps, that between 430 and 1017 times as many counts mW^{-1} min^{-1} M^{-1} are acquired for the dual-waveguide trap as for the LTRS. This difference should, however, not be interpreted as an improved performance of the dual-waveguide trap over the LTRS, as it merely reflects the size of the illumination volume. As such Figure 4.5 indicates that the dual-waveguide traps have an advantage over the LTRS when addressing larger particles.

To compare the different dual-waveguide traps, eight repeated one-minute spectra are acquired for each dual-waveguide trap. For each measurement the acquisition volume is placed in the centre of the fluidic channel between the waveguides at the height of the waveguide facets. To average out any positioning errors, the acquisition volume is repositioned in-between measurements. Due to a malfunctioning piezo stage, which controls the position of the dual-waveguide trap with respect to the objective, the manual stage was used to perform the alignment for these experiments. This stage is normally only used for an initial coarse alignment due to its lower resolution and significant

hysteresis. Because of the hysteresis, the channel walls were used as positioning reference. The estimated positioning accuracy of this method is 10 % of the channel width.

Comparing the ascorbic acid spectra as produced by the different dual-waveguide traps; we find that the background signals seem to fall roughly into 2 groups. This is most clearly seen in the region between 400 and 550 cm^{-1} as shown in Figure 4.6. The spectra of one group, composed of the 5 and 15 µm traps, have three main peaks centred on 420, 458 and 491 cm^{-1}. The spectra of the other group, composed of the 10 and 20 µm traps, have two peaks centred on 438 and 481 cm^{-1}. These differences between the traps are a further indication that the chip at least influences the background spectrum, since this is the only component of the setup that changes when switching traps. The background spectrum will be analysed in Subsection 4.3.3.

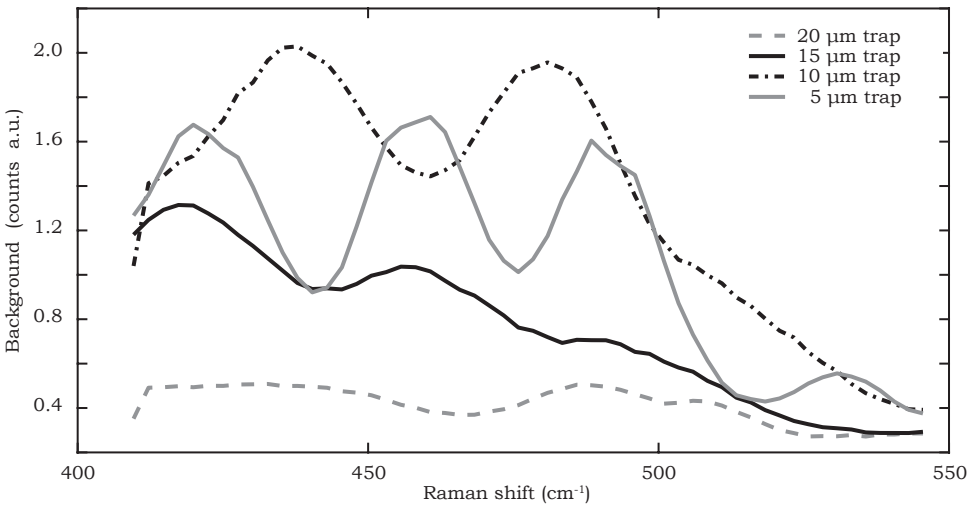

Figure 4.6: Background between 400 and 550 cm^{-1}. Each background is the average of eight spectra normalized to the intensities of the 1668 cm^{-1} peak.

To see which trap is least affected by the background we investigate the signal-to-background ratio. The signal strength was defined as the intensity of the ascorbic acid peak located at 1687.6 cm^{-1} since this strong peak is least affected by the decaying background. The background strength was subsequently taken as the average background between 409.6 and 545.5 cm^{-1}, as this region has negligible ascorbic acid signal (see Figure 4.6).

Figure 4.7 shows the signal-to-background ratio as a function of the trap size. We first observe a significant spread in the signal-to-background ratios for each trap, which increases with increasing trap size. Furthermore, we notice an increase in the average signal-to-background ratio with increasing trap size, denoted in Figure 4.7 by the blue line.

The upward trend observed in Figure 4.7 can be explained by realizing that the facets are further away from the field of view for the larger traps then for the smaller ones. Hence less background signal is collected for the larger traps. Since the trapped particle

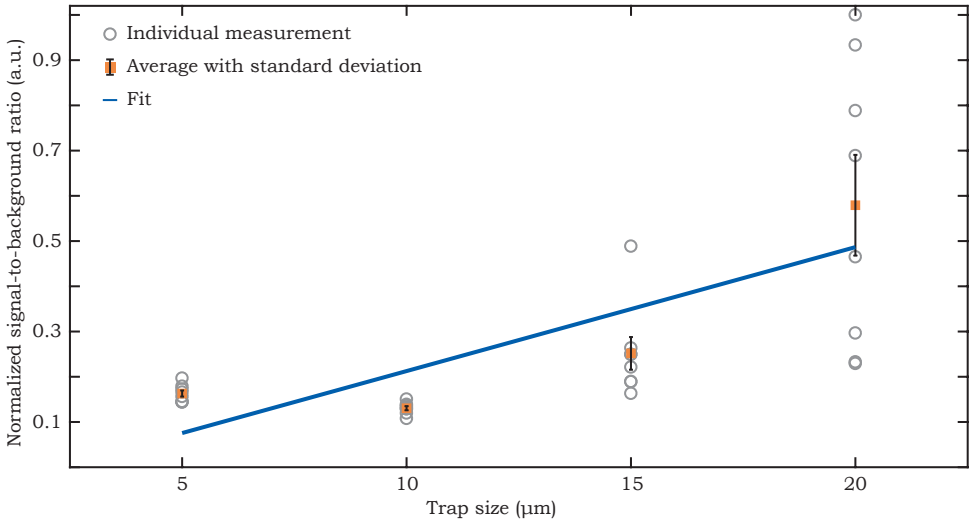

Figure 4.7: Signal-to-background ratio versus trap size. Per trap size eight measurements have been performed. The signal-to-background ratio of the different traps shows an increasing trend with trap size. This plot has been normalized to the highest signal-to-background ratio.

is kept in the field of view, the Raman signal is only affected by the laser intensity, which also affects the background.

Figure 4.8 provides an explanation for the increasing spread in the measurements as a function of the dual-waveguide trap-width in Figure 4.7. From Figure 4.8, we now find that the energy density in the 5 µm trap changes only 1.5 % upon a positioning error of 10% with respect to a perfectly centred measurement. For the 10 and 15 µm traps, this increases to 3.8% and 5.9% respectively. From this it is concluded that the increase in measurement error with increasing trap size is due to an increase in the manual positioning error between the objective and the dual-waveguide trap.

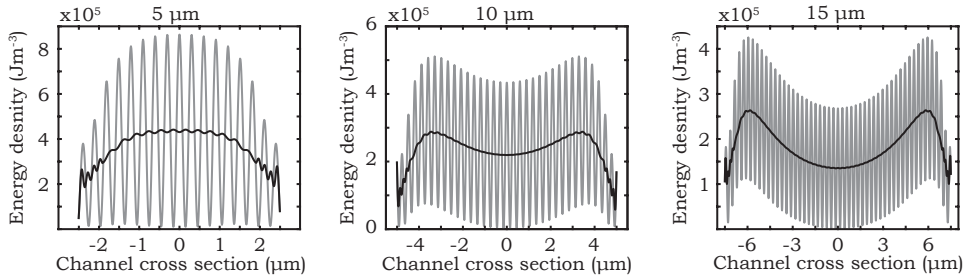

Figure 4.8: Summed energy density in the 5, 10 and 15 µm dual-waveguide traps. (grey lines) Summation of the energy density from Figure 4.2 over the 1.2 µm confocal filter diameter in the direction of the fluidic channel. (black lines) Summed energy density treated with a moving average (width 1.2 µm) along the waveguide axes. Data courtesy of Gyllion Loozen.

Based on Figure 4.7 the 20 µm dual-waveguide trap would be the most logical dual-waveguide trap to use for trapping Raman experiments since it provides the highest signal-to-background ratio, however, the uncertainty in these measurements is large. Additionally, the trapping potentials of the larger traps are shallower than those of the smaller ones. For instance the trapping potentials for the 15 µm dual-waveguide trap are U_x -2.9*10^3 $Jm^{-1}W^{-1}$ and U_z -1.7*10^3 $Jm^{-3}W^{-1}$ compared to U_x -9.5*103 $Jm^{-3}W^{-1}$ and U_z -2.3*10^3 $Jm^{-3}W^{-1}$ for the 5 µm trap. Combined with the larger area in which a trapped particle can "hop around" this means that the chance of a particle moving in and out of the acquisition volume during the integration time becomes larger for the larger traps. Since this hopping between trapping sites would somewhat reduce the signal collection from a biological particle, which is already expected to be low, the 10 and 5 µm traps were nevertheless chosen as bases for the following experiments.

4.3.3. ANALYSIS OF THE BACKGROUND SIGNAL

After the measurements presented in this chapter had been performed, a signal (see Figure 4.9) was found in the light coming from the fibre (see Fi in Figure 4.1). This spectrum, to be referred to as the input spectrum, was measured by placing the fibre at the position of the confocal filter. The input spectrum is most likely not present in the spectra taken with the LTRS because in this mode the laser is reflected on the Raman filter (D2 in Figure 4.1) which transmits any signal within the Raman window, effectively attenuating the input spectrum.

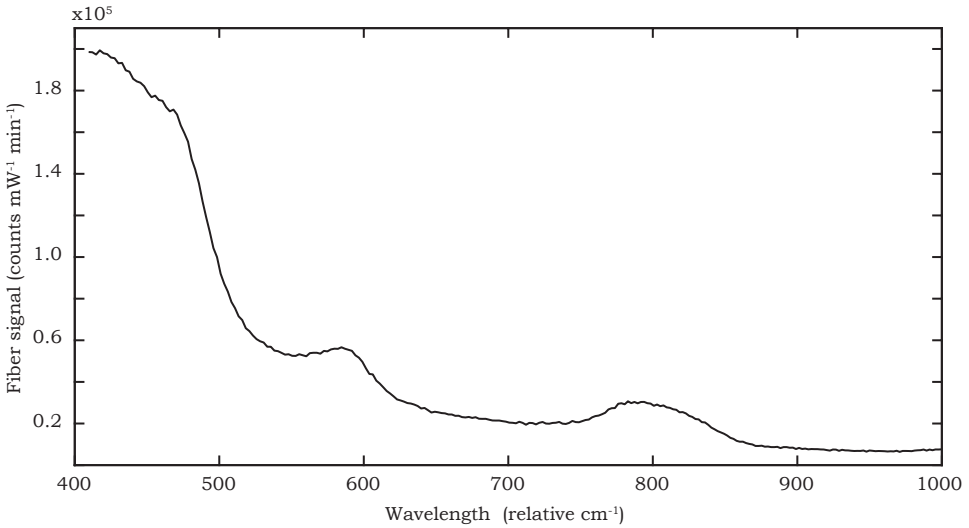

Figure 4.9: Input spectrum. This spectrum was obtained by placing fibre Fi in the pinhole holder P in Figure 4.1. A notable difference between this spectrum and the background observed in Figure 4.6 is the absence of the relative sharp peaks and the slow decrease at higher shifts. The latter is not shown in Figure 4.6. This decrease is most likely absent in the input spectrum because dichroic mirror D2 is bypassed during its collection.

A notable difference between the input spectrum (Figure 4.9) and the background in the spectra acquired with the dual-waveguide traps (Figure 4.6) is the absence of the

relative sharp peaks of the latter in the input spectrum. Examining the spacing between these peaks between 410 and 900 cm^{-1} we find a spacing of – on average – 2.9, 3.2, 3.1 and 3.9 nm for the 5, 10, 15 and 20 µm traps respectively. This relatively regularly spaced intensity variation leads us to suspect that the transmission characteristic of a cavity is superimposed on the background signal.

To find the size of the suspected cavity, the background spectrum is analysed with an OCT based approach resulting in the length of possible cavities. The light intensity reaching the spectrometer can be seen as composed of three terms: the directly transmitted light intensity, the indirectly transmitted light intensity after internal reflections, we will refer to the sum of these as the DC-component, and the intensity of the interference of the direct and indirect beams which we will denote as $I(k)$. Starting with Equation 3 from Trull et al. [87] and following the step presented by Kalkman et al. [88] we can write:

$$a(z) \propto F_k\{I(k)\}(z). \tag{4.4}$$

Equation 4.4 states that the transmission as a function of optical path length difference ($a(z)$) is proportional to the Fourier transform ($F_k\{I(k)\}(z)$) of the interference signal, expressed as a function of the wave vector ($I(k)$). Since we are only interested in the length of any cavities rather than in their absolute transmission, knowing the proportionality is sufficient here. With this an intensity increase in $a(z)$ can be interpreted as an optical path length difference (Δ_{opl}) travelled by the indirectly transmitted light. It is assumed that light transmitted after four reflections will be too weak to be detected. Realizing that transmission requires an even number of reflections, each peak position represents twice the length of the cavity from which it originates.

Figure 4.10 shows the results of this operation applied to the spectral interval represented in Figure 4.6. First the DC-component needs to be subtracted (Figure 4.10 left column). The DC-component will only differ in a phase factor from the input spectrum; consequently a scaled version of this spectrum is subtracted. The resulting spectrum represents the interference term $I(k)$.

Taking the Fourier transform of the interference term we get the Δ_{opl} dependent transmission $a(z)$ (Figure 4.10 right column). Here we find for all four traps a large initial peak centred at 0 µm. This peak is a remnant of the DC-component and is referred to as the ballistic peak. The subsequent peaks provide the Δ_{opl} at which transmission occurs. For the 5 µm trap the transmission displays peaks at 40 µm and 76 µm. For the 10 µm trap we find one broad peak at 57 µm, which could also be an unresolved double peak. The reflectivity of the 15 µm trap first shows one peak at 30 µm and then reproduces the peaks of the 5 µm trap at 46 µm and 71 µm with a deviation slightly larger than the resolution in the z-domain of 5.1 µm. Lastly, for the 20 µm trap, peaks are found at 30 µm and 46 µm, exactly reproducing two of the three peaks found for the 15 µm trap.

By taking half of the z values of the peaks we find cavity lengths of: for the 5 µm trap, 20 and 38 µm; for the 10 µm trap 28.5 µm; for the 15 µm trap 15, 23 and 35.5 µm and for the 20 µm trap 15 and 23 µm. Comparing the values of the cavity lengths to the design of the dual-waveguide trap, a structure in the size range of 15 µm to 38 µm has to be found. The only defined structure of this approximate size is the waveguide splitter. Its width is wider than the conventional waveguide and the light confinement is weaker near the end of the splitter, resulting in appreciable light leakage and possible back reflection.

Other structures that could cause single reflections would be the entry and trapping waveguide facets or waveguide-curvature changes which can cause reflections due to a mode mismatch [45]. Confirming which structure is the source of the found interference will require further investigation.

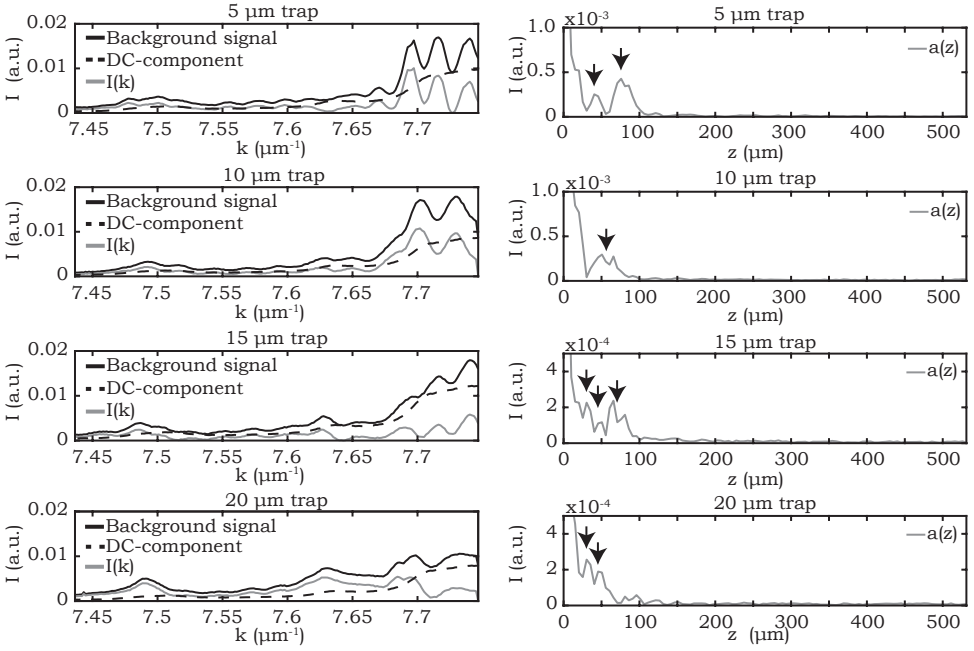

Figure 4.10: Depth dependent reflectivity analysis. (Left column) The background spectrum, DC-component and $I(k)$ between 410 and 903 cm^{-1} for the 5, 10, 15 and 20 µm traps. (Right column) Reflectivity as function of depth for the 5, 10, 15 and 20 µm traps. (black circle) Reflection peak.

4.4. DISCUSSION AND CONCLUSIONS

In this chapter improvements to the setup used in Chapter 3 and a comparison of the LTRS and the dual-waveguide traps have been presented. The discussion and conclusions of the aforementioned results are presented here.

The optical setup was changed such that each of the side arms can compensate for an orientation error of the coupling mirrors in the main optical path. Furthermore, a beam expander inserted directly behind the objective ensures that the beam profile is preserved without clipping through all arms of the optical system. It was found that the setup used in this chapter is less sensitive to miss-alignment and produces better image quality than the configuration presented in previous chapters.

It was found that the dual-waveguide trap produces a stronger Raman signal than the LTRS. This difference is theoretically explained by the larger illumination volume (V_{il}) of the dual-waveguide trap. This larger V_{il} of the dual-waveguide trap is an advantage when working with larger particles such as yeast cells.

Raman experiments with dissolved ascorbic acid showed that the 5, 10, 15 and 20 μm dual-waveguide traps all produced recognizable Raman spectra. It was shown that the background differs in spectral composition per trap and decreases in intensity with trap width. The periodic structure of the background suggests the presence of a cavity type structure within the device, which imposes structure upon the input spectrum. The cavity type structure has yet to be identified. The trapping forces also decrease with trap width. Therefore, the smaller traps are preferred for further experiments, despite the higher background in the acquired spectra.

5

THE FEASIBILITY OF *Bacillus subtilis* SPORE IDENTIFICATION WITH THE DUAL-WAVEGUIDE TRAP

5.1. INTRODUCTION

The fast identification of micro-organisms, such as yeasts and bacteria, is of utmost importance in a large range of applications. Massive parallel single cell Raman spectroscopy is a fast alternative for traditional techniques such as streak plating and PCR. A step in this direction is the dual-waveguide trap, which is an on-chip trapping and Raman device, in our case monolithically fabricated in TripleX waveguide technology [43]. Trapping and Raman generation have been demonstrated with the dual-waveguide trap for polystyrene beads [85]. However, acquiring Raman spectra from biological particles is significantly harder.

Identifying micro-organisms from their Raman spectrum by means of supervised pattern recognition and machine learning requires the creation of a training set containing a large number of spectra (see Chapter 2). Instead, we here study the feasibility of identification by comparing the quality of the obtained spectra with two benchmark values from literature for which identification was proven.

In Subsection 5.2.1 the *Bacillus subtilis* spores are introduced, after which the measuring procedure and spectrum processing required to arrive at the spore spectrum are presented. Before spore peaks can be identified, further spectrum analysis is required, as discussed in Subsection 5.2.3, to separate the spore peaks from the periodic background. The spectra obtained with the 10 µm and 5 µm trap respectively are presented in Subsection 5.3.1 and Subsection 5.3.2

The discussion and conclusions are presented in Section 5.4.3, starting with a short evaluation of the setup in Subsection 5.4.1. Finally, in Subsection 5.4.2, the quality of the obtained spectra is compared to the benchmarks and the feasibility of dual-waveguide based *Bacillus subtilis* spore identification is assessed.

5.2. MATERIALS AND METHODS

This section consists of three subsections. In Subsection 5.2.1 the bacterial spores that will be used for the trapping and Raman experiments in the following sections are presented. Subsequently in Subsection 5.2.2, a brief overview is provided of the used setup and devices, which have already been treated in Chapter 4. Finally the methods used to acquiring and analyse the obtained Raman spectra are detailed in Subsection 5.2.3.

5.2.1. *Bacillus subtilis* SPORES

Bacillus subtilis spores are used as bio-particles because of several reasons. Their diameter is well defined at about 1 µm [26]. Their density is higher than that of bacteria, leading to a stronger Raman signal per unit volume. Their higher average refractive index [26] makes them easier to trap. Furthermore, the spores were readily available and can be stored for a long time, negating the need for fresh cultures.

Figure 5.1 shows the Raman spectrum of *B. subtilis*, which is dominated by the spectrum of dipicolinic acid chelated with Ca^{2+}. This makes the spectrum much simpler than those of non-spore organisms. Consequently, the spectrum can be visually recognized as originating from a species in spore form, from a distinct set of features. Candidate features are e.g. the combined presence of the 1004 and 1017 cm^{-1} peaks or the strong peaks at 1395 and 1448 cm^{-1}.

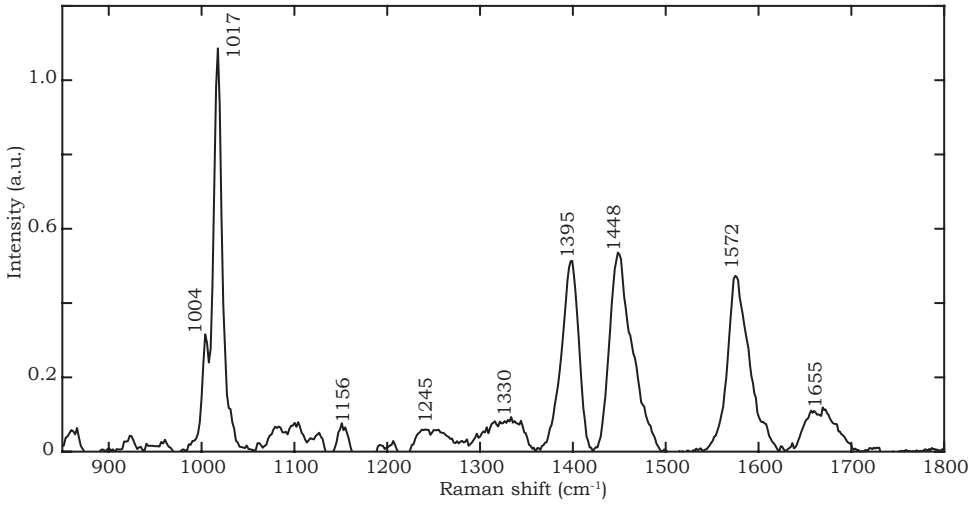

Figure 5.1: Literature spectrum of *B. subtilis* obtained as average of 100 individual spore spectra. Reproduced from [89] with permission from dr. Li Yong-qing.

5.2.2. DEVICES AND SETUP

The setup used in this chapter (see Figure 5.2) uses reflective optics (M D2, D1, and BS) to guide the main beam path, indicated in blue, from the chip holder (CH) to the camera (C). Using lenses L1 and L2, placed within the infinity space of the objective, the

acquired image signal beam and Raman signal beam are respectively contracted and re-collimated. The side arms are the LTRS arm indicated in red, the Raman arm indicated in purple and the illumination arm indicated in green. The beams of these arms are coupled to the main beam path by traversing D1, D2 and BS respectively. A halogen lamp is used in to provide Köhler illumination to the region of interest in the object plane. The chip holder consists of a chip shaped cavity in an aluminium drum. The chip holder is mounted on both a manual and a piezo stage to allow positioning relative to the objective and, in this chapter, holds the 10 or 5 µm dual-waveguide trap chip. These chips are named for the separation between their waveguide facets in the fluidic channel. In this chapter the setup will only be used in dual-waveguide trap mode which means that the fibre (Fi) is directly coupled to the dual-waveguide trap chip.

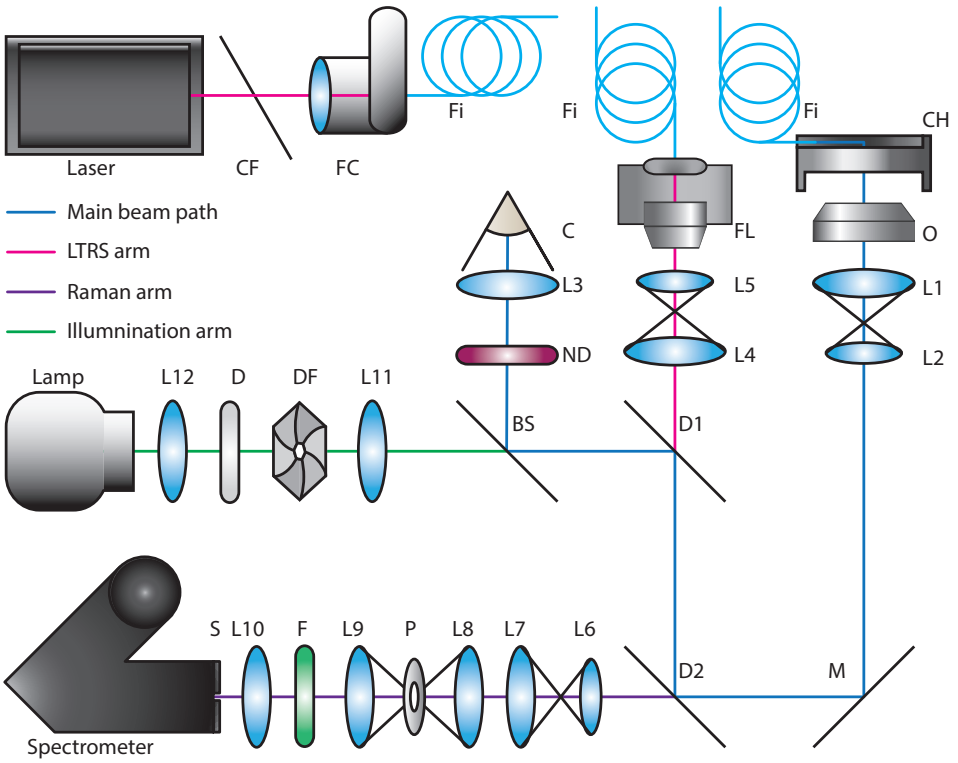

Figure 5.2: Experimental setup used in this chapter. (blue) The main beam path. (red) The LTRS arm. (purple) The Raman arm. (green) The illumination arm. Components: L1-12 - lenses, CF - clean-up filter, FC – Newport 9131-M fibre coupler, Fi - Thorlabs PM-630-HP polarisation maintaining fibre, FL - fibre launcher, C - camera, ND - neutral density filters, Lamp - halogen lamp, D - diffuser plate, DF - diaphragm, BS - 50:50 beam splitter, D1, D2: dichroic mirror, M - silver mirror, O - Olympus UPLSAPO 60XW or LUMPLFLN 40XW objective, CH - chip holder, F - filter, P - pinhole ø=100 µm, S - spectrometer entrance slit, spectrometer Acton LS 785. Lens sets L1/L2, L4/L5 and L6/L7 form beam expanders. L9, P and L8 form a confocal filter.

5.2.3. ACQUIRING RAMAN SPECTRA AND METHOD OF SPECTRUM ANALYSIS

In contrast to Chapter 3, the dual-waveguide trap channel was filled using a µl-pipet, with approximately 1 µl of spore Milli-Q suspension[1] . After placing the chip in the holder, a fibre (see Fi in Figure 5.2) was used to couple light into the input waveguide of the dual-waveguide trap. Around 120 mW of laser power was used. Trapping events were generated by allowing spores to be carried to the trapping region by the spontaneous flow in the channel caused by *e.g.* remaining capillary effects. Trapping events were detected by monitoring the changes in number of bright spots from which light in the trapping region is scattered into the camera image (see C in Figure 5.2). This allows a crude determination of the number of trapped spores. Using this method, the obtained spectra were divided into few spores spectra (#spores ≤ 3) and many spores spectra (#spores ≥ 4). A few spores spectrum is more difficult to measure than a many spores spectrum, because the Raman generating volume is smaller for few spores. Additionally, a few spores measurement ends when too many spores are trapped or lost whereas a many spores measurement only ends when too many are lost. For few spores spectra, this limits the chance of attaining long acquisition times and thus stronger signals.

Starting from the trapping event, a sequence of 60 frames with an integration time of 10 seconds per frame was acquired. A subset of this sequence, containing spore-signal, was then averaged to obtain the raw spore spectrum. To obtain a raw background spectrum a set of frames, not necessarily sequentially acquired, without spore-signal was averaged. The raw background is assumed to be representative of the empty trap.

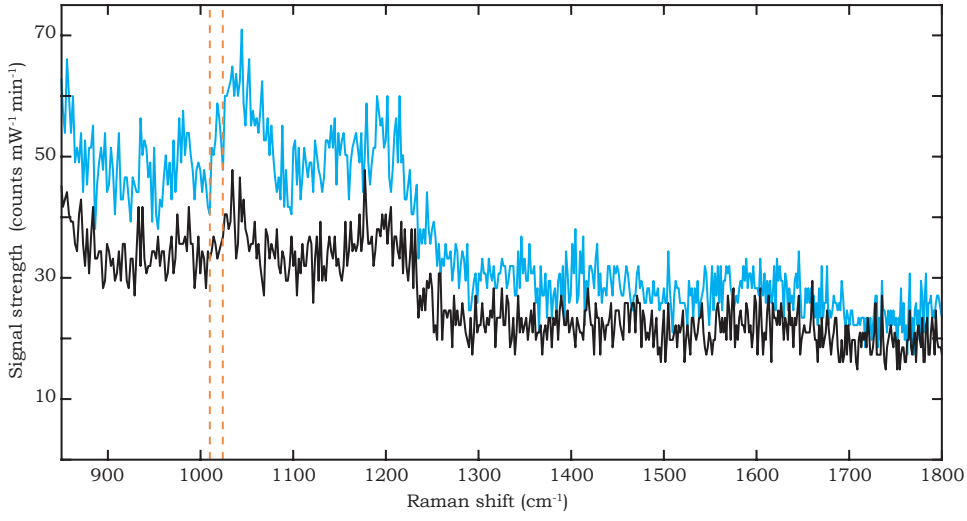

Figure 5.3: Examples of single frame spectra. (blue line) A single frame containing spore signal. (black line) A single frame without spore signal. The dashed lines indicate the range used to determine the presence of spore signal.

[1] The *Bacillus subtilis* spore (NCCB 70064) suspension was kindly provided by the Media and Sterilization Support staff of the Department of Biotechnology of the TU Delft.

Figure 5.3 shows one frame with and one without spore-signal. The criterion for presence of spore-signal is a peak, of sufficient width and intensity, in a range around the expected 1017 cm^{-1} spore (see Figure 5.3). If the range showed no peak, the frame was assumed to have no spore-signal. The spore-signal presence was determined during post processing. Although the frames in Figure 5.3 are very noisy, further analysis of the raw spectra will show that this selection criterion is effective. The frames in Figure 5.3 also show the slow decline and two broad structures of the periodic background, centred at 1050 and 1200 cm^{-1}.

To avoid "cherry picking", only continuous frame sequences were averaged to form the raw spore spectra. Frames containing a cosmic peak were rejected from the subset. In such cases, the sequence was still considered to be continuous. This method is labour intensive and gives more readout noise than a single 600 second acquisition. However, it has the benefit that the acquisition–time window can be chosen to coincide with the spore presence in post-processing with a time resolution of 10 seconds. This means that spore-signal is present during practically the entire acquisition time. In contrast, with a single 600 second acquisition only part of the acquisition time may contribute to the spore-signal, whereas the entire acquisition time contributes to the background, thus decreasing the signal-to-background ratio.

The raw spectra are further treated as regular spectra. The spore spectra (S_{spore}) shown in Subsections 5.3.1 and 5.3.2 are given by:

$$S_{spore} = (R_{spore} - \alpha S'_{in}) - \beta(R_{bg} - \gamma S'_{in}). \tag{5.1}$$

Here the two terms in brackets give the corrections of the raw spore and background spectra (R_{spore}, R_{bg}) with the input spectrum (see Figure 4.9). S'_{in} is the input spectrum in which the slow decrease in background, observed in the raw spectra in Figure 5.3, has been re-created with a linear offset. The scaling factors (α,β,γ) in Equation 5.1 are chosen such that the maximum amount of background signal is removed from the spectrum without causing excessive negative values.

The spore spectra presented in the following sections are divided into four groups based on trap size (10 or 5 µm) and number of spores (many or few).

The first step of the spectrum analysis is identification of the spectra as spore spectra, by assigning peaks in the spectra to reference peaks. A systematic coinciding of measured peaks with the reference leads to a positive identification. To assign a peak it needs to be discernible. Due to the periodic background (see Chapter 4), peaks have to be assigned based on the local maxima found in the spectrum after filtering with a flattened Gaussian [90] in the Fourier domain. A flat Gauss transfer function is used instead of an ideal (rectangular) low pass transfer function to minimize the introduction of ringing artefacts in the filtered spectra. The cut-off frequency of this filter is chosen per trap, so as to exclude all frequencies above the start of the frequency band of the periodic background.

In the spore spectra, discussed in detail in the following sections, the peak at 1017 cm^{-1} is most prominent due to the selection bias. The peaks at 1395 and 1448 cm^{-1} are present in all spectra. Furthermore, we find one or more of the peaks at 1330, 1572 or 1655 cm^{-1} in each spectrum. In all shown spectra at least three peaks are assigned,

identifying all as spore spectra. The assigned peaks are used to determine the figures of merit for each spectrum.

The quality of the spectra is assessed based on the following three figures of merit:
i) the number of assigned peaks, which quantifies the strength of the identification;
ii) the average prominence of the assigned peaks in the Fourier filtered spectrum, to which we will further refer as the average signal strength ($\overline{S}$), as it is a measure for peak signal strength;
iii) the average prominence-to-noise further referred to as the average signal-to-noise ratio ($\overline{SNR}$).

The prominence [91] is the height of a peak relative to the lowest local minimum between the peak and the nearest peak of higher intensity. The prominence in the Fourier filtered spectrum is a lower bound of the signal strength, since nearby peaks do not contribute to it. To determine the noise level a smoothed version of the spore spectrum, obtained by 3 point averaging, is subtracted from the spore spectrum. The noise level is now defined as the rms value of the remaining signal.

In addition to the peaks assigned according to the above procedure, each spectrum shows one or more features that can be manually assigned, which come in two types. The first type is only a shoulder on a stronger peak in the Fourier filtered spectrum, making it hard to assign position and signal strength. The second type is tentatively assigned based on the unfiltered spore spectrum, but is less reliable since it cannot be differentiated from the periodic background with certainty.

5.3. RESULTS

The results are presented according to the dual-waveguide trap from which they were obtained. In Subsection 5.3.1 the many and few spores spectra obtained with the 10 µm trap are presented. Those obtained with the 5 µm trap are presented in Subsection 5.3.2

5.3.1. RAMAN SPECTRA OF BACTERIAL SPORES OBTAINED WITH THE 10 μm TRAP

Using the method detailed in the previous section, 27 full sequences of 600 seconds length, were obtained with the 10 µm trap. From the subsets found, the two best suited for further processing are shown below as the spectra originating from either many or few spores. The signal strength of the spectra, expressed as counts $mW^{-1}min^{-1}$, is normalized to the power in the trap. This is calculated from the power coupled into the input waveguide of the chip, using the 4.1% coupling efficiency determined in Chapter 3

Figure 5.4a shows a many spores spectrum composed of twelve frames of ten seconds. The obtained signal is low, leading to low signal-to-noise ratios. In the Fourier filtered spectrum, peaks are found at 1401 and 1458 cm^{-1}. Figure 5.4c compares these peak positions to the reference peak positions at 1395 and 1448 cm^{-1}. Here a small shift on the order of the spectrometer resolutions is seen. As before (see Figure 4.5), this is attributed to a calibration difference. Further peaks are found at 1332, 1581 and 1653 cm^{-1}. In Figure 5.4c and 5.4d these peaks are shown with the associated reference peak positions at 1330, 1572 and 1655 cm^{-1}. The assignment of these five peaks identifies this spectrum as a spore spectrum.

The average signal strength of the five assigned peaks is 2.8 counts mW−1 min^{-1}, leading to an average SNR of 2.3. The maximum SNR of 4.2 is achieved for the measured peak at 1581 cm^{-1} (see Figure 5.4d). The assigned peak positions and figures of merit, along with other data are compiled for further comparison in Table 5.1 on page 81, as will be done for the other spectra in this and the following section.

In Figure 5.4a, three broad peaks are seen in the spore spectrum at 1044, 1106 and 1185 cm^{-1}. These peaks result from the periodic background. Because of their width they are carried into the Fourier filtered spectrum, obstructing the assignment of spore peaks. Figure 5.4c shows such a situation at 1273 cm^{-1}. Here a peak, that is associated with the reference peak at 1245 cm^{-1}, is reduced to a shoulder of the 1185 cm^{-1} background peak. As a shoulder it cannot be assigned.

Figure 5.4b shows two further peaks in the spore spectrum at 1004 and 1016 cm^{-1}. These peaks are associated with the 1004 and 1017 cm^{-1} reference peaks and are relatively well pronounced considering the SNR of this spectrum. However, neither peak is carried into the Fourier filtered spectrum due to their small width, low amplitude and proximity to the dominant background peak located at 1044 cm^{-1}. These peaks illustrate the strictness of the used assignment rule. Even the 1017 cm^{-1} selection biased peak would in this case not have qualified for assignment.

A few spores spectrum, obtained with the 10 µm trap is shown in Figure 5.5a. It is composed of a two frame sequence. In the Fourier filtered spectrum five spore peaks are found, as indicated by the magenta arrows in Figure 5.5a. In Figure 5.5c and 5.5d, these peaks are shown with the associated reference peak positions. Table 5.1 on page 81 gives

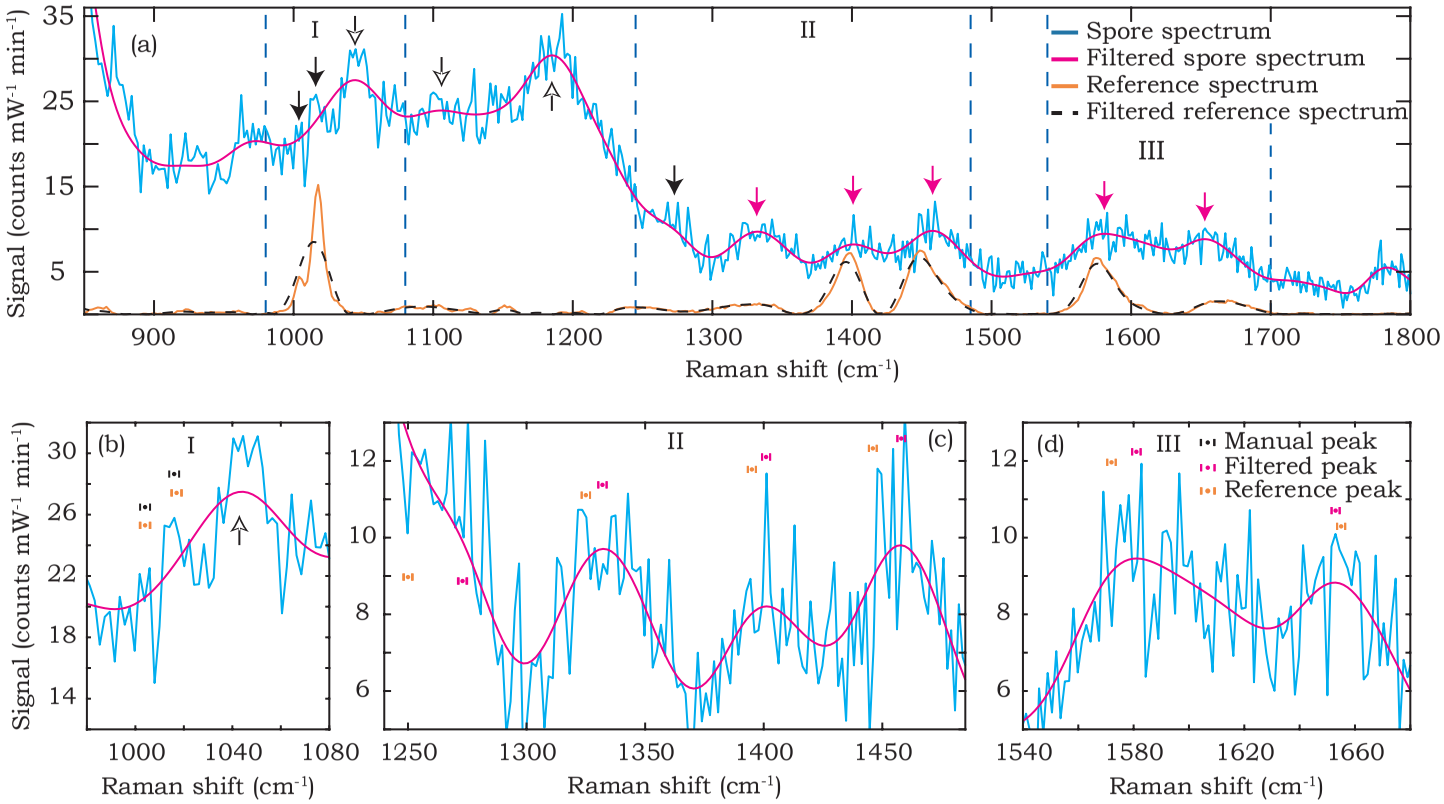

Figure 5.4: Many spores Raman spectrum from the 10 μm trap. (a) Full spectrum with five assigned peaks (magenta arrows), three manually assigned peaks (black arrows) and three background peaks (open arrows). (b) Close up, showing the peaks at 1004, 1016 and 1044 cm^{-1}. (c) Close up, showing the shoulder at 1273 cm^{-1} and the assigned peaks at 1332, 1401 and 1458 $^{-1}$. (d) Close up, showing the assigned peaks at 1581 and 1653 cm^{-1}. The bars in plots (b-d) give the local spectrometer resolution at the position of the manually assigned peaks, the assigned peaks and the reference peaks.

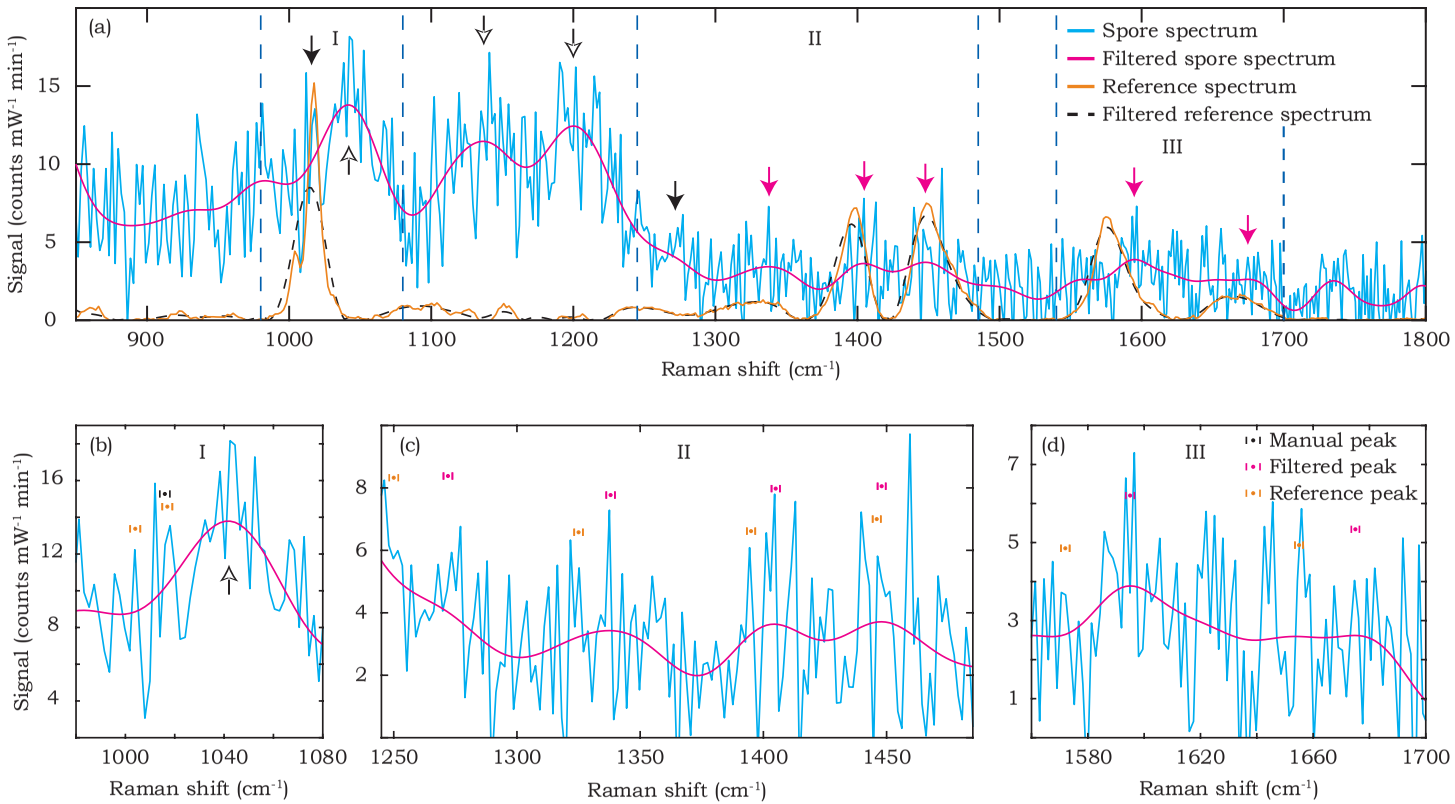

Figure 5.5: Figure 14 Few spores Raman spectrum from the 10 μm trap. (a) Full spectrum with five assigned peaks (magenta arrows), two manually assigned peaks (black arrows) and three background peaks (open arrows). (b) Close up, showing the peaks at 1016 and 1042 cm^{-1}. (c) Close up, showing the spore peaks at 1338, 1405 and 1448 cm^{-1}. (d) Close up, showing the assigned peaks at 1572 and 1655 cm^{-1}. The bars in plots (b-d) give the local spectrometer resolution at the position of the manually assigned peaks, the assigned peaks and the reference peaks.

the measured and reference peak positions.

The average signal strength of the 5 assigned peaks is 1.2 counts $mW^{-1}min^{-1}$ with an average SNR ratio of 0.6. This is less than for the many spores spectrum, as was expected. The maximum SNR of 1.3 is found for the measured peak at 1595 cm^{-1} as shown in Figure 5.5d.
Three background peaks are seen in this spectrum, at 1042, 1137 and 1200 cm^{-1}. The 1200 cm^{-1} peak again has a shoulder associated with the 1245 cm^{-1} reference peak (see Figure 5.5a). In Figure 5.5b the 1017 cm^{-1} reference peak is less clear than in the many spores spectrum.

5.3.2. RAMAN SPECTRA OF BACTERIAL SPORES OBTAINED WITH THE 5 μm TRAP

For the 5 µm trap 100 full sequences of 600 seconds were obtained. From the subsets found, the two best suited for further processing are shown below as the spectra originating from either many or few spores.

The many spores spectrum shown in Figure 5.6a was acquired in the 5 µm trap as a 9 frame sequence. In this spectrum three peaks are found in the Fourier filtered spectrum indicated by the magenta arrows. These peaks are shown with the associated reference peak position in Figure 5.6c. The exact peak positions and associated values are compiled in Table 5.1 on page 81. With the assignment of these three peaks, the spectrum is identified as a spore spectrum.
The average signal strength of the 3 assigned peaks is 4.4 counts $mW^{-1}min^{-1}$ and the average SNR is 2.3. The maximum SNR of 6.3 was obtained for the 1448 cm^{-1} peak. The very low 0.04 SNR of the 1395 cm^{-1} peak in this spectrum can be explained by its weak prominence relative to the strong peak at 1448 cm^{-1}.
This many spores spectrum has two rather than three strong background peaks, located at 1050 and 1217 cm^{-1}.
Figure 5.6b shows that the peak associated with the 1017 cm^{-1} reference peak is strong enough in this spore spectrum to dominate the background peak at 1050 cm^{-1}. In Figure 5.6d, two further peaks corresponding to the 1572 and 1655 cm^{-1} reference peaks can be seen in the spore spectrum. However, neither of these is strong enough to produce a local maximum in the Fourier filtered spectrum.

In Figure 5.7 the few spores spectrum for the 5 µm trap is shown, again obtained as a 9 frame sequence. Five spore peaks are observed in the Fourier filtered spectrum as indicated in Figure 5.7a. Their assignment in Figure 5.7c and 5.7d gives a positive identification for this spectrum.
The average signal strength of the 5 assigned peaks is 0.8 counts $mW^{-1}min^{-1}$ and the average SNR is 0.4. The maximum SNR of 1.5 is found for the peak at 1330 cm^{-1}. The lowest SNR of the four presented spore spectra is 0.03 and found for the 1572 and 1655 cm^{-1} peaks shown in Figure 5.7d. As explained before the SNR value does not reflect on the quality of the peak assignment.
Two strong background peaks are seen in Figure 5.7a at 1050 and 1217 cm^{-1}. As in Figure 5.6, the 1050 cm^{-1} peak is dominated by the 1017 cm^{-1} peak. In Figure 5.7b even a peak tentatively associated with the 1004 cm^{-1} reference peak can be seen.

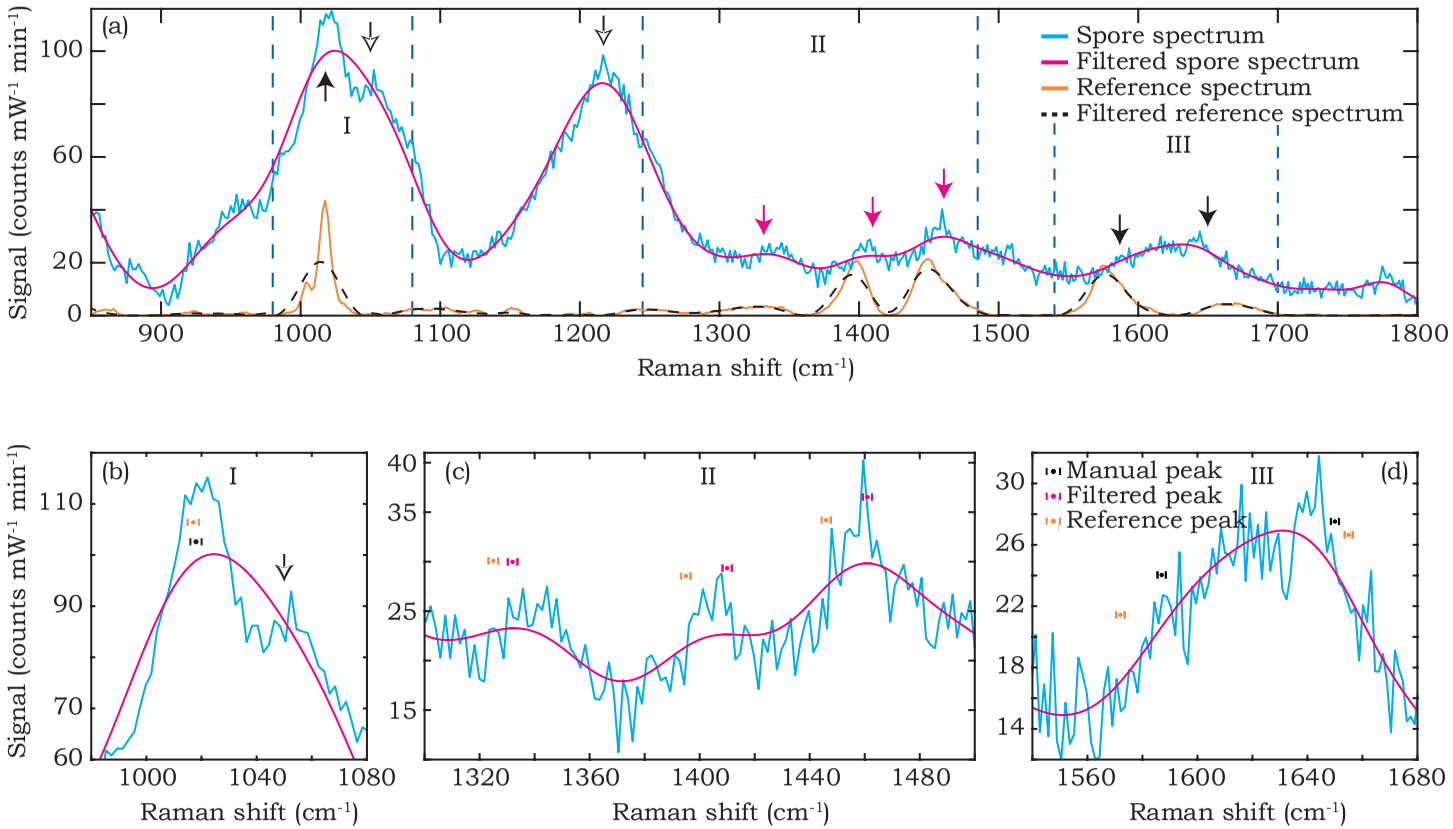

Figure 5.6: Figure 15 Many spores Raman spectrum from the 5 μm trap. (a) Full spectrum with three assigned peaks (magenta arrows), three manually assigned peaks (black arrows) and two background peaks (open arrows). (b) Close up, showing the peaks at 1018 and 1050 cm^{-1}. (c) Close up, showing the spore peaks at 1332, 1410 and 1461 cm^{-1}. (d) Close up, showing the peaks at 1587 and 1650 cm^{-1}. The bars in plots (b-d) give the local spectrometer resolution at the position of the manually assigned peaks, the assigned peaks and the reference peaks.

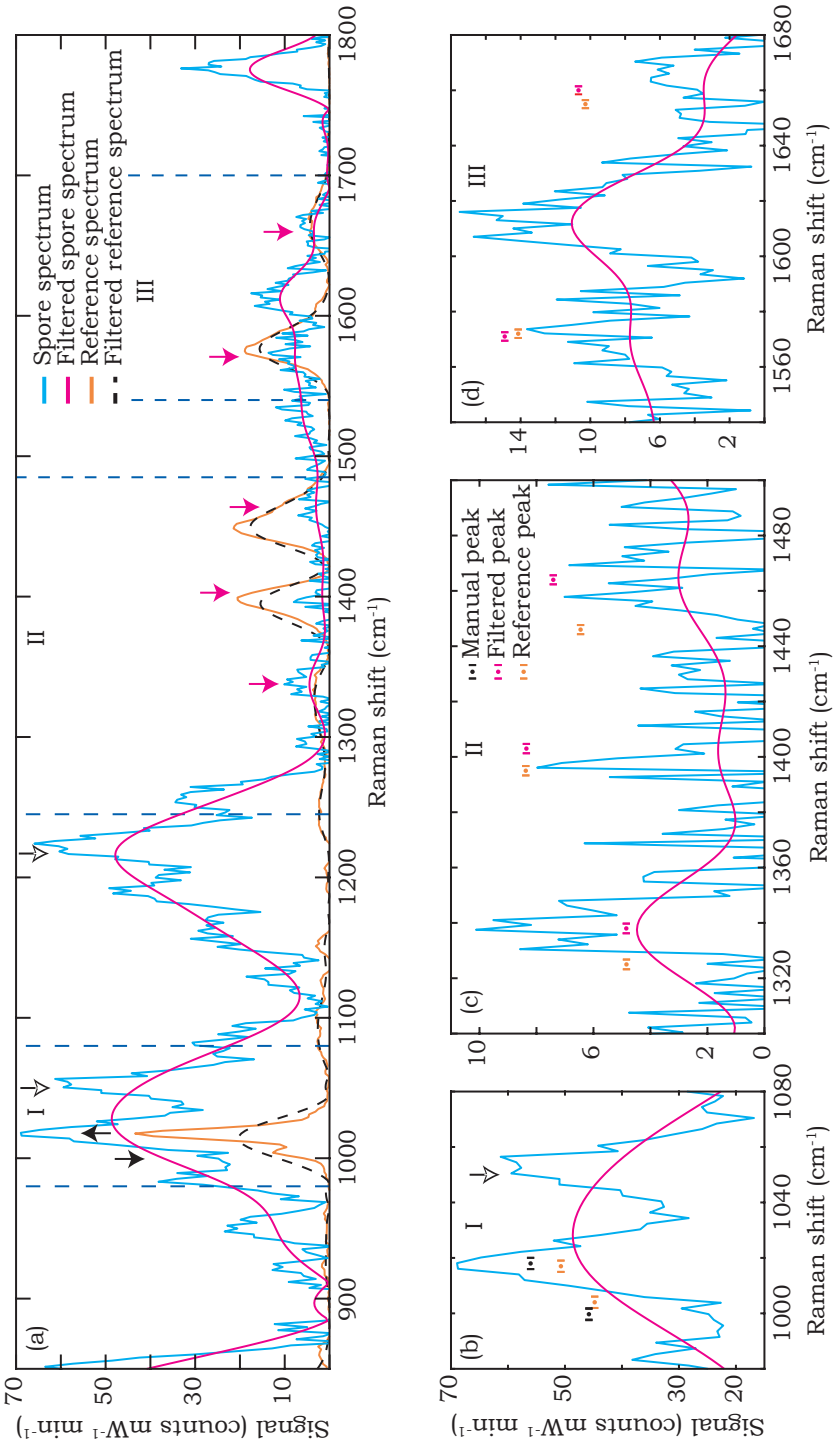

Figure 5.7: Figure 16 Few spores Raman spectra from the 5 μm trap. (a) Full spectrum with five assigned peaks (magenta arrows), two manually assigned peaks (black arrows) and two background peaks (open arrows). (b) Close up, showing the peaks at 1000 cm^{-1}, 1018 and 1050 cm^{-1}. (c) Close up, showing the spore peaks at 1338, 1403 and 1464 cm^{-1}. (d) Close up, showing the spore peaks at 1571 and 1660 cm^{-1}. The bars in plots (b-d) give the local spectrometer resolution at the position of the manually assigned peaks, the assigned peaks and the reference peaks.

As mentioned above, Table 5.1 provides an overview of the peak positions relevant to the spectra. Additionally, the SNR of the assigned peaks and the figures of merit for each measured spectrum are given.

The Table shows a range of SNR values from 6.3 to 0.03. The $\Delta\sigma_7$ and$\Delta\sigma_8$ peaks in the 5 µm few spores spectrum show the lowest SNR values. These SNR values are an indication of the quality of the spectrum. However, peaks are assigned based on a local maximum in the Fourier filtered spectrum. Thus, assignment also means that the SNR in the spore spectrum is sufficient to distinguish the peak in the Fourier filtered spectrum.

Comparing the spectra in Table 5.1, many spores to many spores and few spores to few spores, we find that the 5 µm trap spectra outperform the 10 µm trap spectra when it comes to maximum obtained SNR. However, when comparing the peaks in different spectra per reference peak, we find that the 10 µm many spores peaks always have the best or second to best SNR.

Table 5.1: Overview of the reference and measured peak positions and the figures of merit per spore spectrum. $\Delta\sigma_i$ $(i = 1:8)$ give the peak positions found in Figure 5.1 and 5.4-5.7. The signal-to-noise [SNR] is given for each assigned peak. The maximum SNR per spectrum is given in bold. $\overline{SNR}$ is the average SNR, $\overline{S}$ is the average signal defined as the average prominence in the filtered spectrum. Both are given for each measured spectrum.

	$\Delta\sigma_1$ (cm^{-1})	$\Delta\sigma_2$ (cm^{-1})	$\Delta\sigma_3$ (cm^{-1})	$\Delta\sigma_4$ (cm^{-1}) [SNR]	$\Delta\sigma_5$ (cm^{-1}) [SNR]	$\Delta\sigma_6$ (cm^{-1}) [SNR]	$\Delta\sigma_7$ (cm^{-1}) [SNR]	$\Delta\sigma_8$ (cm^{-1}) [SNR]	$\overline{SNR}$ (a.u.)	$\overline{S}$ (counts $mW^{-1}\,min^{-1}$)
Reference	1004	1017	1245	1330	1395	1448	1572	1655	-	-
10 µm many	1004	1016	1273	1332 [2.5]	1401 [0.9]	1458 [3.1]	1581 **[4.2]**	1653 [1.0]	2.3	2.8
10 µm few	-	1016	1272	1338 [0.5]	1405 [0.3]	1448 [0.9]	1595 **[1.3]**	1675 [0.1]	0.6	1.2
5 µm many	-	1018	-	1332 [0.6]	1410 [0.04]	1461 **[6.3]**	1587	1650	2.3	4.4
5 µm few	1000	1018	-	1338 **[1.5]**	1403 [0.1]	1464 [0.2]	1571 [0.03]	1660 [0.03]	0.4	0.8

5.4. DISCUSSION AND CONCLUSIONS

This chapter has presented a feasibility study of the dual-waveguide trap applied to bacterial spores. Here the discussion and conclusions from the aforementioned results are presented.

5.4.1. EVALUATION OF THE SETUP

The trapping and Raman experiments with the dual-waveguide traps indicated two major points of improvement. The first is to increase the fibre to chip coupling efficiency from the current approximate 4.1% towards the theoretical 89%. With this coupling efficiency a maximum of 210 mW would be available for trapping and Raman generation [92].

The second is to gain fluidic control such that the number of trapped particles can be determined at will and maintained indefinitely. This will prevent the premature ending of measurements due to particle collisions. Limiting the number of particles in the trap in combination with an increased trapping power will additionally reduce particle hopping. Consequently, the effective overlap between the acquisition volume and the Raman generating volume is increased, by preventing hopping to trap sites at the edge of the acquisition volume.

5.4.2. RAMAN SPECTRA OF *Bacillus subtilis* SPORES

Using the 10 and 5 μm dual-waveguide traps Raman spectra of many (#spores≥4) and few (#spores≤3) trapped bacterial spores were obtained. These categories were defined due to the lack of control over the number of trapped spores. The spectra presented for these categories are composed from multiple sequential frames selected based on the presence of the 1017 cm^{-1} spore peak. The spore spectra have a low signal-to-noise ratio and a background with a periodic component (see section 4.3.3). To remove the periodic component of the background, the spectra were filtered with a flattened Gaussian in the Fourier domain. This approach selectively filters the periodic peaks from the spectra, aiding Raman peak assignment. As it is in principal a low pass filter, it removes the noise from the spectra and can induce intensity decreases and small position shifts in Raman peaks. The latter is mainly observed for sharp and asymmetrical peaks. Because of the filters selectivity and the low signal-to-noise ratio of the spectra, this approach is preferred over e.g. a walking average as this could inadvertently add noise intensity to assigned peaks.

The filtered spectra are identified based on a minimum of three assigned spore peaks, although most present five. The assigned peak position display a shift with respect to the reference position in the order of the spectrometer resolution. This shift is in first approximation attributed to a calibration difference. However, an actual change in the molecular vibrations, and thus a shift of the peak positions and relative intensities, due to differences in sample environment and preparation can be a contributing factor, as is know from literature [14, 89]. To conclusively determine if this is the case, a higher signal intensity would be required. Alternatively, a direct reference of the used sample could be created with an independent trapping and Raman device.

To compare the Raman generation and acquisition performance of the traps the proportionality factor α ($mW^{-1}min^{-1}$) is used as defined by Wang *et al.*[93]

$$\alpha = \frac{SNR}{\sqrt{P * T}} \tag{5.2}$$

Here SNR denotes the signal-to-noise ratio and $(P * T)$ the Raman generating power acquisition time product. This relation is based on the fact that the SNR of shot noise limited spectra is proportional to the square root of the number of detected photons. The proportionality factor α depends on the quality of the measurement setup and the measured sample. Factors influencing α are, for instance, the NA of the used objective and the stability with which particles are trapped.

To put the obtained α values in perspective, we compare them to those of Wang et.al. [93] and De Luca *et al.* [94]. These articles provide a valuable benchmark of the α values that need to be achieved, as they were able to identify single *Escherichia coli* DH5α cells and bovine semen cells based on their Raman fingerprint.

To make a comparison with the bench marks, we take into account that α is inversely proportional to the illumination wavelength squared. Furthermore, it is assumed that the sample dependence of α remains within an order of magnitude for most types of cells and micro-organisms. We now find α values of 5.8 and 10.7 for ref. [93] and [94], respectively.

Using Equation 5.2, we find that the 10 μm and 5 μm traps produce average α values of 1.2 and 1.4. Furthermore, the average sequence lengths of the presented spectra, respectively 7 and 9 frames, suggest a higher trapping stability for the 5 μm trap. Combined, this points towards a higher performance of the 5 μm trap. This would be in line with the expected higher trapping stability and associated higher effective overlap between the Raman generating and acquisition volumes for the 5 μm trap (see Chapter 4. However, it can also be attributed to the fact that roughly four times as many experiments have been performed with the 5 μm trap as with the 10 μm trap. Further experiments would be needed to increase the significance of this difference.

Comparing the α values of the two dual-waveguide traps to the benchmarks we find that the system almost performs in the same order of magnitude as the reference systems. To match the SNR of the reference systems, a one to two orders of magnitude higher power-time product is required. This should be attainable, considering the aforementioned possible coupling improvement. Furthermore, an NA increase to match that of [94], would give a signal increase of about 25%.

5.4.3. CONCLUSIONS

Summarizing, it can be concluded that the dual-waveguide trap is a device capable of producing Raman signals of many (#spores≥4) and few (#spores≤3) trapped bacterial spores. The obtained spectra have a low SNR and contain a periodic background. Filtering with a flattened Gaussian in the Fourier domain did allow the assignment of three to five peak positions corresponding to those of reference spore peaks. This is seen by the author as proof that the spectra originate from the trapped spores. The fact that the dual-waveguide trap can function with a variety of trap widths shows that it can be further tailored to the size of the sample particles. The setup clearly requires improvements, however, it is plausible that the SNR values of the benchmarks can be realised.

6

CONCLUSIONS AND OUTLOOK

This final chapter provides the overall conclusions by answering the sub-research questions posed in the Introduction and by recapitulating the findings of the previous chapters. Subsequently, the implications of these answers for the main research question will be discussed. Following this, the Outlook will shortly discuss research suggestions and envision the basic architecture of an on-chip trapping and Raman based instrument.

6.1. CONCLUSIONS

The main research question, posed in the Introduction, was divided into four sub questions. These questions are here answered by reviewing the conclusions of the relevant chapters. Combining the answers to the sub questions we will arrive at the answer to the main research question.

Question 1

> "Are we able to identify micro-organisms based on Raman spectra obtained with laser tweezers Raman spectroscopy and treated by signal processing and pattern recognition? "

As demonstrated in Chapter 2 of this thesis, we were able to trap single cells of the yeast species *Kluyveromyces lactis* and *Saccharomyces cerevisiae* and obtained a Raman fingerprint from these. Using a Fisher's criterion based rule, the yeast cells where subsequently classified with accuracies of 85% (σ = 0.05%) and 79% (σ = 0.04%), respectively. From this, it is concluded that it is possible for our specific setup to identify micro-organisms using LTRS based single cell Raman spectroscopy and the appropriate signal processing and pattern recognition.

Furthermore, in Chapter 2 a large within species variation in the Raman spectra was found. This is theorized to be due to differences in cell phase between the individual cells.

Question 2

> "Is an on-chip dual-waveguide trap, fabricated in TripleX, capable of optically trapping individual particles in a microfluidic environment while generating a significant Raman signal from those particles?"

In Chapter 3 the trapping of single 1 µm polystyrene beads in the 5 µm wide fluidic channel of our TripleX based dual-waveguide trap was demonstrated. By comparing release experiments to simulations, it was found that a trapping force of up to 1.3 pN could be exerted on such a bead using 5.1 mW of laser power in the trap. This power was sufficient to produce recognizable Raman spectra of a single trapped polystyrene bead for acquisition times as short as 0.25 s. From this we conclude that a TripleX based on-chip dual-waveguide trap is indeed capable of optically trapping particles in a microfluidic environment while generating a significant Raman signal of those particles.

Furthermore, it was observed that trapped beads can hop between multiple stable trapping positions. In addition to the trapping of single polystyrene beads, it was found that the dual-waveguide trap can trap multiple beads simultaneously. These simultaneously trapped beads can form clumps or line up into chains along the optical axis.

Question 3

> "Is an on-chip TripleX dual-waveguide trap capable of trapping micro-organisms and producing Raman fingerprint spectrum from these?"

In Chapter 5 the trapping of Bacterial spores of the species Bacillus subtilis was demonstrated using both a 10 and 5 μm dual-waveguide trap. Trapping of individually suspended spores proved to be difficult. In the trapping experiments Raman spectra were acquired from few (#spores≤3) and many (#spores≥4) spores. The definition of these classes (few and many) combined with the assembly of spectra from sequences of frames resulted in spectra of defined numbers of spores, despite the lack of fluidic control. The presented spectra could be identified as spore spectra based on at least three peaks even though their signal-to-noise ratio was low. From the obtained signal-to-noise ratios it was found that the dual-waveguide trap system almost performs in the same order of magnitude as the optical traps in the references. From this it is concluded that a TripleX dual-waveguide trap can trap biological particles and produce Raman fingerprints from them.

It was further found that the measuring geometry of the dual-waveguide trap presents unexpected complications, arising from a background signal present in the on-chip beams emanating from the waveguides.

The main question

The main research question addressed with the research in this PhD thesis is:

> "Can an integrated dual-waveguide trap, as intended by Van Leest et al. [46], be realized and used to identify micro-organisms based on their Raman spectrum acquired from an optically trapped single cell?"

Based on the work presented in this thesis and the aforementioned conclusions we can answer this question. Yes, an integrated dual-waveguide trap, as intended by Van Leest et al.[46] can be realised. Yes, it can trap micro-organisms, however trapping a single micro-organise remains challenging, mainly due to the lack of control in the fluidics. Yes, it can generate Raman spectra from which the micro-organism can be recognised, however it is left to future research to prove that the obtained spectrum quality is sufficient to classify the micro-organisms.

6.2. OUTLOOK

This research has demonstrated the feasibility and potential of dual-waveguide lab-on-a-chip devices for on-chip trapping and Raman spectroscopy. However, the setup presented leaves room for improvement. In this Outlook suggestions for further research are presented, after which a dual-waveguide trap based instrument architecture will be envisioned.

6.2.1. RESEARCHING THE PHYSICS AND APPLICATION SUITABILITY

The presented research can be continued in two directions: further research into the physics of the dual-waveguide traps and improving the performance of the dual-waveguide traps. Both would benefit from a number of changes to the setup. Firstly, a more advanced chip-holder will improve the ease of use of the setup. In addition to efficient and stable coupling, it should feature a lid for the chip, such that the fluidic channel can be opened and easily cleaned. Ideally, this lid should allow the use of objectives with an $NA \geq 1.2$. These objectives would increase the amount of Raman signal acquired and can create an independent laser tweezers focus inside the fluidic channel. The latter can be an important tool in the further characterisation of the dual-waveguide traps. Furthermore, the holder should provide sufficient fluidic control [95] to at least create and maintain a zero flow environment in which experiments can reliably be performed.

Further research into the dual-waveguide trap's physics will be found in more refined experiments on particle trapping and Raman generation. In these experiments the detailed structure of the energy density, observed in simulations [92], should be investigated. Additionally, the effect of different types and sizes of particles on the trapping behaviour can be tested. These experiments should aim to find the operational upper and lower limits of the dual-waveguide trap for *e.g.* used power and particle size. In these experiments the independent laser tweezers focus can be used to deliver, position and hold particles in the trapping region at positions of interest. After calibration, it can also be used to determine the trapping strength of hot spots by either pulling trapped particles from the hot spots in so called or tug-of-war experiments [96] or by photonic force microscopy [97].

Improved performance of the presented system can first be sought in simplification of the path followed by the Raman signal through the setup. If the chip is made transparent, Raman signal collection can be done from the opposite side of the chip. After acquisition the Raman signal can be directly coupled to a fibre and presented to the spectrometer. This approach removes several optical components, such as lenses and mirrors, from the signal path, increasing the efficiency. Different techniques can be employed to boost performance even further. For example, the effect of different wavelengths and phase combinations on the energy density in the dual-waveguide trap can be explored. This approach can allow tailoring of the position and intensity of hot spots. More intense hot spots would provide stronger trapping and Raman generation. Controlled positioning of shallow hot spots could provide size selective trapping, based on the overlap of larger particles with multiple hot spots. The use of multiple wavelengths would also provide a method to isolate the Raman spectrum from the background and noise [98], thereby reducing the signal strength requirement.

6.2.2. ENVISIONING A DUAL-WAVEGUIDE TRAP BASED INSTRUMENT

The goal for many working with on-chip trapping and Raman characterisation of particles is an instrument to be used by non-expert operators in a point-of-care environment. In this section a possible instrument architecture for this goal will be discussed. As the instrument requirements will vary with the target application, blood analyses is chosen as an example application. Blood analysis forms a good example application, as blood contains many different particles that can be analysed with trapping and Raman devices. In addition, sample preparation can be limited to simple, well-established techniques such as fractioning.

A possible instrument architecture is envisioned as a table top appliance as it allows for more design freedom than a handheld version. The majority of single particle based analyses in blood require ratio determinations, *e.g.* the ratio between dormant and activated platelets [99]. These analyses require a high number of measurements to attain statistical significance. To make this possible in an acceptable time, the instrument is expected to have a large number of individual trapping and Raman devices. The number of devices will largely be determined by the footprint per device.

It can be envisioned that the instrument is based on a type of microwell plate where every well provides trapping and Raman functionality. Figure 6.1 shows a cross sectional and top view of such a plate which will be referred to as the device plate. The device plate can be fabricated monolithically and CMOS compatible in waveguiding platforms such as TripleX [43] or Si_3N_4. In the future this could be extended to for instance glasses or PMMA using femtosecond laser micro-structuring [100, 101]. Depending on its cost, estimated to be 4 euro per cm^2 at a CMOS research fab [102] ,the device plate can be reusable or disposable. A disposable device plate limits the cross-contamination risk. However, considering the typical materials and techniques used in CMOS fabrication a reusable device plate might be preferred from a sustainability viewpoint.

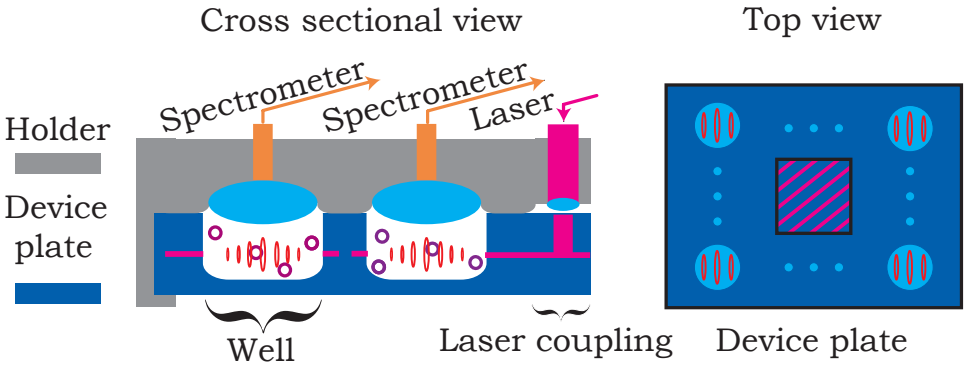

Figure 6.1: Impression of the proposed device architecture. (Cross sectional view) a cross sectional side view showing: two sample filled wells optically coupled via a lens and fibre array to one or more spectrometers and a fibre coupling a laser to the device plate. (Top view) a device plate with a NxN well array arranged around a central laser coupling grating (routing waveguides are not shown).

A sample filled device plate should slot precisely [103] into a holder in the instrument. Optical power is coupled from the holder to the device plate from a central point [104], after which it is routed to the individual traps (see Figure 6.1). The Raman signal, on the other hand, is collected out of plane by the holder per well. A first instrument version will use a combined lens and fibre array [105] to collect the Raman signal (see Figure 6.1) and route it to a spectrometer. Further on grating couplers might be used to collect the Raman signal from every well on the device plate [106].

The device plate holder can either function as an interface between the plate and components such as an external laser and an external spectrometer or it can, partially, integrate these functions. A gradual shift from limited to almost complete integration is expected as photonic techniques mature. For a first version table top instrument integration of functions into the holder should be considered with care. Integration of, for instance, lasers [107] can reduce waveguide routing issues in the device plate. However, this comes at the cost of considerable added complexity to the holder. Similarly the integration of spectrometers might reduce signal loss at the cost of the maximum resolving power [108].

Spectrometer integration can however be justified for blood analyses as many tests can be based on the measurement of few or even single bands in the spectrum. Examples of these are determining the oxygenation state of haemoglobin [109], the detection of Alzheimer's disease from platelets [110] and the diagnoses of thalassemia [111] and sickle cell disease [112]. For these applications only a limited resolving power is required. This allows the diffractive element of the spectrometer to be integrated in the form of for instance arrayed waveguide gratings [113] or further on tapered Bragg waveguides [114, 115].

The transport of particles to the trapping region can rely on Brownian motion. In this manner, sequential trapping events can be obtained from one well. However, the particle concentration in the sample has to be tuned to prevent the trapping of multiple particles while maintaining an acceptable repeat rate. Alternatively, the holder can provide fluidic connections to the device plate allowing the delivery of particles to the trapping region at the desired rate.

As is usually the case in a developing field, there are almost as many visions of a first instrument version as there are researchers. These are neither limited to trapping and Raman nor to spectroscopy [116, 117]. Only time will tell which of these visions will be realized. What is clear is that when these techniques mature to marketable instruments their impact will be considerable.

ACKNOWLEDGEMENTS

I have always been the type for long walks or hikes rather than sprints or marathons, my PhD turned out to be no different. As with hikes though-going can be made much lighter if you meet the right people on your way.

One of the first I had the pleasure of meeting was Thijs. At first I had to get used to your subtle appreciation of humour, especially my own, but we ended up sharing quite a few laughs in the office. Thank you for your patience in explaining all the different things in and outside the cleanroom and for your kind sternness when I was my largest obstacle. The cleanroom is a strange place where timing is more important than time and even simple tasks made me feel productive. This place would definitely not be the same without the cleanroom staff, who are always ready with a helping hand, expert advice or a wisecrack. Although none of the work with which you have helped me has made it into this thesis, I would like to thank you for all of it. This part would not be complete without thanking Ahmet and Delphine. You helped me out at times when I would have more than understood it if you wouldn't have. Thank you for doing so none the less.

Work in the cleanroom is aimed at work in the lab. As you don't get to pick the people with whom you spend a lot of time in these cramped dark rooms, I consider myself lucky to have met Martijn, Gyllion, Boling and Felipe there. Martijn, things didn't go as we planned, and I hope our mutual planning will improve in the future, but I'm glad that we made it work. Gyllion, it was a joy having you around, do me a favour and threat the lab as an escape room. Lab work requires things to fit just right, if it doesn't you ask the technicians. I want to thank Ron and Tom for all their efforts in helping me polish the rough edges off of things. Dennis, Jorne, Mathijs and Sven choose to join the (side) projects I was working on in the lab more or less voluntarily. My guess is that you didn't find what you were expecting and I still sometimes feel like I should apologize for that. However, I am grateful that you did join, really appreciate the work that you did and wish to you that your future project will live up to your expectations.

Of course there are many people involved with a PhD project that rarely, if ever, set foot in your lab, such as the other group members. I tend to think of a research group as an extended family with uncles, aunts, nieces and nephews related through the type of work they do rather than genetics. If this idea applies to QI than Ronald would be its grandmother, always keeping a sharp eye on the wellbeing of all the little children and handing out good advice were ever needed. Ronald I'm glad I got to meet you, even if it means that I now might have to suffer a kick to the shins every once in a while. From the nephews I want to thank Lennard and Robiel for all our coffee room discussions. I still think off our discussion triangle on a surprisingly regular basis especially when it is dark enough to read. I also want to thank Robert, Jelle, Lena, Tom and Yan for their support and more generally for making our research group more hospitable. Although they are not from our group, they might as well have been part of the family, I want to

thank Pascale, Marijke, Astrid, Jannie and Apilena who will start to help you even before you have had a change to tell them who you are. As a Wetsus PhD in Delft I was also a remote cousin to that family. I want to thank Wetsus and especially the sensoring theme table members for always making us feel welcome when we visited Leeuwarden and for their understanding when things did not go as we had hoped.

A really smart guy along the way told me that the most important things you learn during your PhD have very little to do with your research topic. I believe he is right. As learning can be done in different ways, I want to thank Helene and Andrea for teaching me how to dance, which was and continues to be more fun than I anticipated. Of course I also want to thank Fien, Tudor, Kitso, Martin, Bekir and all the other board and comity members of Rock 'n Delft. Thank you for all the small and large adventures we shared. Learning "new" Tai Chi styles in Delft was also quite an adventure, thank you Mevr. Wang and Kelvin for helping me stretch my limbs while other parts of me were in danger of over stretching. My mother once asked me, if fiddling around with outdated computer parts was of any use at all. Who would have guessed that it would put bread on my plate one day? I want to thank OGD for financing the last leg of my PhD. More than that, I want to thank the colleagues there and at TMH for their kindness, welcoming nature and the philosophical and sociological discussion we had. Especially I want to thank Odette and Carel for showing me new points of view, which would have been hard to learn in an academic setting. Further, I would like to thank Lucas and Jaap for allowing me to practices the things I have learned, which would have been very hard to do outside of academia.

Some people you meet at rest stops, where your paths cross, others walk along for longer stretches. Of those, I want to especially thank Tungky, Frank and Maaike. Thank you for listening to me complain about large and small things and for all the good advice. I also want to thank Ine and Emanuel for being the type of friends they are.

Finally, I would like to thank my family both the old ones and the new ones for all their support and understanding especially in the last writing stretch. Thank you, for providing me with examples, for holding the stones so that I had the chance to see the things that sparked my curiosity and for helping me understand things that you might not understand yourself.

Als aller Letzen möchte ich Anna danken, Danke, dass du mich begleitest und mir den Weg leichter machst. Kleines, ich hoffe, dass wir zusammen noch einen sehr weiten Weg gehen werden.

Jeroen Heldens

A

Appendix

Table A.1: Wilson notation of the various vibrational modes of the benzene moiety of the polystyrene polymer as observed in Figure 1.2 according to [21]

Wilson Number	Approximate Description of Vibration
1	Ring "breathing"
3	CH deformation
6a,6b	Ring deformation
8a,8b	Ring strectch
9a,9b	CH deformation
15	CH deformation
18a	CH deformation

B

Acronyms

CMOS Complementary Metal Oxide Semiconductor

DNA Deoxyribonucleic Acid

FDTD Finite-Difference Time-Domain

FIR Far Infrared

IR Infrared

KS Kolmogorov-Smirnov

LOC Lab-On-a-Chip

LTRS Laser Tweezers Raman Spectroscopy

NA Numerical aperture

NGS Next Generation Sequencing

NIR Near Infrared

OCT optical coherence tomography

PC Principal Component

PCA Principal Component Analysis

PCR Polymerase Chain Reaction

PDMS Polydimethylsiloxane

PMMA Polymethylmethacrylate

RNA Ribonucleic acid

SCRS Single Cell Raman Spectroscopy

WGD whole genome duplication

LIST OF FIGURES

1.1 Graphical representation of the frequencies involved in Raman scattering. An incident light wave, in this case with a wavelength of 785 nm (top left graph) interacts with a vibrational mode of a molecule, in this case the CH stretch mode (Wilson Number 2) of polystyrene (bottom left graph). This interaction induces a dipole oscillation in the molecule, which resembles the vibrational mode perturbed by the incident light wave (central graph). The oscillating dipole can radiate at two of three different frequencies. In the case that the vibrational mode was already populated the emitted light will have the sum frequency (top right graph) if the vibrational mode is relaxed which is called Anti-Stokes Raman scattering or the same frequency as the incident light (middle right graph) if the vibrational mode remains populated which is called Rayleigh scattering. In the case that the vibrational is mode is not populated at the moment of the interaction, the incident light will be either Rayleigh scattered or will have the difference frequency (bottom right graph) if the vibrational mode is excited which is called Stokes Raman scattering. 8

1.2 Raman spectrum of polystyrene. All save two peaks can be assigned to the various vibrational modes of the benzene moiety of the polystyrene polymer. These peaks have been labelled following the Wilson notation for benzene. [22, 23]. For the different vibrational modes, the reader is referred to appendix A. The two remaining peaks can be assigned to the vibrational stretching mode of the skeletal C-C bonds, for the broad peak around 800 cm^{-1} and the vibrational scissoring mode of the methylene bridge for the peak at 1450 cm^{-1} 10

1.3 Optical trapping, geometric and Rayleigh regime. In these figures red arrows denote light rays, blue and white arrows indicate imparted momentum, open arrows indicate net momentum and closed loops give iso-field lines. The geometrical optical explanation of optical trapping of particles much larger than the wavelength is based on the conservation of momentum between the trapped particle and the refracted and reflected light. In this case, the trapping of a particle can be decomposed in lateral and axial trapping. Axial trapping (a-b) is achieved by the balancing of the momentum transferred to the particle by the refracted light and the reflected light. Lateral trapping (c) results from the asymmetrical refraction and the corresponding un-balanced change in momentum, of light by a particle in an optical gradient. In both cases, a tighter focus produces a stronger trap although axial trapping is the most sensitive to this effect. The particle in this illustration is assumed to be of higher refractive index than its surroundings. In the Rayleigh scattering regime where the particle is much smaller than the wavelength (d) it can be treated as an induced dipole minimizing its energy by placing itself at the focus of the optical gradient. Figure based on Dholakia et al. [31] 12

1.4 TripleX box shell waveguide 15

2.1 Schematic drawing of the laser tweezers Raman spectrometer. Components: SM fibre – single mode fibre, F1 – clean-up filter, F2 – razor edge filter, L1, L2 – lenses beam expander, D1, D2 – dichroic mirrors, L3, L4 – lenses confocal filter, P1 – pinhole, L5 – aperture matching lens, F3 – filter set for camera. For the fluidic cell a zoomed-in view is shown where GS indicates the glass slides and PF the parafilm. The inset shows an image of an optically trapped yeast cell (encircled), adjacent to a group of cells with some of their organelles resolved. 24

2.2 (a) An example of a direct *K. lactis* spectrum (blue) and the corresponding spectrum reconstructed from the reduced number of PCs used the analysis (black). The Raman bands indicated by vertical lines (solid or dashed) agree with Raman bands found in yeast by [13, 51, 64] and have been associated with the indicated molecules. Solid lines have in addition been found by [65]. (b) Envelope spectra of *K. lactis* (blue) and *S. cerevisiae* (red). The envelopes are constructed from the training spectra by taking for each Raman shift the highest and the lowest intensity. Some sharp peaks, for example the two negative peaks indicated with an asterisk (∗) are residual cosmics. The hatched area indicates the overlap between the envelope spectra, showing that the *S. cerevisiae* envelope largely encloses the *K. lactis* envelope. 27

2.3 Linear classification of 48 *K. lactis* (blue) and 90 *S. cerevisiae* (red) test spectra. Circles denote correctly classified spectra, crosses incorrectly classified spectra. The classifier value is noted along the horizontal axis. The position of the data points with respect to the vertical dashed line at zero classifier value indicates their classification, with negative values corresponding to *K. lactis* and positive values corresponding to *S. cerevisiae*. The two empirical cumulative distributions, (solid lines), refer to the right vertical axis. The maximum vertical deviation D between the distributions amounts to 0.72 and is indicated by the double arrow. 29

3.1 (a) Cross-sectional schematic with dimensions and materials of the waveguide. The blue trapezoidal box shape is Si_3N_4. Both the inner region of the box and the surrounding cladding are SiO_2. (b) Cross-sectional SEM picture of a waveguide with the box structure. (c) Mode profile of the lowest TE mode in the waveguide, represented as P_z, the z-component of the Poynting vector. Colours from red to purple indicate increasing values of P_z. (d) Microscope image of the Raman trapping device taken while red light was coupled into the input waveguide to check waveguide continuity, giving the red glow. A 50/50 Y-junction splits the input waveguide in two half-circular arms (circle diameter = 7 mm), which guide the light to the fluidic channel. The waveguiding structures are imaged as white due to saturation of the camera. For clarity, white saturation regions due to scattering loss at the input waveguide and at the trap have been removed. (e) Microscope image of the central region of the device. Each of the two waveguides terminates in a wall of the 5 µm wide fluidic channel, which tapers up in two steps. Definition of the coordinate axes as indicated in b) and e). 36

3.2 Schematic of the setup for optical trapping and Raman spectroscopy with the dualwaveguide trap, which is clamped in a holder with ports for fluidic access. Components: CF - laser clean-up filter, FC - fibre coupler, M1, M2 - dichroic mirrors, M3 - beam splitter, L1, PH, L2 - lenses and pinhole of confocal filter, EF - razor edge filter, L3, L4 - aperture matching lens and imaging lens for spectrometer and camera, respectively. In most of the experiments, the power offered by the fibre to the input waveguide was 125 mW, as indicated. 37

3.3 Simulated patterns of the intensity of the electric field in (a) the xz-plane and (b) the yz-plane. The pattern results from excitation of the lowest TE mode and shows standing wave modulation due to beam interference. The polarization is in the x-direction. 39

3.4 Snapshots (a) and (b, c) of the online supplementary Media 1 and Media 2^3 , respectively. A single trapped bead can be seen in a). In b) and c) a lump a five trapped beads and a linear chain of four trapped beads are shown, respectively. The respective water flow velocities for the panels are 90, 34 and 43 µm/s. Dashed lines indicate the boundaries of the fluidic channel and the dual waveguides. 41

3.5 Calculated forces F_x, F_y+ (-) and F_z for displacement of a 1 µm polystyrene bead on the three corresponding axes. The axes y+ (y-) are defined in Figure 3.1b. 43

3.6 Raman spectra of an optically trapped polystyrene 1 µm bead, for integration times as indicated. Ptrap = 5.1 mW. The Raman shifts attached to the dashed lines have been taken from a standard Raman spectrum of polystyrene [83]. From the spectra a background has been subtracted and they have been slightly smoothed, as described in the text. The two 15 s spectra indicated with (A) and (B) demonstrate the repeatability of the measurements. The dotted lines are the axes of the respective spectra, showing that the intensity is negative for higher shifts as a result of the background-subtraction procedure (see text). The numbers in brackets adjacent to the integration times are the vertical offsets applied to the spectra for clarity. 46

4.1 Experimental setup used in this chapter. (blue) The main beam path. (red) The LTRS arm. (purple) The Raman arm. (green) The illumination arm. Components: L1-12 - lenses, CF - clean-up filter, FC – Newport 9131-M fibre coupler, Fi - Thorlabs PM-630-HP polarisation maintaining fibre, FL - fibre launcher, C - camera, ND - neutral density filters, Lamp - halogen lamp, D - diffuser plate, DF - diaphragm, BS - 50:50 beam splitter, D1, D2: dichroic mirror, M - silver mirror, O - Olympus UPLSAPO 60XW or LUMPLFLN 40XW objective, CH - chip holder, F - filter, P - pinhole ø=100 µm, S - spectrometer entrance slit, spectrometer Acton LS 785. Lens sets L1/L2, L4/L5 and L6/L7 form beam expanders. L9, P and L8 form a confocal filter. 52

4.2 Simulated dual-waveguide trap illumination volumes. From left to right the 5, 10 and 15 µm dual-waveguide trap. (colormap) Energy density (ρ_E). (dashed lines) The radial V_{il} boundary. (solid vertical white lines) The position of the channel wall. Data courtesy of Gyllion Loozen 54

4.3 Relevant volumes for Raman spectroscopy. (a) LTRS. (b) Dual-waveguide trap. Illumination volume: the region with sufficient intensity to generate Raman signal. Raman generating volume: the portion of the V_{il} occupied with Raman active substance. Acquisition volume: the volume from which Raman signal can be acquired. 55

4.4 Comparison of the background collection for empty and full traps. (a) For the LTRS a portion of the laser light is reflected and scattered back towards the objective by the interfaces of the fluidic cell. (b) When a particle is trapped, only the amount of laser light directed towards the objective changes. (c) For the dual-waveguide trap, most laser light is directed from one waveguide to the other. Only a small part of the diverging light or light scattered from the side walls will reach the objective. (d) When a particle is trapped in the dual-waveguide trap the amount of laser light that reaches the objective strongly increases. Furthermore, the spectral composition of this light will be different from the light collected without a trapped particle (not shown). 57

4.5 Ascorbic acid spectra. (Top) LTRS spectra. (orange) Solid ascorbic acid. (blue) Saturated ascorbic acid solution. (black markers) Literature peak positions. (orange markers) Solid ascorbic acid peak positions. (blue markers) Saturated ascorbic acid solution peak positions. Bars on the markers indicate the local spectrometer resolution. The peak positions (in cm^{-1}) are [Lit; solid; solution], [870.3; 871.0; 879.7], [1129; 1133; 1160], [1258; 1264, 1298], [1320; 1325; 1357], [1498; 1508; -], [1668; 1663; 1695]. (Bottom) Dual-waveguide trap spectra of a saturated ascorbic acid solution. (pairs of dashed lines) LTRS ascorbic acid peaks. The spacing between the lines indicate the local spectrometer resolution. 58

4.6 Background between 400 and 550 cm^{-1}. Each background is the average of eight spectra normalized to the intensities of the 1668 cm^{-1} peak. 60

4.7 Signal-to-background ratio versus trap size. Per trap size eight measurements have been performed. The signal-to-background ratio of the different traps shows an increasing trend with trap size. This plot has been normalized to the highest signal-to-background ratio. 61

4.8 Summed energy density in the 5, 10 and 15 µm dual-waveguide traps. (grey lines) Summation of the energy density from Figure 4.2 over the 1.2 µm confocal filter diameter in the direction of the fluidic channel. (black lines) Summed energy density treated with a moving average (width 1.2 µm) along the waveguide axes. Data courtesy of Gyllion Loozen. 61

4.9 Input spectrum. This spectrum was obtained by placing fibre Fi in the pinhole holder P in Figure 4.1. A notable difference between this spectrum and the background observed in Figure 4.6 is the absence of the relative sharp peaks and the slow decrease at higher shifts. The latter is not shown in Figure 4.6. This decrease is most likely absent in the input spectrum because dichroic mirror D2 is bypassed during its collection. 62

4.10 Depth dependent reflectivity analysis. (Left column) The background spectrum, DC-component and $I(k)$ between 410 and 903 cm^{-1} for the 5, 10, 15 and 20 µm traps. (Right column) Reflectivity as function of depth for the 5, 10, 15 and 20 µm traps. (black circle) Reflection peak. 64

5.1 Literature spectrum of *B. subtilis* obtained as average of 100 individual spore spectra. Reproduced from [89] with permission from dr. Li Yong-qing. . . 69

5.2 Experimental setup used in this chapter. (blue) The main beam path. (red) The LTRS arm. (purple) The Raman arm. (green) The illumination arm. Components: L1-12 - lenses, CF - clean-up filter, FC – Newport 9131-M fibre coupler, Fi - Thorlabs PM-630-HP polarisation maintaining fibre, FL - fibre launcher, C - camera, ND - neutral density filters, Lamp - halogen lamp, D - diffuser plate, DF - diaphragm, BS - 50:50 beam splitter, D1, D2: dichroic mirror, M - silver mirror, O - Olympus UPLSAPO 60XW or LUMPLFLN 40XW objective, CH - chip holder, F - filter, P - pinhole ø=100 µm, S - spectrometer entrance slit, spectrometer Acton LS 785. Lens sets L1/L2, L4/L5 and L6/L7 form beam expanders. L9, P and L8 form a confocal filter. 70

5.3 Examples of single frame spectra. (blue line) A single frame containing spore signal. (black line) A single frame without spore signal. The dashed lines indicate the range used to determine the presence of spore signal. . 71

5.4 Many spores Raman spectrum from the 10 μm trap. (a) Full spectrum with five assigned peaks (magenta arrows), three manually assigned peaks (black arrows) and three background peaks (open arrows). (b) Close up, showing the peaks at 1004, 1016 and 1044 cm^{-1}. (c) Close up, showing the shoulder at 1273 cm^{-1} and the assigned peaks at 1332, 1401 and 1458 $^{-1}$. (d) Close up, showing the assigned peaks at 1581 and 1653 cm^{-1}. The bars in plots (b-d) give the local spectrometer resolution at the position of the manually assigned peaks, the assigned peaks and the reference peaks. . . 75

5.5 Figure 14 Few spores Raman spectrum from the 10 μm trap. (a) Full spectrum with five assigned peaks (magenta arrows), two manually assigned peaks (black arrows) and three background peaks (open arrows). (b) Close up, showing the peaks at 1016 and 1042 cm^{-1}. (c) Close up, showing the spore peaks at 1338, 1405 and 1448 cm^{-1}. (d) Close up, showing the assigned peaks at 1572 and 1655 cm^{-1}. The bars in plots (b-d) give the local spectrometer resolution at the position of the manually assigned peaks, the assigned peaks and the reference peaks. 76

5.6 Figure 15 Many spores Raman spectrum from the 5 μm trap. (a) Full spectrum with three assigned peaks (magenta arrows), three manually assigned peaks (black arrows) and two background peaks (open arrows). (b) Close up, showing the peaks at 1018 and 1050 cm^{-1}. (c) Close up, showing the spore peaks at 1332, 1410 and 1461 cm^{-1}. (d) Close up, showing the peaks at 1587 and 1650 cm^{-1}. The bars in plots (b-d) give the local spectrometer resolution at the position of the manually assigned peaks, the assigned peaks and the reference peaks. 78

5.7 Figure 16 Few spores Raman spectra from the 5 μm trap. (a) Full spectrum with five assigned peaks (magenta arrows), two manually assigned peaks (black arrows) and two background peaks (open arrows). (b) Close up, showing the peaks at 1000 cm^{-1}, 1018 and 1050 cm^{-1}. (c) Close up, showing the spore peaks at 1338, 1403 and 1464 cm^{-1}. (d) Close up, showing the spore peaks at 1571 and 1660 cm^{-1}. The bars in plots (b-d) give the local spectrometer resolution at the position of the manually assigned peaks, the assigned peaks and the reference peaks. 79

6.1 Impression of the proposed device architecture. (Cross sectional view) a cross sectional side view showing: two sample filled wells optically coupled via a lens and fibre array to one or more spectrometers and a fibre coupling a laser to the device plate. (Top view) a device plate with a NxN well array arranged around a central laser coupling grating (routing waveguides are not shown). 89

CURRICULUM VITÆ

Jeroen Theodoor Heldens

09-03-1984 Born in Roermond, The Netherlands

EDUCATION

2010 - 2019 Wetsus PhD Project,
Topic: "Trapping and Raman sensing of bacteria in water
using photonic crystal cavities"
Kavli Institute of Nanoscience and Department of Imaging Physics,
Delft University of Technology

2006 - 2009 Master Natural Sciences,
Master project: "Molecular wires based on hybrid peptide-OPV compounds"
Radboud Universiteit Nijmegen

2002 - 2006 Bachelor Natural Sciences,
Bachelor project: "The fabrication of 3 dimensional Polymer-Dispersed
Liquid-Crystal Photonic Crystals, by the use of
the four non-coplanar beams approach"
Radboud Universiteit Nijmegen

1997 - 2002 VWO,
Profile: "Natuur & Techniek" and "Natuur & Gezondheid"
Bisschoppelijk College Schöndeln in Roermond

WORK

since 2018	WPO at Corbion, for OGD
since 2017	SSD and WPB (Polaris), for OGD
2015 - 2017	WPO at Thomas More Hogeschool Rotterdam , for OGD
2010 - 2017	Research Assistant, Department of Imaging Physics, Quantitative Imaging Group (Prof. dr. ir. L.J. van Vliet) Delft University of Technology, The Netherlands
2006 - 2008	Master Internship Departmens of Bio-Organic Chemistry (Prof. dr. ir. J. C. M. van Hest) and Spectroscopy of Solids and Interfaces (Prof. dr. T. H. M. Rasing) Radboud Universiteit Nijmegen
2005 -2006	Bachelor Internship Department of Spectroscopy of Solids and Interfaces (Prof. dr. T. H. M. Rasing) Radboud Universiteit Nijmegen

LIST OF PUBLICATIONS

7. **J.T. Heldens, D.K. Leenman, M.A.H. Luttik, P.A.S. Daran-Lapujade, L.J. van Vliet and J. Caro**, *Classification of yeast species using single cell Raman tweezers spectroscopy*, to be published (2019)

6. **M. Boerkamp, T. van Leest, J. T. Heldens, A. Leinse, M. Hoekman, R. Heideman, J. Caro**, *On-chip optical trapping and Raman spectroscopy using a TripleX dual-waveguide trap*, Opt. Express, vol. 22, no. 14, pp. 30528-30537 (2014)

5. **J. Caro, J. T. Heldens, D. K. Leenman**, *A numerical re-evaluation of the Mcdonald-Vaughan model for Raman depth profiling*, In Wax, AP, Backman, V (eds.), Proc. of SPIE , vol. 8592 , pp. 859219-1-6 (2013)

4. **M. Boerkamp, J. T. Heldens, T. van Leest, A. Leinse, M. Hoekman, R. Heideman, and J. Caro**, *On-chip Raman spectroscopy with a TripleX dual-waveguide trap*, In Proc. of Symposium IEEE Photonics Society Benelux, Eindhoven , p.283-286 (2013)

3. **T. van Leest, J. T. Heldens, B. van der Gaag, J. Caro**, *Photonic crystal cavities for resonant evanescent field trapping of single bacteria*, Proc. of SPIE, Biophotonics: Photonic Solutions for Better Health Care III, vol. 8427, pp. 6 (2012)

2. **J. T. Heldens, D. K. Leenman, M. A. H. Luttik, P. A. S. Daran-Lapujade, J. T. Pronk, J. Caro**, *Discrimination of single yeast cells with Raman spectroscopy: Saccharomyces cerevisiae and Kluyveromyces lactis*, EOS Annual Meeting (EOSAM 2012) September 2012, Aberdeen (2012) (Poster)

1. **R. Matmour, I. De Cat, S. J. George, W. Adriaens, P. Leclere, P. H. H. Bomans, N. A. J. M. Sommerdijk, J. C. Gielen, P. C. M. Christianen, J. T. Heldens, J. C. M. van Hest, D. W. P. M. Löwik, S. De Feyter, E.W. Meijer, A. P. H. J. Schenning**, *Oligo(p-phenylenevinylene)-Peptide Conjugates: Synthesis and Self-Assembly in Solution and at the Solid-Liquid Interface*, J. Am. Chem. Soc., vol. 130, no. 44, pp. 14576–14583 (2008)

REFERENCES

REFERENCES

[1] W. Keuning, *Eindelijk helderheid in het Friese drinkwater,* (2010).

[2] X. Didelot, R. Bowden, D. J. Wilson, T. E. a. Peto, and D. W. Crook, *Transforming clinical microbiology with bacterial genome sequencing,* Nature Reviews Genetics **13**, 601 (2012).

[3] P. Francois, A. Huyghe, Y. Charbonnier, M. Bento, S. Herzig, I. Topolski, B. Fleury, D. Lew, P. Vaudaux, S. Harbarth, W. Van Leeuwen, A. Van Belkum, D. S. Blanc, D. Pittet, and J. Schrenzel, *Use of an automated multiple-locus, variable-number tandem repeat-based method for rapid and high-throughput genotyping of Staphylococcus aureus isolates,* Journal of Clinical Microbiology **43**, 3346 (2005).

[4] W. M. Dunne, L. F. Westblade, and B. Ford, *Next-generation and whole-genome sequencing in the diagnostic clinical microbiology laboratory,* European Journal of Clinical Microbiology and Infectious Diseases **31**, 1719 (2012).

[5] J. Eid, A. Fehr, J. Gray, K. Luong, J. Lyle, G. Otto, P. Peluso, D. Rank, P. Baybayan, B. Bettman, A. Bibillo, K. Bjornson, B. Chaudhuri, F. Christians, R. Cicero, S. Clark, R. Dalal, A. DeWinter, J. Dixon, M. Foquet, A. Gaertner, P. Hardenbol, C. Heiner, K. Hester, D. Holden, G. Kearns, X. Kong, R. Kuse, Y. Lacroix, S. Lin, P. Lundquist, C. Ma, P. Marks, M. Maxham, D. Murphy, I. Park, T. Pham, M. Phillips, J. Roy, R. Sebra, G. Shen, J. Sorenson, A. Tomaney, K. Travers, M. Trulson, J. Vieceli, J. Wegener, D. Wu, A. Yang, D. Zaccarin, P. Zhao, F. Zhong, J. Korlach, and S. Turner, *Real-Time DNA Sequencing from Single Polymerase Molecules,* Science **323**, 133 (2009).

[6] S. Howorka, S. Cheley, and H. Bayley, *Sequence-specific detection of individual DNA strands using engineered nanopores.* Nature biotechnology **19**, 636 (2001).

[7] R. M. Gibson, C. L. Schmotzer, and M. E. Quiñones-Mateu, *Next-generation sequencing to help monitor patients infected with HIV: Ready for clinical use?* Current Infectious Disease Reports **16** (2014), 10.1007/s11908-014-0401-5.

[8] V. P. Barber and J. J. Newby, *Jet-cooled fluorescence spectroscopy of a natural product: Anethole,* Journal of Physical Chemistry A **117**, 12831 (2013).

[9] R. Amann and B. M. Fuchs, *Single-cell identification in microbial communities by improved fluorescence in situ hybridization techniques.* Nature reviews. Microbiology **6**, 339 (2008).

[10] M. Sohn, D. S. Himmelsbach, F. E. Barton, and P. J. Fedorka-cray, *Fluorescence Spectroscopy for Rapid Detection and Classification of Bacterial Pathogens,* Applied Spectroscopy **63**, 1251 (2009).

[11] H. E. Giana, L. J. Silviera, R. A. Zângaro, and M. T. T. Pacheco, *Rapid identification of bacterial species by fluorescence spectroscopy and classification through principal components analysis,* Journal of Fluorescence **13**, 489 (2003).

[12] P. Rösch, M. Harz, M. Schmitt, and J. Popp, *Raman spectroscopic identification of single yeast cells,* Journal of Raman Spectroscopy **36**, 377 (2005).

[13] P. Rösch, M. Harz, and K. Peschke, *Identification of single eukaryotic cells with micro-Raman spectroscopy,* Biopolymers **82**, 312 (2006).

[14] G. P. Singh, C. M. Creely, G. Volpe, H. Grötsch, and D. Petrov, *Real-time detection of hyperosmotic stress response in optically trapped single yeast cells using Raman microspectroscopy.* Analytical chemistry **77**, 2564 (2005).

[15] C. V. Raman and K. S. Krishan, *A New Type of Secondary Radiation,* Nature **121**, 501 (1928).

[16] D. A. Long, *The Raman effect a unified treatment of the theory of raman scattering by molecules* (John Wiley & Sons Ltd, 2002) p. 597.

[17] G. Placzek, *Handbuch der Radiologie*, edited by E. Marx, Vol. 6 (Akademische Verlagsgesellschaft, 1934) pp. 205–374.

[18] I. S. Arvanitoyannis, A. C. Stratakos, P. Tsarouhas, I. Atomic, E. Agency, A. Bakri, N. Heather, J. Hendrichs, I. Ferris, C. H. Bell, B. B. Harral, T. J. W. Smith, S. T. Conyers, K. A. Mills, S. K. Cardwell, B. E. Llewellin, A. Bonifacio, R. Guidetti, T. Altiero, V. Sergo, L. Rebecchi, T. Bowen, G. a. Dover, R. J. C. Cannon, G. J. Hallman, C. M. Blackburn, P. J. Caspers, G. W. Lucassen, E. A. Carter, H. A. Bruining, G. J. Puppels, C. Crews, M. Driffield, C. Thomas, I. Dalle-Donne, R. Rossi, D. Giustarini, A. Milzani, R. Colombo, K. D. Datkhile, R. Mukhopadhyaya, T. K. Dongre, B. B. Nath, I. V. Ermakov, M. Sharifzadeh, M. Ermakova, W. Gellermann, P. Ferrier, P. a. Follett, A. Swedman, D. K. Price, K. Snook, M. Wall, W. Bailey, R. V. Glatz, D. W. Hahn, G. J. Hallman, R. L. Hellmich, V. Arthur, C. M. Blackburn, A. G. Parker, R. L. Hellmich, N. M. Levang-Brilz, J. L. Zettler, I. C. Winborne, A. G. Parker, C. M. Blackburn, H. Huang, H. Shi, S. Feng, W. Chen, Y. Yu, D. Lin, R. Chen, X. Huang, M. F. Poelchau, P. a. Armbruster, D. Jayas, S. Jeyamkondan, A. A. Kader, D. Zagory, E. L. Kerbel, A. M. Khalil, M. H. Gagaa, a. M. Alshamali, R. Kizil, J. Irudayaraj, R. T. Kozikowski, S. E. Smith, J. a. Lee, W. L. Castleman, B. S. Sorg, D. W. Hahn, C. A. Lieber, S. K. Majumder, D. L. Ellis, D. D. Billheimer, A. Mahadevan-Jansen, H. Lu, J. Zhou, S. Xiong, S. Zhao, J. P. Madigan, H. L. Chotkowski, R. L. Glaser, M. Mansour, G. Franz, Q. Matthews, A. Brolo, J. Lum, X. Duan, A. Jirasek, N. Mir, R. M. Beaudry, C. Nansen, A. Coelho, J. M. Vieira, J. R. P. Parra, L. D. Geremias, Y. Xue, F. Huang, J. R. P. Parra, L. G. Neven, M. Morford, H. Nöthel, H. Nothel, B. Strese, I. Notingher, S. Verrier, S. Haque, J. M. Polak, L. L. Hench, E. K. Oztekin, S. E.

Smith, D. W. Hahn, J. H. Pyo, J. S. Park, H. J. Na, H. J. Jeon, S. H. Lee, J. G. Kim, S. Y. Park, Y. W. Jin, Y. S. Kim, M. a. Yoo, B. Qi, C. Zhao, E. Youn, C. Nansen, C. Redon, D. Pilch, E. P. Rogakou, O. Sedelnikova, K. Newrock, W. M. Bonner, S. S. Resilva, R. Pereira, E. P. Rogakou, C. Boon, C. Redon, W. M. Bonner, B. Sachdev, M. Zarin, Z. Khan, P. Malhotra, R. K. Seth, R. K. Bhatnagar, E. Shaurub, C. P. Shaw, A. Jirasek, J.-K. K. Shim, T. T. Aye, D.-W. W. Kim, Y. J. Kwon, J.-H. H. Kwon, K.-Y. Y. Lee, M. S. Siddiqui, E. Filomeni, M. François, S. R. Collins, T. Cooper, R. V. Glatz, P. W. Taylor, M. F. Fenech, W. R. Leifert, M. Smutná, K. Beňová, P. Dvořák, T. Nekvapil, V. Kopřiva, D. Maté, S. Surisan, P. Hormchan, S. Jamornmarn, M. Teresa, Y.-n. Alejandro, J. R. True, B. Verlag, I. Zucker, U. B. Eichler, D. C. Klein, H. Gainer, V. P. Whittaker, I. Z. Boctor, J. a. Weil, J. R. Bolton, M. Yamauchi, K. Suzuki, S. Kodama, and M. Watanabe, *Effects of irradiation on phenoloxidase levels in codling moth (Lepidoptera: Tortricidae) larvae,* Journal of Economic Entomology **106**, 734 (2013), arXiv:NIHMS150003 .

[19] D. G. Fouche and R. K. Chang, *Relative Raman cross section for O3, CH4, C 3H8, NO, N2O, and H2,* Applied Physics Letters **20**, 256 (1972).

[20] M. PENNEY, C M; GOLDMAN, L M ; LAPP, *Raman Scattering Cross Sections,* Nature **235(58)**, 110 (1972).

[21] F. D. Dollish, W. G. Fateley, and F. F. Bentley, *Characteristic Raman frequencies of organic compounds* (John Wiley & Sons Ltd, 1974) p. 407.

[22] E. B. Wilson, *The Normal Modes and Frequencies of Vibration of the Regular Plane Hexagon Model of the Benzene Molecule,* Physical Review **45**, 706 (1934).

[23] R. W. H. Dana W. Mayo, Foil A. MIller, *Course Notes on the Interpretation of Infrared and Raman Spectra* (John Wiley & Sons Ltd, 2004) p. 583.

[24] K. C. Neuman, E. H. Chadd, G. F. Liou, K. Bergman, and S. M. Block, *Characterization of photodamage to Escherichia coli in optical traps,* Biophysical Journal **77**, 2856 (1999).

[25] A. Ashkin, *Acceleration and trapping of particles by radiation pressure,* Physical review letters , 24 (1970).

[26] T. Van Leest and J. Caro, *Cavity-enhanced optical trapping of bacteria using a silicon photonic crystal,* Lab on a Chip **13**, 4358 (2013).

[27] S. Mandal, X. Serey, and D. Erickson, *Nanomanipulation using silicon photonic crystal resonators.* Nano letters **10**, 99 (2010).

[28] C. Faigle, F. Lautenschläger, G. Whyte, P. Homewood, E. Martín-Badosa, and J. Guck, *A monolithic glass chip for active single-cell sorting based on mechanical phenotyping.* Lab on a chip **15**, 1267 (2015), arXiv:_barata Materials and Techniques of polychrome wooden sculpture .

[29] M. Dienerowitz, M. Mazilu, and K. Dholakia, *Optical manipulation of nanoparticles: a review,* Journal of Nanophotonics **2**, 021875 (2008).

[30] D. J. Stevenson, F. Gunn-Moore, and K. Dholakia, *Light forces the pace: optical manipulation for biophotonics.* Journal of biomedical optics **15**, 041503 (2011).

[31] K. Dholakia, P. Reece, and M. Gu, *Optical micromanipulation,* Chem. Soc. Rev. **37**, 42 (2008).

[32] J. D. Jackson, *Classical electrodynamics*, 3rd ed. (Wiley, John, 1999) p. 808.

[33] M. Ghodbane, E. C. Stucky, T. J. Maguire, R. S. Schloss, D. I. Shreiber, J. D. Zahn, and M. L. Yarmush, *Development and validation of a microfluidic immunoassay capable of multiplexing parallel samples in microliter volumes,* Lab Chip **15**, 3211 (2015).

[34] G. Si, W. Yang, S. Bi, C. Luo, and Q. Ouyang, *A parallel diffusion-based microfluidic device for bacterial chemotaxis analysis,* Royal Society of Chemistry **12**, 1389 (2012).

[35] A. Kling, C. Chatelle, L. Armbrecht, E. Qelibari, J. Kieninger, C. Dincer, W. Weber, and G. Urban, *Multianalyte Antibiotic Detection on an Electrochemical Microfluidic Platform,* Analytical Chemistry **88**, 10036 (2016).

[36] P. C. Ashok, A. C. De Luca, M. Mazilu, and K. Dholakia, *Enhanced bioanalyte detection in waveguide confined Raman spectroscopy using wavelength modulation.* Journal of biophotonics **4**, 514 (2011).

[37] P. C. Ashok, G. P. Singh, H. a. Rendall, T. F. Krauss, and K. Dholakia, *Waveguide confined Raman spectroscopy for microfluidic interrogation.* Lab on a chip **11**, 1262 (2011).

[38] A. Constable, J. Kim, J. Mervis, F. Zarinetchi, and M. Prentiss, *Demonstration of a fiber-optical light-force trap,* Optics Letters **18**, 1867 (1993).

[39] P. R. T. Jess, V. Garcés-Chávez, D. Smith, M. Mazilu, L. Paterson, A. Riches, C. S. Herrington, W. Sibbett, and K. Dholakia, *Dual beam fibre trap for Raman microspectroscopy of single cells.* Optics express **14**, 5779 (2006).

[40] S. Dochow, M. Becker, R. Spittel, C. Beleites, S. Stanca, I. Latka, K. Schuster, J. Kobelke, S. Unger, T. Henkel, G. Mayer, J. Albert, M. Rothhardt, C. Krafft, and J. Popp, *Raman-on-chip device and detection fibres with fibre Bragg grating for analysis of solutions and particles.* Lab on a chip **13**, 1109 (2013).

[41] F. L. Royo, *Fabrication of Silicon Photonics Devices,* in *Handbook of Silicon Photonics* (CRC Press, 2013) Chap. 12, pp. 611–677.

[42] P. Løvhaugen, B. S. Ahluwalia, T. R. Huser, and O. G. Hellesø, *Serial Raman spectroscopy of particles trapped on a waveguide,* Optics Express **21**, 2964 (2013).

[43] K. Wörhoff, R. G. Heideman, A. Leinse, and M. Hoekman, *TriPleX: A versatile dielectric photonic platform,* Advanced Optical Technologies **4**, 189 (2015).

[44] J. F. Bauters, M. J. R. Heck, D. D. John, J. S. Barton, C. M. Bruinink, A. Leinse, R. G. Heideman, D. J. Blumenthal, and J. E. Bowers, *Planar waveguides with less than 0.1dB/m propagation loss fabricated with wafer bonding,* Optics Express **19**, 24090 (2011).

[45] G. Yurtsever, B. Považay, A. Alex, B. Zabihian, W. Drexler, and R. Baets, *Photonic integrated Mach-Zehnder interferometer with an on-chip reference arm for optical coherence tomography,* Biomedical Optics Express **5**, 1050 (2014).

[46] M. M. van Leest, F. Bernal Arango, and J. Caro, *Optical forces and trapping potentials of a dual-waveguide trap based on multimode solid-core waveguides,* Journal of the European Optical Society **6**, 39 (2011).

[47] J. Liu, S. Miao, W. Huang, E. R. Turner, Y. Luo, J. Li, Q. Wang, and S. Yan, *Identification of Clostridium butyricum as the bacteria causing soy sauce explosion and leakage and its control using nisin,* Food Control **34**, 509 (2013).

[48] M. Ros-Chumillas, M. Egea-Cortines, A. Lopez-Gomez, and J. Weiss, *Evaluation of a rapid DNA extraction method to detect yeast cells by PCR in orange juice,* Food Control **18**, 33 (2007).

[49] K. Dierick, E. V. Coillie, I. Swiecicka, H. Devlieger, A. Meulemans, L. Fourie, M. Heyndrickx, G. Meyfroidt, G. Hoedemaekers, and J. Mahillon, *Fatal family outbreak of Bacillus cereus-associated food poisoning,* JOURNAL OF CLINICAL MICROBIOLOGY **43**, 4277 (2005).

[50] C. Kirschner, K. Maquelin, and P. Pina, *Classification and identification of enterococci: a comparative phenotypic, genotypic, and vibrational spectroscopic study,* Journal of clinical microbiology **39**, 1763 (2001).

[51] S. B. Rodriguez, M. A. Thornton, and R. J. Thornton, *Use of Raman spectroscopy and chemometrics for identification and strain discrimination of the wine spoilage yeasts, Saccharomyces cerevisiae, Zygosaccharomyces bailii, and Brettanomyces burxellensis,* Applied and environmental microbiology **79**, 6264 (2013).

[52] R. Rodicio and J. J. Heinisch, *Yeast on the milky way: genetics, physiology and biotechnology of Kluyveromyces lactis.* Yeast (Chichester, England) **30**, 165 (2013).

[53] K.-K. Hong and J. Nielsen, *Metabolic engineering of Saccharomyces cerevisiae: a key cell factory platform for future biorefineries.* Cellular and molecular life sciences : CMLS **69**, 2671 (2012).

[54] Y. Tsuda, H. Yasutake, A. Ishijima, and T. Yanagida, *Torsional rigidity of single actin filaments and actin-actin bond breaking force under torsion measured directly by in vitro micromanipulation.* Proceedings of the National Academy of Sciences of the United States of America **93**, 12937 (1996).

[55] C. Xie, J. Mace, M. A. Dinno, Y. Q. Li, W. Tang, R. J. Newton, and P. J. Gemperline, *Identification of single bacterial cells in aqueous solution using confocal laser tweezers Raman spectroscopy.* Analytical chemistry **77**, 4390 (2005).

[56] J. W. Chan, *Recent advances in laser tweezers Raman spectroscopy (LTRS) for label-free analysis of single cells.* Journal of biophotonics **6**, 36 (2013).

[57] C. Verduyn, E. Postma, W. a. Scheffers, and J. P. Van Dijken, *Effect of benzoic acid on metabolic fluxes in yeasts: a continuous-culture study on the regulation of respiration and alcoholic fermentation.* Yeast (Chichester, England) **8**, 501 (1992).

[58] A. Macdonald and A. S. Vaughan, *Numerical simulations of confocal Raman spectroscopic depth profiles of materials: a photon scattering approach,* Journal of Raman Spectroscopy **38**, 584 (2007).

[59] J. Caro, J. T. Heldens, and D. Leenman, *A numerical re-evaluation of the Mcdonald-Vaughan model for Raman depth profiling,* in *Proc. of SPIE Vol. 8592 859219-1*, 1, edited by A. P. Wax and V. Backman (2013) p. 6.

[60] M. L. Bennink, S. H. Leuba, G. H. Leno, J. Zlatanova, B. G. de Grooth, and J. Greve, *Unfolding individual nucleosomes by stretching single chromatin fibers with optical tweezers.* Nature structural biology **8**, 606 (2001).

[61] F. Vogt and B. Mizaikoff, *Dynamic determination of the dimension of PCA calibration models using F-statistics,* Journal of Chemometrics **17**, 346 (2003).

[62] A. R. Webb, *Statistical pattern recognition*, 2nd ed. (John Wiley & Sons Ltd, 2002) p. 496.

[63] I. Young, *Proof without prejudice: use of the Kolmogorov-Smirnov test for the analysis of histograms from flow systems and other sources.* Journal of Histochemistry & Cytochemistry **25**, 935 (1977).

[64] G. P. Singh, G. Volpe, C. M. Creely, H. Grötsch, I. M. Geli, and D. Petrov, *The lag phase and G1 phase of a single yeast cell monitored by Raman microspectroscopy,* Journal of Raman Spectroscopy **37**, 858 (2006).

[65] J. De Gelder, K. De Gussem, P. Vandenabeele, P. De Vos, and L. Moens, *Methods for extracting biochemical information from bacterial Raman spectra: an explorative study on Cupriavidus metallidurans.* Analytica chimica acta **585**, 234 (2007).

[66] R. J. Swain, G. Jell, and M. M. Stevens, *Non-invasive analysis of cell cycle dynamics in single living cells with Raman micro-spectroscopy.* Journal of cellular biochemistry **104**, 1427 (2008).

[67] Y.-S. Huang, T. Karashima, M. Yamamoto, and H.-o. Hamaguchi, *Molecular-level investigation of the structure, transformation, and bioactivity of single living fission yeast cells by time- and space-resolved Raman spectroscopy.* Biochemistry **44**, 10009 (2005).

[68] K. Wolfe and D. Shields, *Molecular evidence for an ancient duplication of the entire yeast genome,* Nature **387**, 708 (1997).

[69] M. Delic, M. Valli, A. B. Graf, M. Pfeffer, D. Mattanovich, and B. Gasser, *The secretory pathway: exploring yeast diversity.* FEMS microbiology reviews **37**, 872 (2013).

[70] N. Moscelli, V. Malvaioli, F. Iuliano, and M. Vellekoop, *A microfluidic system for full hydrodynamic focusing control,* Procedia Engineering **25**, 803 (2011).

[71] J. Tsibouklis, M. Stone, A. A. Thorpe, P. Graham, T. G. Nevell, and R. J. Ewen, *Inhibiting bacterial adhesion onto surfaces: the non-stick coating approach,* International Journal of Adhesion and Adhesives **20**, 91 (2000).

[72] M. B. Fenn, V. Pappu, P. G. Georgeiv, and P. M. Pardalos, *Raman spectroscopy utilizing fisher-based feature selection combined with support vector machines for the characterization of breast cell lines,* Journal of Raman Spectroscopy **44**, 939 (2013).

[73] J. van de Vossenberg, H. Tervahauta, K. Maquelin, C. H. W. Blokker-Koopmans, M. Uytewaal-Aarts, D. van der Kooij, A. P. van Wezel, and B. van der Gaag, *Identification of bacteria in drinking water with Raman spectroscopy,* Analytical Methods **5**, 2679 (2013).

[74] Z. Movasaghi, S. Rehman, and I. U. Rehman, *Raman Spectroscopy of Biological Tissues,* Appl. Spectrosc. Rev **42**, 493 (2007).

[75] C. Xie, J. Mace, M. A. Dinno, Y. Q. Li, W. Tang, R. J. Newton, and P. J. Gemperline, *Identification of single bacterial cells in aqueous solution using confocal laser tweezers Raman spectroscopy,* Analytical Chemistry **77**, 4390 (2005).

[76] H. Sumikura, E. Kuramochi, H. Taniyama, and M. Notomi, *Cavity-enhanced Raman scattering of single-walled carbon nanotubes,* Applied Physics Letters **102**, 231110 (2013).

[77] K. C. Neuman and S. M. Block, *Optical trapping.* The Review of scientific instruments **75**, 2787 (2004).

[78] I. Bloch, *Ultracold quantum gases in optical lattices,* Nature Physics **1**, 23 (2005), arXiv:1312.5772 .

[79] S. Dochow, C. Krafft, U. Neugebauer, T. Bocklitz, T. Henkel, G. Mayer, J. Albert, and J. Popp, *Tumour cell identification by means of Raman spectroscopy in combination with optical traps and microfluidic environments,* Lab on a Chip **11**, 1484 (2011).

[80] O. G. Helleso, P. Lovhaugen, A. Z. Subramanian, J. S. Wilkinson, and B. S. Ahluwalia, *Surface transport and stable trapping of particles and cells by an optical waveguide loop,* Lab on a Chip **12**, 3436 (2012).

[81] A. Leinse, R. Heideman, W. Beeker, M. Hoekman, B. C.M., C. Roeloffzen, L. Zhuang, D. Marpuang, and M. Burla, *TriPlex photonic platform technology: Low-loss waveguide platform for applications from UV to IR,* 16th European Conference on Integrated Optics **4**, 6 (2012).

[82] R. Heideman, M. Hoekman, and E. Schreuder, *TriPleX-based integrated optical ring resonators for lab-on-a-chip and environmental detection,* IEEE Journal on Selected Topics in Quantum Electronics **18**, 1583 (2012).

[83] B. Jasse, R. S. Chao, and J. L. Koenig, *Laser Raman scattering in uniaxially oriented atactic polystyrene,* Journal of Polymer Science: Polymer Physics Edition **16**, 2157 (1978).

[84] K. J. Thomas, M. Sheeba, V. P. N. Nampoori, C. P. G. Vallabhan, and P. Radhakrishnan, *Raman spectra of polymethyl methacrylate optical fibres excited by a 532 nm diode pumped solid state laser,* Journal of Optics A: Pure and Applied Optics **10** (2008), 10.1088/1464-4258/10/5/055303.

[85] M. Boerkamp, T. V. Leest, J. Heldens, A. Leinse, M. Hoekman, R. Heideman, and J. Caro, *On-chip optical trapping and Raman spectroscopy using a TripleX dual-waveguide trap,* Optics express **22**, 30528 (2014).

[86] N. J. Everall, *Confocal Raman microscopy: performance, pitfalls, and best practice.* Applied spectroscopy **63**, 245A (2009).

[87] A. K. Trull, J. van der Horst, J. G. Bijster, and J. Kalkman, *Transmission optical coherence tomography based measurement of optical material properties,* Optics Express **23**, 33550 (2015).

[88] J. Kalkman, *Fourier-Domain Optical Coherence Tomography Signal Analysis and Numerical Modeling,* Hindawi International Journal of Optics **2017**, 16 (2017).

[89] L. Kong, P. Setlow, and Y.-q. Li, *Analysis of the Raman spectra of Ca(2+)-dipicolinic acid alone and in the bacterial spore core in both aqueous and dehydrated environments.* The Analyst **137**, 3683 (2012).

[90] L. R. van den Doel and L. J. van Vliet, *Temporal phase-unwrapping algorithm for dynamic interference pattern analysis in interference-contrast microscopy.* Applied optics **40**, 4487 (2001).

[91] J. Griffié, L. Boelen, G. Burn, A. P. Cope, and D. M. Owen, *Topographic prominence as a method for cluster identification in single-molecule localisation data,* Journal of Biophotonics **8**, 925 (2015).

[92] G. B. Loozen and J. Caro, *On-chip optical trapping of extracellular vesicles using box-shaped composite SiO2- Si3N4 waveguides,* Optics express **26**, 334 (2018).

[93] Y. Wang, Y. Ji, E. S. Wharfe, R. S. Meadows, P. March, R. Goodacre, J. Xu, and W. E. Huang, *Raman activated cell ejection for isolation of single cells,* Analytical Chemistry **85**, 10697 (2013).

[94] A. C. De Luca, S. Managó, M. A. Ferrara, I. Rendina, L. Sirleto, R. Puglisi, D. Balduzzi, A. Galli, P. Ferraro, and G. Coppola, *Non-invasive sex assessment in bovine semen by Raman spectroscopy,* Laser Physics Letters **11**, 055604 (2014).

[95] D. McIlvenna, W. E. Huang, P. Davison, A. Glidle, J. Cooper, and H. Yin, *Continuous cell sorting in a flow based on single cell resonance Raman spectra,* Lab Chip **16**, 1420 (2016).

[96] A. S. Bezryadina, D. C. Preece, J. C. Chen, and Z. Chen, *Optical disassembly of cellular clusters by tunable 'tug-of-war' tweezers,* Light: Science and Applications **5**, 1 (2016).

[97] G. Volpe, R. Quidant, G. Badenes, and D. Petrov, *Surface plasmon radiation forces,* Physical Review Letters **96**, 1 (2006).

[98] S. T. McCain, R. M. Willett, and D. J. Brady, *Multi-excitation Raman spectroscopy technique for fluorescence rejection.* Optics express **16**, 10975 (2008).

[99] C. G. Atkins, K. Buckley, M. W. Blades, and R. F. Turner, *Raman Spectroscopy of Blood and Blood Components,* Applied Spectroscopy **71**, 767 (2017).

[100] R. Osellame, H. J. Hoekstra, G. Cerullo, and M. Pollnau, *Femtosecond laser microstructuring: An enabling tool for optofluidic lab-on-chips,* Laser and Photonics Reviews **5**, 442 (2011).

[101] W. M. Pätzold, A. Demircan, and U. Morgner, *Low-loss curved waveguides in polymers written with a femtosecond laser,* Optics Express **25**, 263 (2017).

[102] P. . Debackere, D. . Taillaert, K. . De Vos, S. . Scheerlinck, P. . Bienstman, and B. Baets, *Si based Waveguide and Surface Plasmon Sensors*, Tech. Rep. (Universiteit Gent, 2007).

[103] R. Schmitt and A. Witte, *Development of a micro positioning stage for lab on a chip applications,* in *International Conference on Chemical, Biological and Environmental Engineering*, Cairo, 2010 (2010) pp. 119–123.

[104] D. Martens, G. Dong, and P. Bienstman, *Optimized Si3N4 grating couplers for relaxed alignment requirements under flood illumination,* Applied Optics **56**, 1286 (2017).

[105] V. Optika, *Fiber Coupled Microlens Array 2D Fiber Array Actively Aligned onto MLA,* (2018).

[106] A. Sánchez-Postigo, J. Gonzalo Wangüemert-Pérez, J. M. Luque-González, Í. Molina-Fernández, P. Cheben, C. A. Alonso-Ramos, R. Halir, J. H. Schmid, and A. Ortega-Moñux, *Broadband fiber-chip zero-order surface grating coupler with 0.4 dB efficiency,* Optics Letters **41**, 3013 (2016).

[107] Y. Lin, C. Browning, R. Timens, D. Geuzebroek, C. Roeloffzen, D. Geskus, R. Oldenbeuving, R. Heideman, Y. Fan, K. Boller, J. Zhao, and L. Barry, *Narrow linewidth hybrid InP-TriPleX photonic integrated tunable laser based on silicon nitride microring resonators,* Optics InfoBase Conference Papers **Part F84-O**, 38 (2018).

[108] D. M. Kita, H. Lin, A. Agarwal, K. Richardson, I. Luzinov, T. Gu, and J. Hu, *On-Chip Infrared Spectroscopic Sensing: Redefining the Benefits of Scaling,* IEEE Journal of Selected Topics in Quantum Electronics **23** (2017), 10.1109/JSTQE.2016.2609142.

[109] H. Brunner and H. Sussner, *Resonance Raman scattering on haemoglobin,* Biochimica et Biophysica Acta (BBA) - Protein Structure **310**, 20 (1973).

[110] P. Chen, Q. Tian, S. J. Baek, X. L. Shang, A. Park, Z. C. Liu, X. Q. Yao, J. Z. Wang, X. H. Wang, Y. Cheng, J. Peng, A. G. Shen, and J. M. Hu, *Laser Raman detection of platelet as a non-invasive approach for early and differential diagnosis of Alzheimer's disease,* Laser Physics Letters **8**, 547 (2011).

[111] A. C. De Luca, G. Rusciano, R. Ciancia, V. Martinelli, G. Pesce, B. Rotoli, L. Selvaggi, and A. Sasso, *Spectroscopical and mechanical characterization of normal and thalassemic red blood cells by Raman Tweezers,* Optics Express **16**, 7943 (2008).

[112] A. C. B. Filho, L. Silveira, A. L. S. Yanai, and A. B. Fernandes, *Raman spectroscopy for a rapid diagnosis of sickle cell disease in human blood samples: a preliminary study,* Lasers in Medical Science **30**, 247 (2014).

[113] D. Geuzebroek, A. V. Rees, E. Klein, and K. Lawniczuk, *Visible Arrayed Waveguide Grating (400nm – 700nm) for Ultra-wide Band (400-1700nm) Integrated Spectrometer for Spectral Tissue Sensing,* in *2017 IEEE 14th International Conference on Group IV Photonics (GFP)*, Vol. 223 (IEEE, Berlin, 2017) p. 2016.

[114] R. G. DeCorby, N. Ponnampalam, E. Epp, T. Allen, and J. N. McMullin, *Chip-scale spectrometry based on tapered hollow Bragg waveguides,* Optics express **17**, 16632 (2009).

[115] V. Maselli, J. R. Grenier, S. Ho, and P. R. Herman, *Femtosecond laser written optofluidic sensor: Bragg grating waveguide evanescent probing of microfluidic channel,* Optics Express **17**, 11719 (2009).

[116] S. J. Trietsch, T. Hankemeier, and H. J. van der Linden, *Lab-on-a-chip technologies for massive parallel data generation in the life sciences: A review,* Chemometrics and Intelligent Laboratory Systems **108**, 64 (2011).

[117] G. Luka, A. Ahmadi, H. Najjaran, E. Alocilja, M. Derosa, K. Wolthers, A. Malki, H. Aziz, A. Althani, and M. Hoorfar, *Microfluidics integrated biosensors: A leading technology towards lab-on-A-chip and sensing applications,* Sensors **15**, 30011 (2015).

"Final Message to His Creation:
##############"

From Douglas Adams'
"So long, and thanks for all the fish", page 165

ISBN: 978-94-6384-038-5